

Development of perovskite oxygen ion conducting materials for oxygen permeable membrane

(酸素透過膜用混合導電性ペロブスカイト型酸化物セラミックスの研究)

2011 年

高橋 洋祐

名古屋工業大学博士論文
甲第791号(課程修了による)
平成23年3月23日授与

Contents

1. Introduction of research
 - 1.1. Oxygen permeable membrane
 - 1.2. Solid oxide fuel cell (SOFC)
 - 1.3. Purposes of the study
2. Summary of experimental measurement
 - 2.1. Measurement of electron and ion conductivities
 - 2.2. Measurement of oxygen permeation
3. The fundamental characteristics of $\text{LaSrTiFeO}_{3-\delta}$ oxygen ion conducting materials
 - 3.1. Introduction
 - 3.2. Experimental
 - 3.3. Results and Discussion
 - 3.4. Conclusion
4. In situ analysis of $\text{La}_{0.6}\text{Sr}_{0.4}\text{Ti}_{0.1}\text{Fe}_{0.9}\text{O}_{3-\delta}$ and $\text{La}_{0.6}\text{Sr}_{0.4}\text{Ti}_{0.3}\text{Fe}_{0.7}\text{O}_{3-\delta}$ oxygen ion conductors
 - 4.1. Introduction
 - 4.2. Experimental
 - 4.3. Results and Discussion
 - 4.4. Conclusion
5. Multilayer ceramic deposition process of dense oxygen permeable membranes on porous supports
 - 5.1. Introduction
 - 5.2. Experimental
 - 5.3. Results and Discussion
 - 5.4. Conclusion
6. Oxygen ion conducting membranes sintered under different atmosphere and HIP

- 6.1. Introduction
- 6.2. Experimental
- 6.3. Results and Discussion
- 6.4. Conclusion
7. Rheological study of $\text{LaSrTiFeO}_{3-\delta}$ paste for screen printing process
 - 7.1. Introduction
 - 7.2. Experimental
 - 7.3. Results and Discussion
 - 7.4. Conclusion
8. Summary
9. References
10. List of Publications
11. Acknowledgment

1. Introduction

Perovskite-oxide ion-conductive materials are studied, with the purpose of using them as oxygen-permeable membranes for the partial oxidation of methane as well as for other oxygen production and enrichment activities or as materials (mainly, cathode materials) for solid oxide fuel cells (SOFCs).

1.1. Oxygen permeable membrane

Gas-to-liquid (GTL) fuels, which are produced from natural methane gas (CH_4) processed into synthesis gas, syngas (CO and H_2), has drawn attention in recent years as a clean energy solution.

As shown in the schematic of the GTL process in Figure 1-1, GTL fuel can be transported by sea because it is in liquid form. In addition, transport ships can be used as a platform for the synthesis of GTL fuel.

GTL fuel is produced through the processes of syngas production and fuel synthesis (Fischer-Tropsch synthesis, $\text{CO} + 2\text{H}_2 \rightarrow 1/n(\text{CH}_2)_n + \text{H}_2\text{O}$). The cost of these production and synthesis processes accounts for at least 60% of the total cost; therefore, a reduction in the cost of the syngas production process is required. In the production of syngas from CH_4 , the following reactions are mainly involved.

Partial oxidation reaction $\text{CH}_4 + 1/2\text{O}_2 \rightarrow 2\text{H}_2 + \text{CO} + 35.6\text{kJ/mol}$

Steam reforming reaction $\text{CH}_4 + \text{H}_2\text{O} \rightarrow 3\text{H}_2 + \text{CO} - 206\text{kJ/mol}$

The partial oxidation process is advantageous over the steam reforming process because of its exothermic reaction and ideal gas composition ratio of syngas, $\text{H}_2/\text{CO}=2$, which is the same as that of the feeding gas in the GTL process. ¹⁾

This new method takes advantage of the high methane content in the gas generated in coke ovens of steel mills and produces hydrogen through the partial oxidation of methane and oxygen. ²⁾

In both cases, there is a strong demand for compact, low-cost, energy-efficient technology of oxygen production for the partial oxidation process. Cryogenic distillation, the conventional oxygen-generating method, requires massive facilities associated with high plant construction costs—costs which in some cases account for 50% of the total construction cost of a syngas plant. Ceramic oxygen-permeable membrane reactors based on oxygen-ion conductors are widely regarded as a promising solution. ³⁻⁶⁾

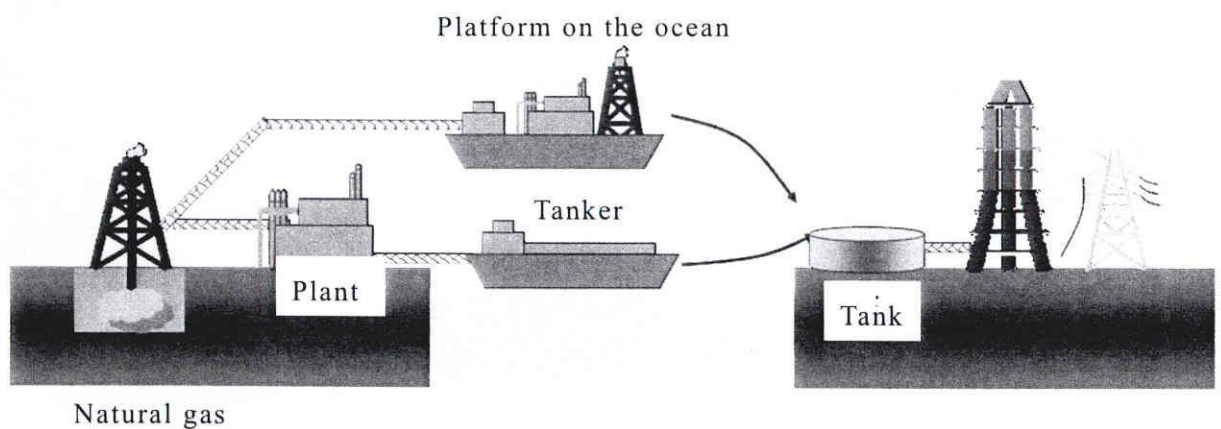
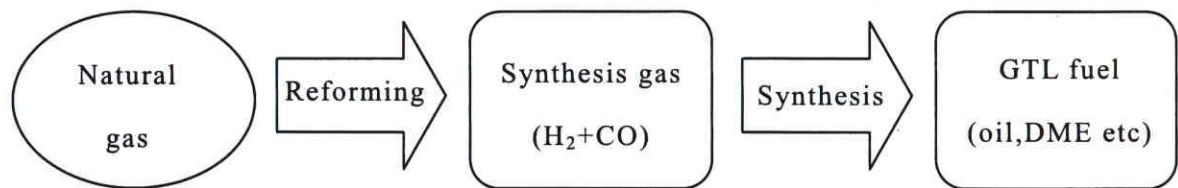


Fig.1-1. Schematic of GTL process.

Figure 1-2 shows a schematic diagram of the partial oxidation reaction of CH_4 using a membrane reactor. CH_4 is supplied to one side of the membrane and air to the other. The difference in electrochemical potential on the two sides of the membrane causes oxygen to permeate through the membrane in the form of oxide ions. At anode

surface, the catalyst activates the partial oxidation reaction of CH_4 with permeated oxygen, producing syngas, CO and H_2 . This oxygen-permeable membrane reactor allows the simultaneous generation of oxygen and synthesis gas very compactly in a single facility.

Owing to the compact process of fuel production, plant cost can be reduced, leading to the reduction in fuel production cost. Moreover, the compact process also enables the effective use of smaller gas fields in Asia, Oceania, and the Americas, which have not been used because of their perceived unprofitability.

The importance of oxygen production and enrichment technologies in industry is increasing owing to the recent increase in environmental consciousness. For example, these technologies are frequently used for combustion and chemical reaction systems in power plants and ironworks that emit a large amount of CO_2 . The combustion efficiency is improved by effectively using O_2 in such systems, with the aim of reducing CO_2 emission. Recently, the conversion efficiency of fuel cells has been improved. Thus, oxygen production and enrichment technologies are expected to be used as clean-energy-related technologies.

For the facilities/sites that require a relatively small volume of O_2 , O_2 gas tanks delivered from an oxygen-generating facility are usually used. The ceramic membrane reactors as shown in Figure 1-3 allow the use of exhaust heat generated by the O_2 separating reaction as an auxiliary power source, for use in small facilities. This advantage allows the deployment of oxygen-permeable membranes not only to replace conventional oxygen-generating facilities but also to supply the by-product heat.

As shown in the schematic in Figure 1-4, tube type oxygen-permeable membranes are generally bundled together for use and the number of these membranes is increased depending on the required volume of O_2 . The use of planar and honeycomb cell structures is also examined. Cryogenic distillation requires a reasonably large plant to collect oxygen by cooling air to approximately -200°C , whereas, for example,

a small oxygen-separating membrane system can produce a considerable volume of oxygen with a system size of only 1 m³.

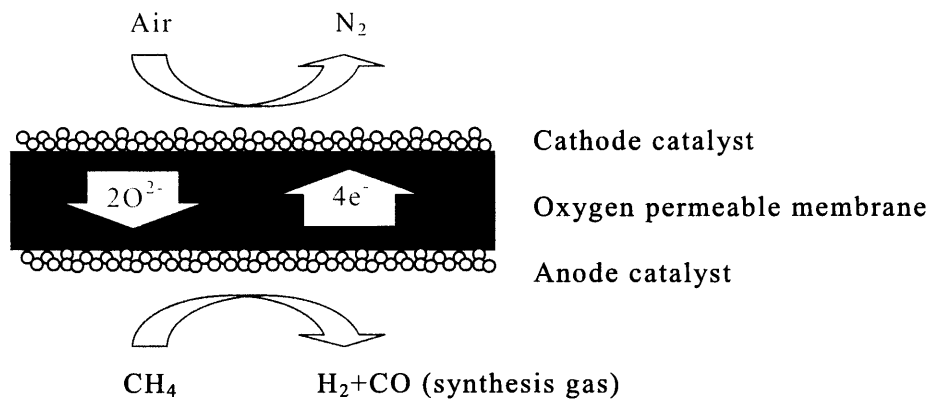


Fig.1-2. Schematic of CH₄ conversion using oxygen permeable membrane.

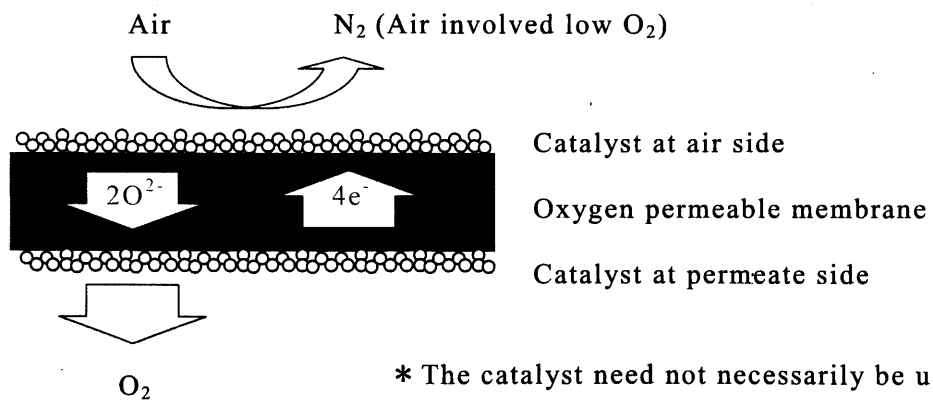


Fig.1-3. Schematic of O₂ generation using oxygen permeable membrane.

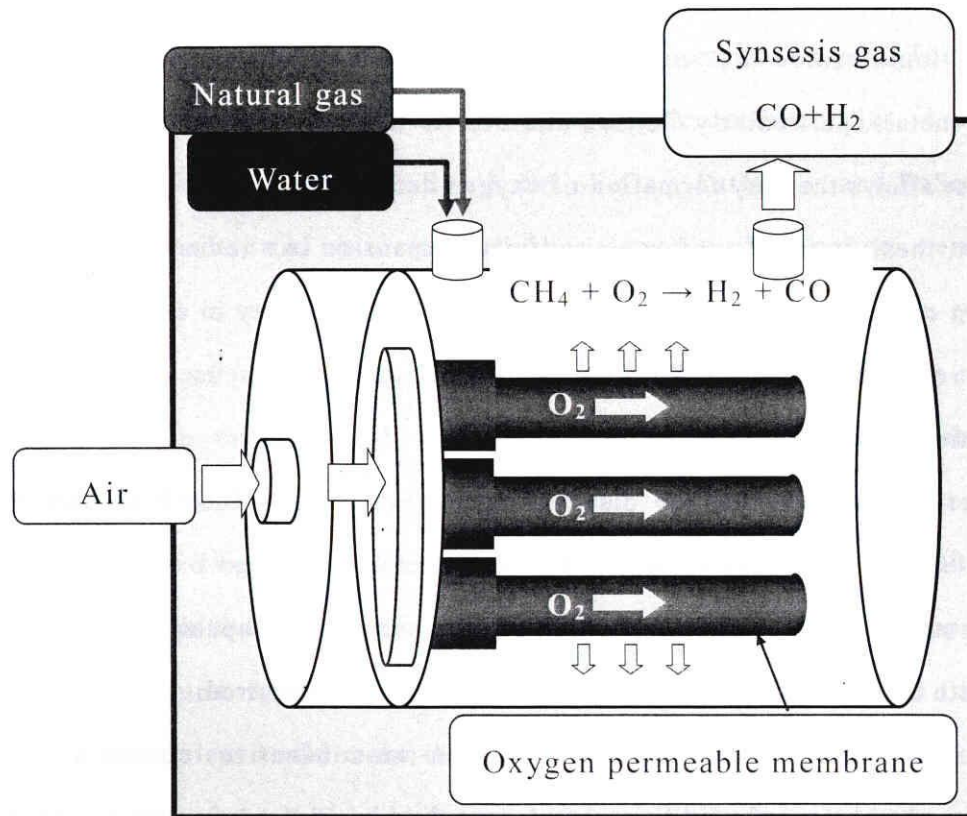


Fig.1-4. Schematic of CH₄ conversion system using oxygen permeable membrane reactor.

Much work is currently being devoted to investigations on mixed conductive oxides, which exhibit both oxygen-ion and electron conductivities, as candidate materials for oxygen-permeable membranes. They allow oxygen to pass continuously from one side to the other side of the membrane because of the difference in oxygen partial pressure, without external electrodes or circuitry. To date, the perovskite-type oxide LaMO_{3-δ} (M=Co, Cu, Ga, Fe, Ni, etc.),⁷⁻¹³⁾ the non perovskite-type oxide SrCo_{0.5}FeO_x,¹⁴⁾ and the mixed-oxide Ce_{0.8}Gd_{0.2}O_x-MnFe₂O₄¹⁵⁾ systems are reported to have high oxygen permeation capabilities. The perovskite oxide system is a good candidate for the oxygen-permeable membrane, with an easy-to-control

transport property by substituting the La site (A site, larger cation in 12-fold coordination) or M site (B site 6-fold coordination). The La ion is chosen for its appropriate ionic radii that enable easy construction of the cubic ABO_3 lattice. Transition metals, particularly Co, Mn and Fe, are favorable for their mixed charge valence that allows the easy formation of oxygen defects.

However, these materials undergo significant expansion in a reducing atmosphere, resulting in cracks and hence create problems of poor durability in cyclic operation. Pei et al. reported that these failures result from large volumetric changes in the crystal lattice.¹⁶⁾

Moreover, such materials are disadvantageous in terms of cost because they contain relatively expensive metal elements. Therefore, low-cost oxygen-permeable membrane materials with sufficiently high oxygen permeation capability for practical use and with high durability in a reducing atmosphere are required.

The ceramic membranes based on oxygen-ion-conductive ceramics induce dissociative absorption of oxygen molecules on the air side and transport oxide ions effectively using oxygen defects in the oxide, resulting in the recombination of oxide ions into oxygen molecules on the permeation side, thus promoting oxygen permeation. The oxygen ion conduction becomes the rate-determining step for oxygen permeation when membranes are thick. The surface reaction becomes the rate-determining step when membranes are thin. For the rate-determining step of oxygen ion conduction, the rate of oxygen permeation j_{O_2} can be expressed by

$$j_{O_2} = (RT/16F^2L) \times \sigma_i \times \ln(PO_2^h/PO_2^l) \quad (1)$$

where R , T , F , L , σ_i , PO_2^h , and PO_2^l are the gas constant, absolute temperature, Faraday constant, membrane thickness, oxygen ion conductivity, oxygen partial pressure on the air side, and oxygen partial pressure on the permeation side, respectively. According to equation (1), if the conditions of the oxygen permeation

reaction (temperature, pressure) are fixed, the rate of oxygen permeation increases when using materials with higher oxygen ion conductivity or thinner membranes.

Two approaches have been used to enhance the O₂ permeation rate. The first is to develop new materials with high electronic and ionic conductivities. As it is well known, certain perovskite-type oxides, LaSrCoFeO_{3-δ}, LaGaO_{3-δ}, and BaSrCoFeO_{3-δ}, exhibit high electronic and ionic conductivities, as well as high oxygen permeability.¹⁷⁻¹⁹⁾ The second is to fabricate a very thin dense layer of oxygen-ion-conductive material on top of a porous support.²⁰⁻²²⁾ One factor impeding thin-membrane formation is the mismatch of the thermal expansion coefficient between the membrane and the porous support. Typical oxygen-ion-conductive ceramic membranes have large thermal expansion coefficients of 10 to 15 (x10⁻⁶/K⁻¹) or greater, while the thermal expansion coefficient of porous ceramic supports (e.g., alumina) is around 5 to 7 (x10⁻⁶/K⁻¹).²³⁻²⁵⁾ Such large difference in thermal expansion coefficient could make the use of the ceramic membranes difficult under the thermal cycle from R.T. to high temperatures. While one could use zirconia or magnesia, which have relatively high thermal expansion coefficients as supports, such materials could easily react with the membrane or degrade the membrane by the thermal shock resulting from the difference in thermal expansion coefficients. Researchers are currently exploring the fabrication of porous supports composed of the same material as the membranes, but this approach can give rise to other problems, including porosity deterioration and warping, as the supports could also undergo shrinkage when the membranes are heated to the densification temperature.^{20,21)}

There has been a report on a process by which a certain number of pores (a certain gas permeability) can be maintained in the membrane even after sintering using a porous support composed of materials with a relatively large particle diameter.^{20,21)} However, other problems could arise in this method, for example, the surface roughness of the porous support made of large particles might not be good enough to

fabricate thin membranes over them. Therefore, an efficient method and related material technologies for forming a dense perovskite-oxide thin film with a relatively high thermal expansion coefficient on a porous support are desired.

Another problem is that many perovskite oxides have relatively high sintering temperatures of 1200-1600°C, making densification difficult. If the sintering temperature is simply increased to promote densification, the perovskite oxide could degrade. Recently, thinner membranes have been developed with improved performance (10 μm or thinner membranes have been made); however, gas leakage due to pores in membranes with insufficient density has also become a problem. As a measure to improve the gas tightness of membranes, membrane processing parameters had been optimized; for example, in the case of screen printing, pastes that can fill the pores to a high density have been employed. The optimization of the sintering conditions has also been studied.

1.2. SOFCs

SOFCs are being actively developed as a next-generation power source because of their high power generation efficiency.²⁶⁻³⁰ Figure 1-5 show the most common anode-support cell structure. Oxygen molecules on the cathode perovskite oxide are dissociated and receive electrons from an external circuit to form oxygen ions (O^{2-}), which are supplied to a solid electrolyte (stabilized zirconia). On an anode fuel electrode (a cermet of stabilized zirconia and nickel oxide), O^{2-} from the solid electrolyte reacts with hydrogen, producing vapor and releasing electrons into the external circuit. The structure of SOFCs is similar to that of oxygen-permeable membranes explained in section 1.1; however, electrons do not conduct in a solid electrolyte unlike those in oxygen-permeable membranes. The perovskite-oxide ion-conductive materials considered in this study are generally used as cathode materials because of their electronic conductivity. Perovskite oxides containing Co, Mn, or Fe at the B site are frequently used.

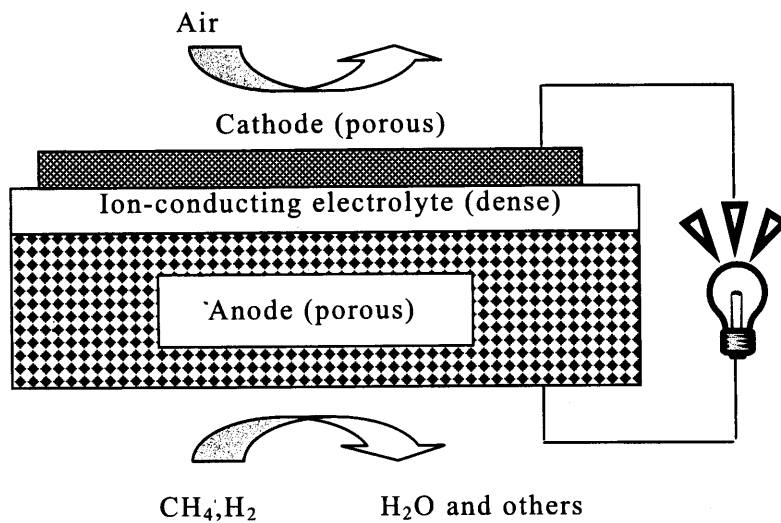


Fig.1-5. Schematic of anode-support cell structure.

For SOFC cathode materials, the required material properties (e.g., oxygen ionic conductivity, electronic conductivity, durability, and reactivity) differ depending on the cell composition, material and structure (widely ranging from cylindrical, planar, to seal-free types) and the scale of application (power generation capability). Currently, low cost and improved durability are common aims of technological development. Accordingly, high-ionic-conductivity cathode materials that are highly reactive to each cell component and contain no expensive Co or Mn are required. In addition, because printing process is frequently used for fabricating SOFC cathode materials as well as oxygen-permeable membranes, device technologies for realizing ceramic pastes that enable particles to fill the pores at a high density are also necessary.

1.3 Purposes of the study

The first purpose of this study was to clarify the fundamental characteristics of $\text{LaSrTiFeO}_{3-\delta}$, a novel perovskite-oxide ion-conductive material with high durability in reducing atmosphere, high oxygen ionic conductivity, and reasonably low cost. In this material, the substitution of Ti at the B site is expected to improve the durability in reducing atmosphere and lower the cost of the material. Compared with the already identified elements at the B site such as Co, Ti is less likely to undergo valence changes, which should result in a more stable crystal structure and less cracking due to thermal expansion in the reducing atmosphere. We have investigated the ionic and electronic conductivities of each component at the A and B sites of $\text{LaSrTiFeO}_{3-\delta}$ and also examined its oxygen permeation performance and the thermal expansion coefficient. The results were systematically evaluated to determine the optimal composition.

The second purpose of the study was to clarify the mechanism of thermal expansion for $\text{LaSrTiFeO}_{3-\delta}$ -based materials in a reducing atmosphere. We carried out *in situ* thermal expansion analysis, *in situ* X-ray diffraction (XRD) structural analysis, in oxidation and reducing atmospheres with the aim of obtaining the factors determining thermal expansion in a reducing atmosphere and measures against the resulting cracking.

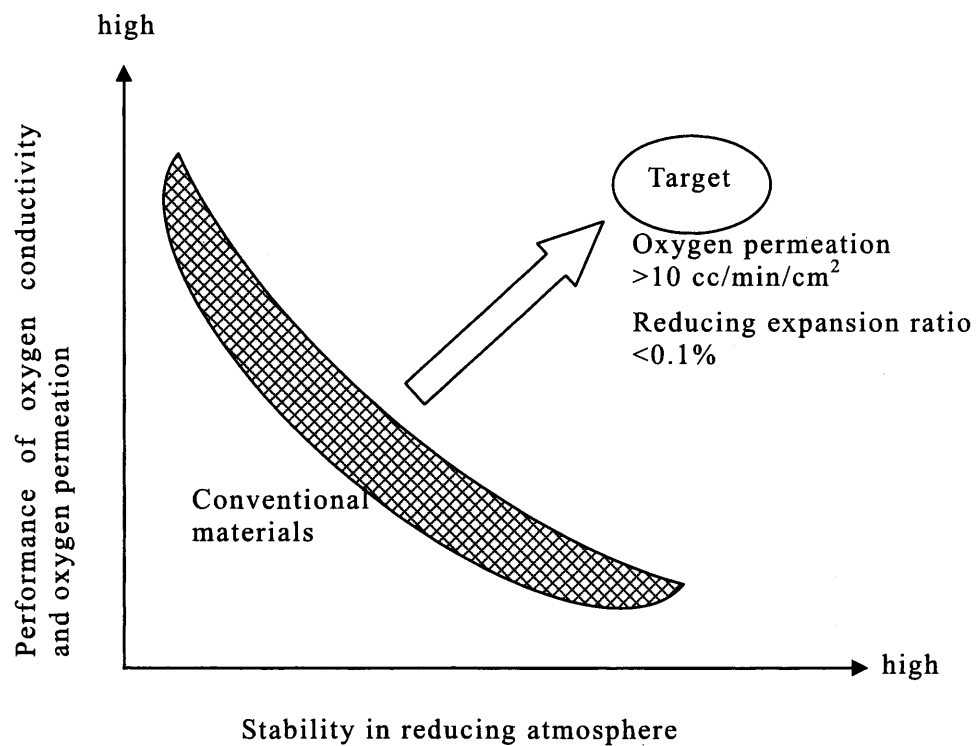
The third purpose was to optimize the ceramic production process. We examined the adoption of a multilayer process, and evaluated the effects of sintering conditions and the rheological characteristics of ceramic pastes used for screen printing. Thus, we obtained new results on the fundamental characteristics required to apply oxygen ion-conductive materials in practical elements and modules.

The fundamental characteristics of $\text{LaSrTiFeO}_{3-\delta}$ oxygen ion conducting materials

The mechanism of thermal expansion for $\text{LaSrTiFeO}_{3-\delta}$ in a reducing atmosphere

The ceramic production process of oxygen ion conducting materials

- Rheological behavior of ceramic paste
- Sintering condition



2. Summary of Experimental measurement

2.1. Measurement of electron and ion conductivities

The sintered bar was cut into $3 \times 3 \times 15$ mm for the measurement of electrical conductivity. Pt wires were attached to the sample with Pt paste and then fired at 1000°C to form four point probes. We evaluated electron and ion conductivities separately by measuring the four-point DC electrical conductivity of the bar sample with four-point electrode contacts with various oxygen partial pressures of the atmosphere. The reducing gas mixture of carbon dioxide, methane, and hydrogen was fed into the test chamber to reduce the oxygen partial pressure of the atmosphere, as monitored by an oxygen sensor. In this four-point terminal DC method, we eliminated the effects of sample polarization and system errors by alternating the polarity of the electric current flow, taking three sets of measurements, for a total of six measurement sets, and calculating the average values.

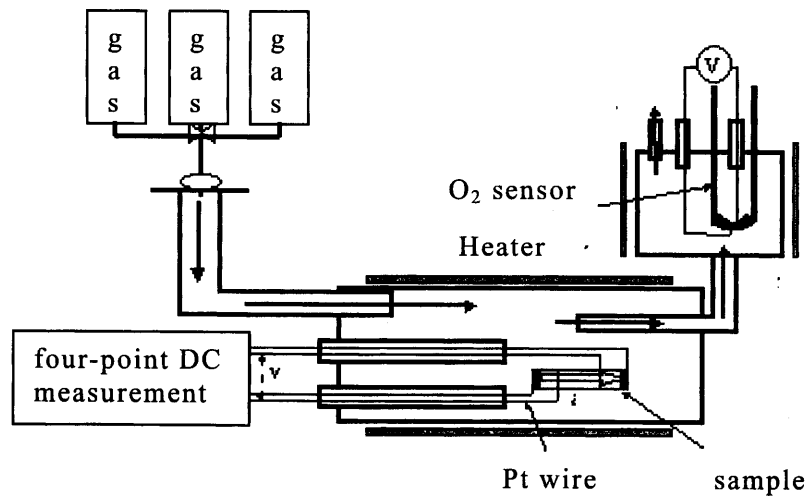


Fig.2-1. The schematic of measurement of conductivity.

2.2. Measurement of oxygen permeation

Disk and tube samples with catalytic electrodes were used for the oxygen permeation performance test, as shown in Figure 2-2, at temperatures from 800 to 1000°C. The sample placement section was constructed on two high-density alumina tubes and the sample was bonded with the outer tube with glass seal. Air and CH₄ fuel gas were fed the air and fuel electrode sides, 100-500cc/min, respectively. CH₄ reacts with oxygen, which comes through the oxygen-permeable membrane sample, on the fuel catalyst electrode and generates syngas ($\text{CH}_4 + 1/2\text{O}_2 \rightarrow 2\text{H}_2 + \text{CO}$). The rate of oxygen permeation was calculated from the flow rates and concentrations of oxygen or syngas analyzed in the gas flow downstream of the fuel side. The gas concentration was analyzed with a gas chromatograph (GL Science CP-4900). Nitrogen leakage through the sample was also monitored by this method to evaluate the concentration of nitrogen in the gas flow downstream of the fuel side.

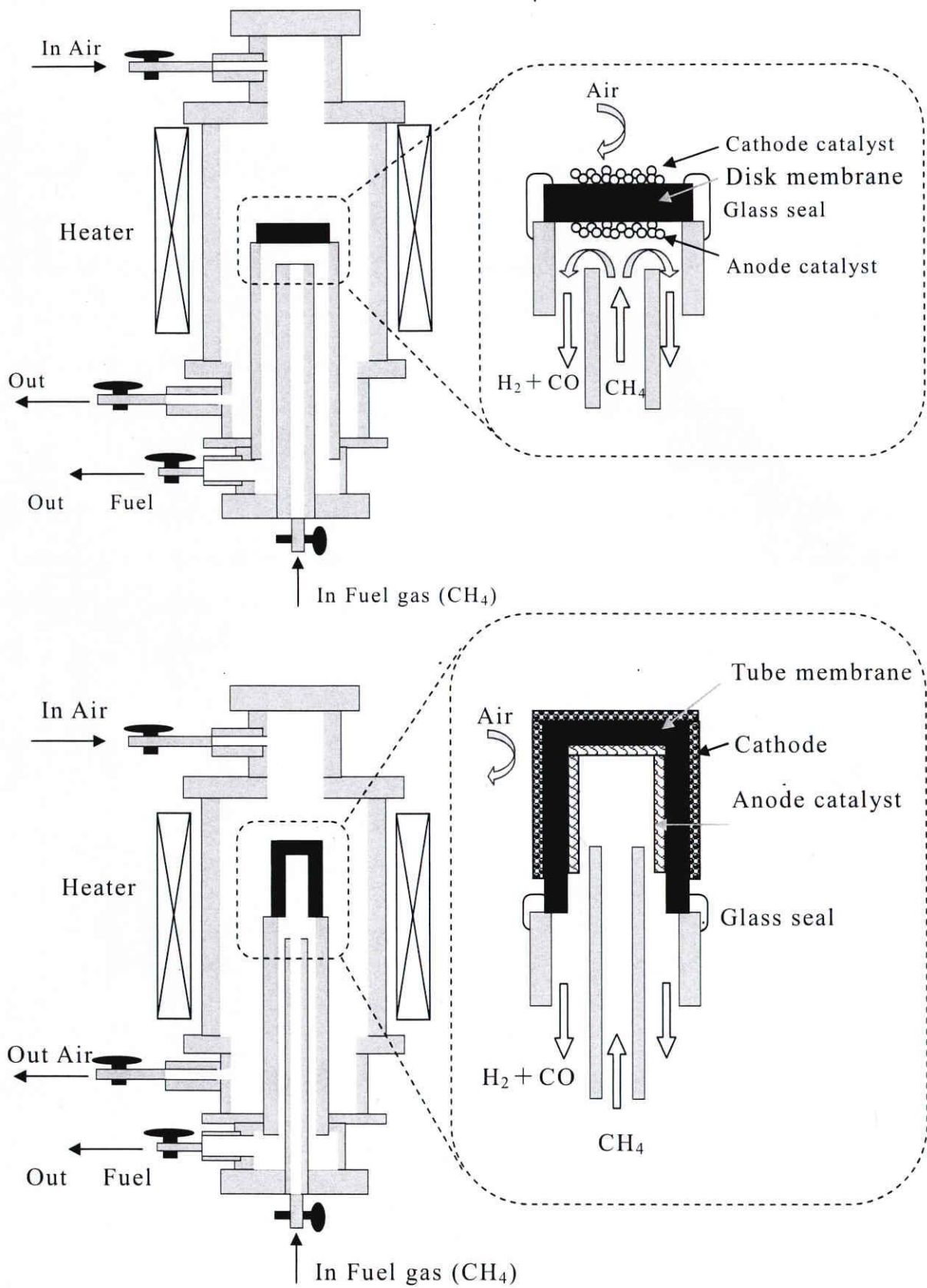


Fig.2-2.Experimental set up for oxygen permeation test for the disk and tube membranes.

3. The fundamental characteristics of $\text{LaSrTiFeO}_{3-\delta}$ oxygen ion conducting materials

3.1. Introduction

To solve the problem as chapter 1, a novel perovskite-type oxide system, $\text{La}_{1-x}\text{Sr}_x\text{Ti}_{1-y}\text{Fe}_y\text{O}_{3-\delta}$, has been developed for the oxygen-permeable membrane in this study. The substitution of the La site by Sr is expected to cause the formation of oxygen vacancies and to stabilize the lattice, leading to a reduced thermal expansion. Compared with Co at the B site, Ti is less likely to undergo valence changes and should result in a more stable crystal structure and less cracking in a reducing atmosphere. The substitution of Ti by Fe is expected to improve durability and to lower the cost of materials.

We have investigated the electrical transport properties of bar-shaped sintered bodies and the oxygen permeation of disk-type sintered bodies of $\text{La}_{1-x}\text{Sr}_x\text{Ti}_{1-y}\text{Fe}_y\text{O}_{3-\delta}$ membranes and examined also the thermal expansion of these oxide membranes in air atmosphere to determine the index of durability in cyclic operation and the matching to the porous support, for example, stabilized zirconia, currently in use. Understanding the trade-off between the high electrical or oxygen-transport properties and the low thermal expansion is the issue in this study, aiming at obtaining a robust high-performance membrane.

3.2. Experimental

3.2.1. Preparation of $\text{La}_{1-x}\text{Sr}_x\text{Ti}_{1-y}\text{Fe}_y\text{O}_{3-\delta}$ (LSTF) membrane

Powders of La_2O_3 (Wako Pure Chemical Industries, Ltd., grain size 1 μm), SrCO_3 (Wako, grain size 1 μm), TiO_2 (Wako, grain size 1 μm), and Fe_2O_3 (Wako, grain size 1 μm) were mixed to prepare various compositions of $\text{La}_{1-x}\text{Sr}_x\text{Ti}_{1-y}\text{Fe}_y\text{O}_{3-\delta}$ with $x = 0.1-0.8$ and $y = 0.6-1.0$. The powders were mixed using a ball mill with YSZ balls for 5 h, and then calcined at 1000°C for 6h. The calcined powder was mixed with a PVA

aqueous solution binder and compacted into pellets (bar of 5×5×30mm, disk of $\phi=25\text{mm}\times t=3\text{mm}$) using a compact press of 100 MPa. These compacts were fired at 1400°C in air for 3h.

The sintered bar was cut into 3×3×15 mm for the measurement of electrical conductivity. Pt wires were attached to the sample with Pt paste and then fired at 1000°C to form four point probes. The sintered disks were then polished to a thickness of 0.5 mm to prepare the LSTF membrane samples for the oxygen permeation performance test. For this test, the electrode and catalyst were formed on the surface of the disk of membrane samples, as shown in Figure 2-2. A slurry of powder mixture, NiO and $\text{Ce}_{0.8}\text{Sm}_{0.2}\text{O}_2$ electrode catalyst mixed in a 1:1 weight ratio, was screen-printed on the fuel side of the sample and dried. This NiO- $\text{Ce}_{0.8}\text{Sm}_{0.2}\text{O}_2$ was selected for catalytic electrode material because of its high performance of ionic conductance of $\text{Ce}_{0.8}\text{Sm}_{0.2}\text{O}_2$ and high catalytic activity of NiO³¹⁾. An air electrode of $\text{La}_{0.5}\text{Sr}_{0.5}\text{CoO}_3$, one of the most promising cathode materials³²⁾, was screen-printed on the other surface of the disk and dried. To sinter these oxide electrodes, the sample disks were fired again at 1000°C for 1h.

3.2.2. Characterization

We evaluated electron and ion conductivities separately by measuring the four-point DC electrical conductivity of the bar sample with four-point electrode contacts with various oxygen partial pressures of the atmosphere. (Experimental detail: Chapter 2)

Oxygen permeation test of disk samples was carried out as Chapter 2 at temperatures from 800 to 1000°C.

As an index of the durability in cyclic operation, thermal expansion of the LSTF sample was measured using Rigaku TMA8310 at temperatures from 25°C to 1000°C in air.

3.3. Results and Discussion

3.3.1. P_{O_2} dependent electrical conductivity and thermal expansion

The electrical conductivity of the LSTF membrane sample was strongly dependent on the oxygen partial pressure, P_{O_2} . Changing P_{O_2} of the atmosphere of the sample, the plot of conductivity shows a minimum region, where the electronic conduction becomes smaller than the ionic conduction. From this plot, the contributions of electronic and ionic conduction can be evaluated separately.

Figure 3-1 a typical XRD pattern of representative LSTF membrane, $La_{0.6}Sr_{0.4}Ti_{0.2}Fe_{0.8}O_{3-\delta}$, after sintering at 1400 °C. The $La_{0.6}Sr_{0.4}Ti_{0.2}Fe_{0.8}O_{3-\delta}$ oxide after the sintering was single phase of perovskite. All the samples in this study were also confirmed as perovskite single phase and the lattice parameter was decreased by Fe substitution. Further analysis on the crystal structures of this perovskite system is discussed at chapter 4.

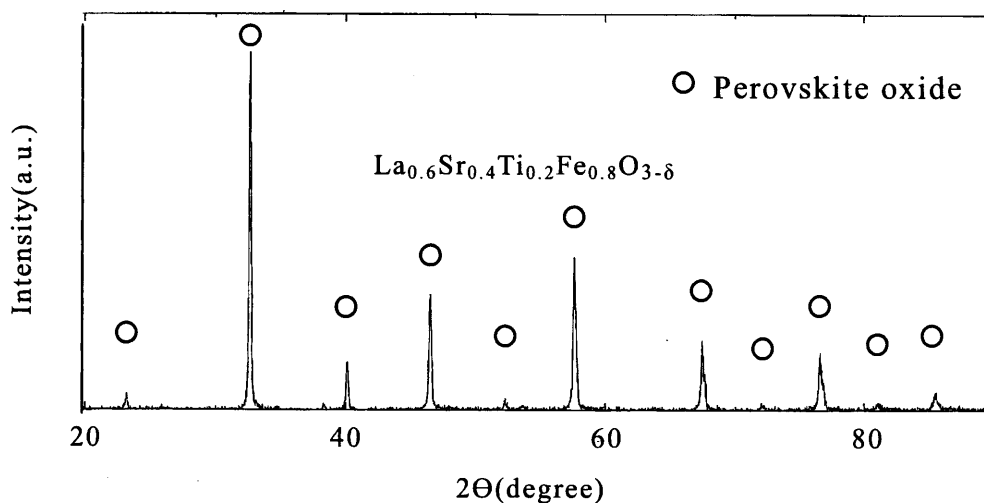


Fig.3-1. XRD pattern of $La_{0.6}Sr_{0.4}Ti_{0.2}Fe_{0.8}O_{3-\delta}$ membrane after sintering at 1400 °C.

Figure 3-2 shows the dependence of conductivity on P_{O_2} for two representative composition sets of LSTF. The effects of A-site substitution, changing x in $La_{1-x}Sr_xTi_{0.1}Fe_{0.9}O_{3-\delta}$, and B-site substitution, changing y in $La_{0.6}Sr_{0.4}Ti_{1-y}Fe_yO_{3-\delta}$, are shown in Figure 3-2 (a) and (b), respectively. For both cases, the flat plateaus of low conductivity, or the region of ion conductivity, were observed and the results are consistent with those reported by Ma³³⁾ and Ishihara¹³⁾. Sr substitution increased the ionic conductivity in the set of $La_{1-x}Sr_xTi_{0.1}Fe_{0.9}O_{3-\delta}$, as shown in Figure 3-2 (a). This change is similar to the results of these membranes in previous reports. On the other hand, La substitution has been reported to enhance the stability with respect to reduction in reducing or H_2 -containing atmospheres.³⁴⁾ Considering this stability matter, the A-site substitution of Sr has been carried out up to 50% La in this study. In this region, the increase in ionic conductivity seems to be saturated at around Sr 40% or 50%.

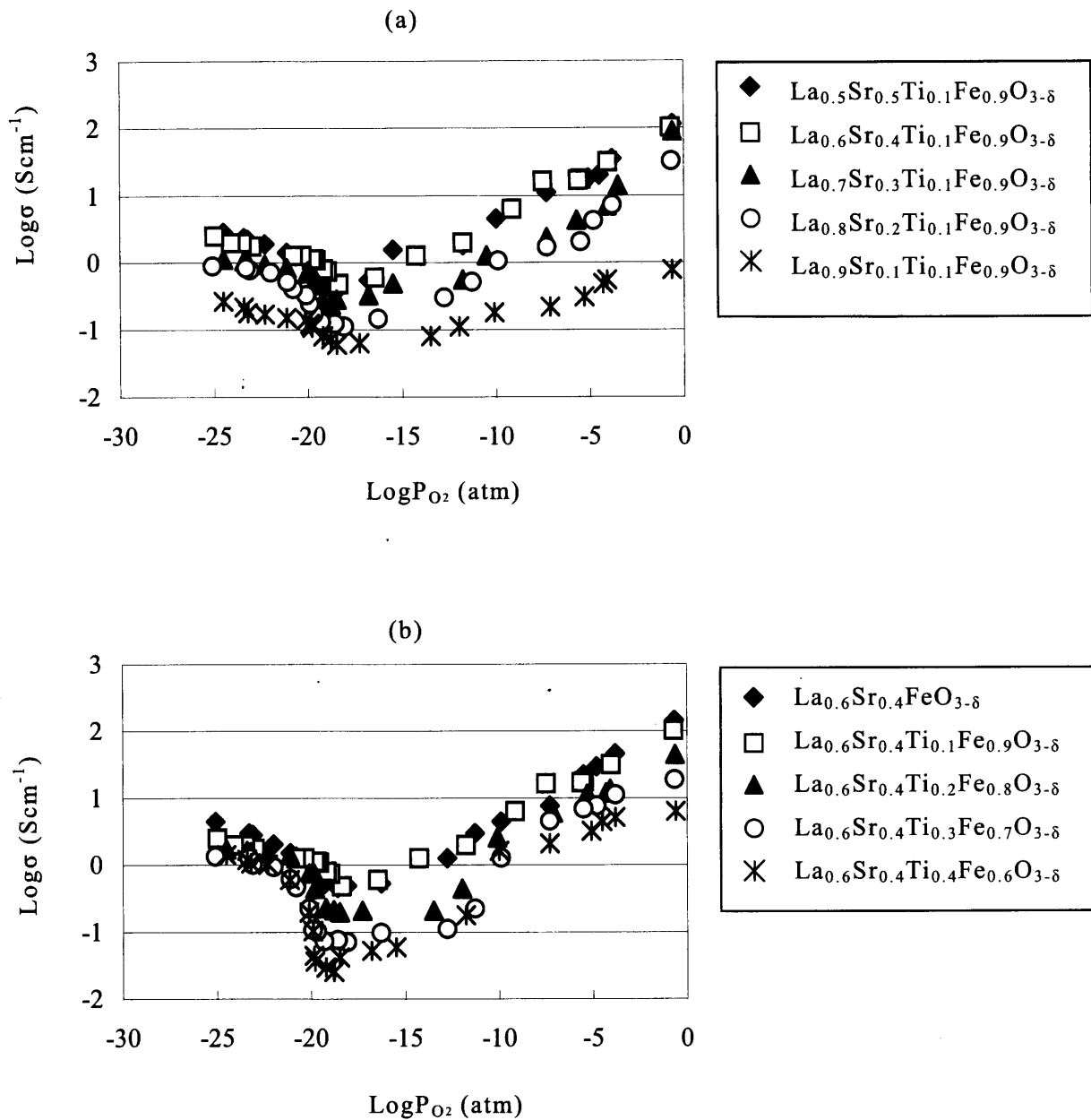


Fig.3-2. Oxygen partial pressure dependence of conductivity of LSTF membranes at 800°C,

(a) A-site substituted $\text{La}_{1-x}\text{Sr}_x\text{Ti}_{0.1}\text{Fe}_{0.9}\text{O}_{3-\delta}$ and

(b) B-site substituted $\text{La}_{0.6}\text{Sr}_{0.4}\text{Ti}_{1-y}\text{Fe}_y\text{O}_{3-\delta}$, samples.

Fe substitution increased the p-type electrical and oxygen ionic conductivity in the set of $\text{La}_{0.6}\text{Sr}_{0.4}\text{Ti}_{1-y}\text{Fe}_y\text{O}_{3-\delta}$, as shown in Figure 3-2 (b), and also reported previously.^{35, 36)} Fagg et al.³⁴⁾ reported that the activation energy was unchanged by Fe substitution, and concluded that the small-polaronic conduction mechanism is unchanged. Also, Fe substitution increases ionic conductivities to vacancy ordering, as reported for $\text{Sr}_{0.97}(\text{Ti,Fe})\text{O}_{3-\delta}$.³⁶⁾

The sample of composition $\text{La}_{0.6}\text{Sr}_{0.4}\text{Ti}_{0.1}\text{Fe}_{0.9}\text{O}_{3-\delta}$ was investigated further at higher temperature. Figure 3-3 shows the oxygen partial pressure dependence of the conductivity of the $\text{La}_{0.6}\text{Sr}_{0.4}\text{Ti}_{0.1}\text{Fe}_{0.9}\text{O}_{3-\delta}$ membrane sample at 800, 900 and 1000°C. As the temperature increases, oxygen ionic conductivities are increased. The E_a of p-type electronic conduction can be deduced to be 38 kJ/mol from the three data values in air atmosphere. This value is similar to that reported by Fagg et al.³⁴⁾ This means the mechanism of p-type electronic conduction is the same.

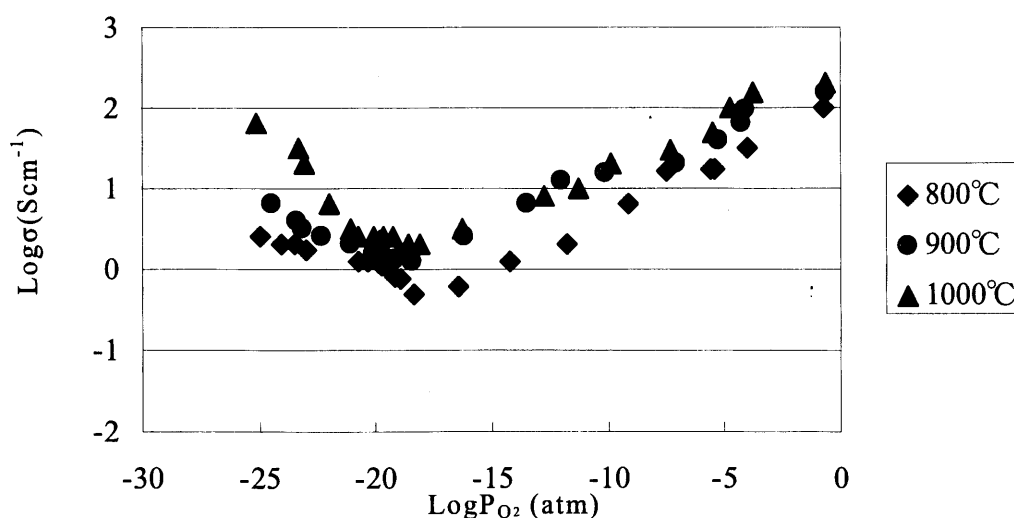


Fig.3-3. Oxygen partial pressure dependence of conductivity of $\text{La}_{0.6}\text{Sr}_{0.4}\text{Ti}_{0.1}\text{Fe}_{0.9}\text{O}_{3-\delta}$ membrane sample at 800,900 and 1000°C.

Figure 3-4 shows the temperature dependence of the ionic conductivity of $\text{La}_{0.6}\text{Sr}_{0.4}\text{Ti}_{1-y}\text{Fe}_y\text{O}_{3-\delta}$ ($y=0.7-0.9$). The values of the activation energy calculated from the data in Figure 6 are 11 -20 kJ/mol. These values are much lower than those previously reported for $\text{LaSrTiFeO}_{3-\delta}$ compositions. Fagg et al. reported that the values of the activation energy for ionic conduction are similar in A-site-deficient $\text{LaSrTiFeO}_{3-\delta}$ and that lattice distortions due to Sr substitution decrease the mobility of oxygen ions.³⁴⁾ In our study, the values of the activation energy are almost unchanged after Fe substitution. Because the composition of Sr is different between previous studies and our study, further study is necessary.

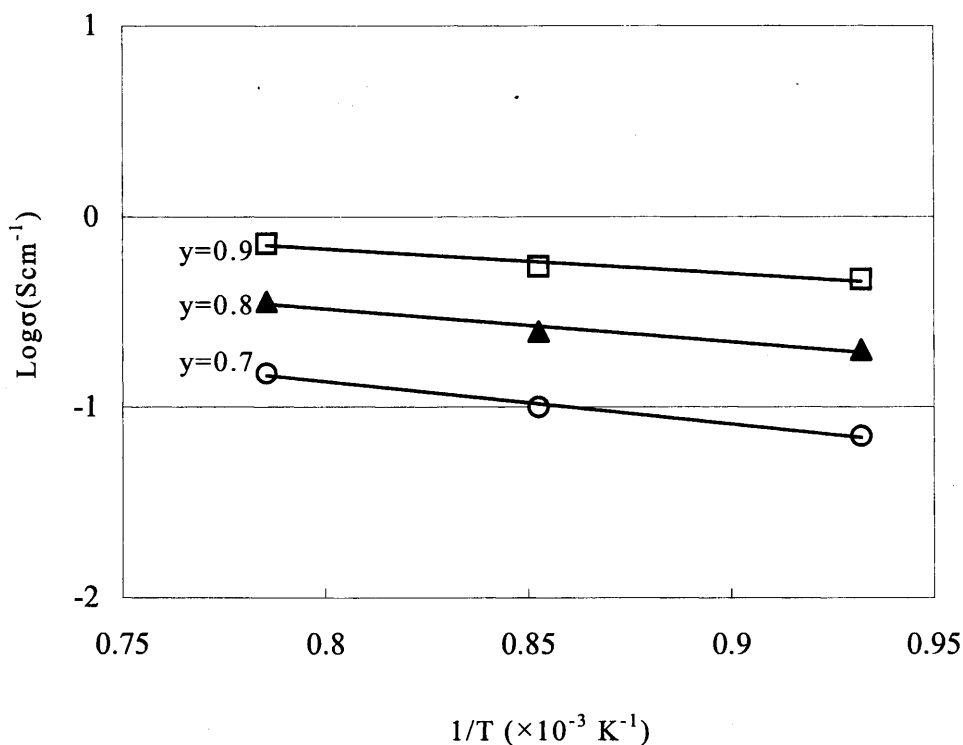


Fig.3-4. Temperature dependence of the oxygen ionic conductivity of $\text{La}_{0.6}\text{Sr}_{0.4}\text{Ti}_{1-y}\text{Fe}_y\text{O}_{3-\delta}$. The P_{O_2} was around 10^{-18} Pa.

Figure 3-5 shows the compositional map of the electrical conductivity of $\text{La}_{1-x}\text{Sr}_x\text{Ti}_{1-y}\text{Fe}_y\text{O}_{3-\delta}$ at 800°C , for (a) electronic conduction at air atmosphere and (b) ionic conduction. The $\text{La}_{0.6}\text{Sr}_{0.4}\text{Ti}_{0.1}\text{Fe}_{0.9}\text{O}_{3-\delta}$ composition was optimized to have the maximum electronic and ionic conductivities.

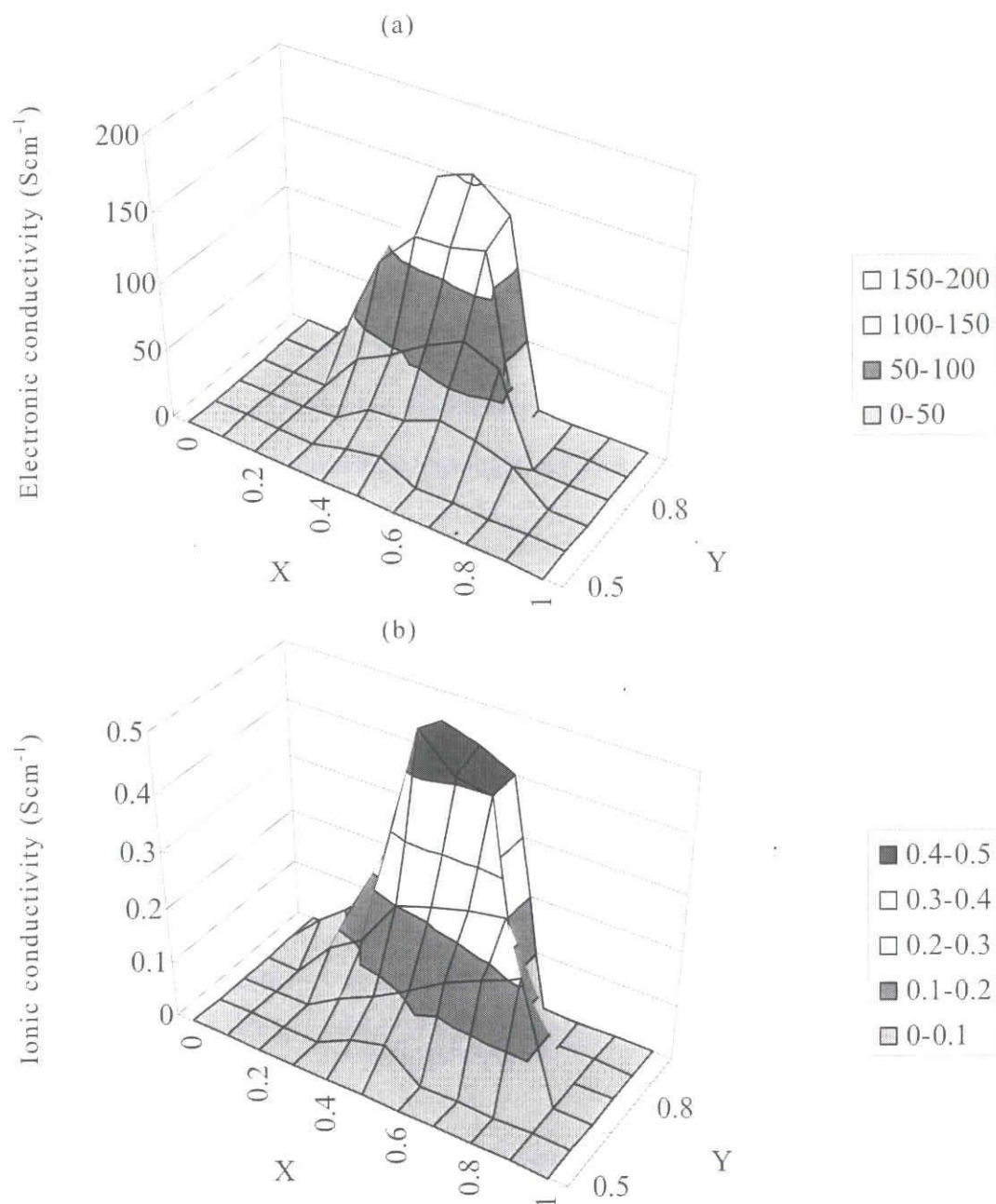


Fig.3-5. Compositional map of electrical conductivity of $\text{La}_{1-x}\text{Sr}_x\text{Ti}_{1-y}\text{Fe}_y\text{O}_{3-\delta}$ at 800°C , (a) electronic conduction at air atmosphere and (b) ionic conduction.

We tested the $\text{La}_{0.6}\text{Sr}_{0.4}\text{Ti}_{0.1}\text{Fe}_{0.9}\text{O}_{3-\delta}$ membrane (0.5 mm thick) at 900°C for oxygen permeation performance with methane/air. The rate of oxygen permeation was fairly good at 10 cc/min/cm^2 or better, where the conversion of CH_4 and selectivity of CO of this membrane were 62.3% and 99.9%, respectively. This CH_4 conversion ratio is much higher than the previously reported for perovskite oxides⁵⁾, and it is considered due to the high oxygen permeation of the membrane. And also, considering high CO selectivity, the catalyst was matched for LSTF membranes.

However, after one hour, cracks appeared in the membrane, and we identified extensive leaks. The cause might be that the thermal expansion coefficient of $\text{La}_{0.6}\text{Sr}_{0.4}\text{Ti}_{0.1}\text{Fe}_{0.9}\text{O}_{3-\delta}$ may be large.

Figure 3-6 shows the compositional mapping of the thermal expansion coefficient, E_{air} , of LSTF. The E_{air} of LSTF was changed from 10.8 to $17.0 (\times 10^{-6}/\text{K}^{-1})$, and that of $\text{La}_{0.5}\text{Sr}_{0.5}\text{FeO}_{3-\delta}$ was the highest, $17.0 \times 10^{-6}/\text{K}^{-1}$, in this study. Compositions displaying high conductivity exhibited large coefficients of thermal expansion. The E_{air} values of samples with lower La compositions are similar to those of other Ti-substituted perovskites. The thermal expansion coefficient of $9.3 (\times 10^{-6}/\text{K}^{-1})$ over the temperature range of 800 to 1200°C has been reported for $\text{La}_{0.2}\text{Sr}_{0.8}\text{Fe}_{0.55}\text{Ti}_{0.45}\text{O}_{3-x}$ by Park et al.³⁷⁾ In a recent report,³⁸⁾ E_{air} of the LSTF system was reported to be as high as 21 to $26 (\times 10^{-6}/\text{K}^{-1})$ over the temperature range of 700 to 1200°C , increased by Ti substitution in the perovskite structure lattice.

Usually, the oxygen-permeable membranes are formed as thin films on porous ceramic supports, and the matching of their thermo mechanical properties to those of porous support is also important. Typical ceramic porous support materials are stabilized zirconia, cerium oxide, and magnesium oxide, and their thermal expansion coefficients are from 9 to $13 (\times 10^{-6}/\text{K}^{-1})$. In the range of compositions investigated in this study, $\text{La}_{0.6}\text{Sr}_{0.4}\text{Ti}_{0.3}\text{Fe}_{0.7}\text{O}_{3-\delta}$ was the optimal composition that had a good trade-off of the high ion conductivity and moderate mechanical stability of thermal expansion.

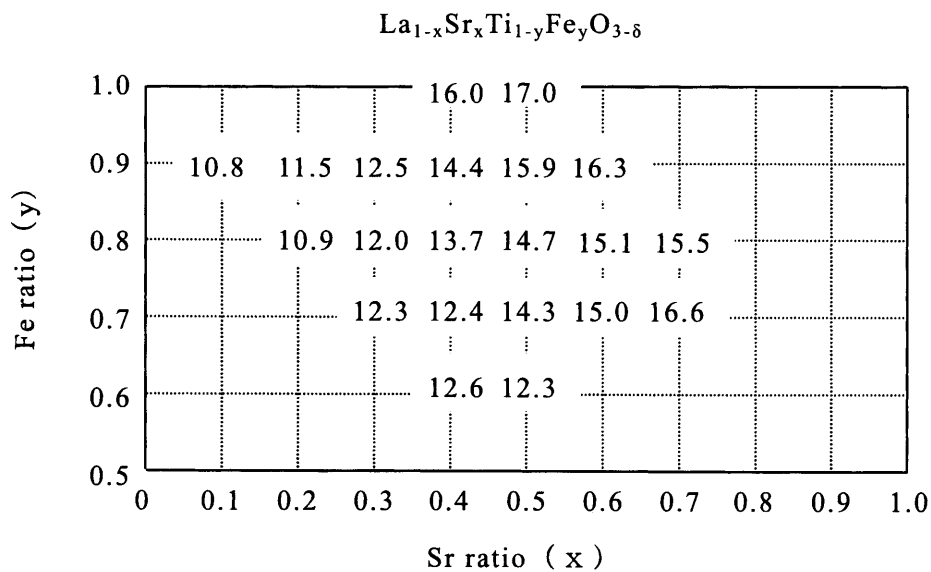


Fig.3-6. Thermal expansion coefficient map of $\text{La}_{1-x}\text{Sr}_x\text{Ti}_{1-y}\text{Fe}_y\text{O}_{3-\delta}$ (800°C).

3.3.2. Oxygen permeation performance of $\text{La}_{0.6}\text{Sr}_{0.4}\text{Ti}_{0.3}\text{Fe}_{0.7}\text{O}_{3-\delta}$

Figure 3-7 shows the relationship between ion conductivity and oxygen permeation rates for each composition of $\text{LaSrTiFeO}_{3-\delta}$. Ion conductivity and oxygen permeation rates are nearly proportional, suggesting that the ion conductivity of the oxygen-permeable membrane material controls the membrane permeation rate.

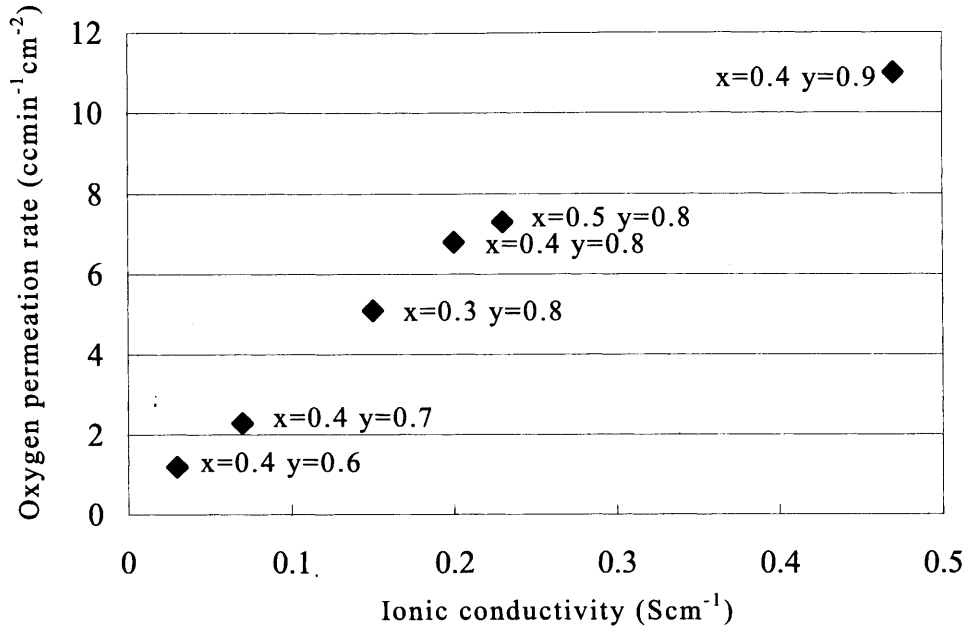


Fig.3-7. Relationship between ion conductivity and oxygen permeation rate of $\text{La}_{1-x}\text{Sr}_x\text{Ti}_{1-y}\text{Fe}_y\text{O}_{3-\delta}$ membrane.

Considering the surface reaction to be sufficiently fast or fully activated, the rate of oxygen permeation j_{O_2} can be expressed by

$$j_{\text{O}_2} = \frac{1}{2FZ_{\text{ion}}} \times j_{\text{ion}} = \frac{1}{4F} \times \sigma_{\text{ion}} \times \frac{E}{L} \quad (2)$$

where F is the Faraday constant, Z_{ion} is the charge of the ion, σ_{ion} is the conductivity of the ion, L is the membrane thickness, and E is the applied voltage across the membrane induced by the difference in oxygen partial pressure. Using Nernst's equation, j_{O_2} can be expressed in a different form,

$$j_{\text{O}_2} = \frac{1}{4FL} \times \sigma_{\text{ion}} \times \frac{RT}{4F} \ln \left(\frac{P_{\text{O}_2}^h}{P_{\text{O}_2}^l} \right) \quad (3)$$

where R , T , $P_{\text{O}_2}^h$, and $P_{\text{O}_2}^l$, are the gas constant, absolute temperature, oxygen-ion

conductivity, oxygen partial pressure on the air side, and oxygen partial pressure on the permeation side, respectively. The measured permeation rate of the sample and the estimation calculated using Eq.(3) are listed in Table 3-1.

Table 3-1. Oxygen permeation rate of $\text{LaSrTiFeO}_{3-\delta}$ at $T=900\text{ }^\circ\text{C}$, membrane thickness $L=0.5\text{mm}$. The calculated value was estimated under the condition that PO_2^h and PO_2^l are 0.021 and 1.0×10^{-24} MPa, respectively.

Samples	Oxygen permeation rate (cc/min/cm ²)	
	Calculated	Measured
$\text{La}_{0.6}\text{Sr}_{0.4}\text{Ti}_{0.1}\text{Fe}_{0.9}\text{O}_{3-\delta}$	28	11
$\text{La}_{0.6}\text{Sr}_{0.4}\text{Ti}_{0.3}\text{Fe}_{0.7}\text{O}_{3-\delta}$	6.3	2.3

The $\text{La}_{0.6}\text{Sr}_{0.4}\text{Ti}_{0.1}\text{Fe}_{0.9}\text{O}_{3-\delta}$ sample showed a rate 4.4 or 4.8 times higher than that of the $\text{La}_{0.6}\text{Sr}_{0.4}\text{Ti}_{0.3}\text{Fe}_{0.7}\text{O}_{3-\delta}$ sample, and this difference corresponds well with the estimated values, i.e., the difference in the ionic conductivities. For the deviation between the calculated and measured data of permeation rate, it is supposed that the actual values of oxygen partial pressure on the membrane surface were different from the thermodynamic equilibrium value. Considering the 2.64 times lower permeation rate, j_{O_2} , the $\text{PO}_2^h/\text{PO}_2^l$ is thought to be 14 times lower. If the rate of surface reaction is sufficiently fast, the oxygen partial pressure on the permeation side is considered to be approximately one order higher than the thermodynamic equilibrium value, 7.1×10^{-16} Pa, obtained from the gas composition and the temperature.

If the ion diffusivity or mobility, μ_{ion} , is unchanged, then the ion conductivity is

a function of ion concentration, c_{ion} , which, in turn, is temperature dependent with activation energy E_a , as discussed above:

$$\sigma_{ion} = e \times \mu_{ion} \times c_{ion} \propto \exp\left(-\frac{E_a}{RT}\right) \quad (4)$$

Then the equation above can be written as

$$j_{O_2} = A \frac{T}{L} \times \exp\left(-\frac{E_a}{RT}\right) \times \ln\left(\frac{P_{O_2}^h}{P_{O_2}^l}\right) \quad (5)$$

Figure 3-8 shows the dependence of the oxygen permeation rate with the parameter of the thickness of the $La_{0.6}Sr_{0.4}Ti_{0.3}Fe_{0.7}O_{3-\delta}$ membrane. From this temperature dependence of the oxygen permeation rate of the $La_{0.6}Sr_{0.4}Ti_{0.3}Fe_{0.7}O_{3-\delta}$ sample, at 800, 900, and 1000°C, the pre-exponential factor A and the activation energy E_a can be estimated to be $5.17 \times 10^{-10} \text{ mol}/(\text{cm} \cdot \text{s} \cdot \text{K})$ and 35 kJ/mol, respectively.

Thinner membranes enhance the oxygen permeation rates. The maximum permeation rate achieved was $13.8 \text{ cc}/\text{min}/\text{cm}^2$, which is an extraordinary value, considering that oxygen permeation rates exceeding $10 \text{ cc}/\text{min}/\text{cm}^2$ are rarely achieved for self-supporting membranes. For membrane thicknesses of 0.5 mm to 0.1 mm, the oxygen permeation rate increases linearly in proportion to the reciprocal of membrane thickness, which is in good correspondence with Eq. (5). This confirms that oxide conductivity is dominant in the behavior of the membrane within this range of thicknesses. Table 3-2 shows the effects of membrane thickness for CH_4 conversion and CO selectivity. The CH_4 conversion increases with decreasing membrane thickness. And CO selectivity did not depend on membrane thickness. Therefore, it is considered that the CH_4 conversion further improved by increasing oxygen permeation rate.

Table 3-2. Effects of membrane thickness of $\text{La}_{0.6}\text{Sr}_{0.4}\text{Ti}_{1-y}\text{Fe}_y\text{O}_{3-\delta}$ on the ratio of CH_4 conversion and the CO selectivity at working temperature of 900 °C.

Substitution by Fe (y)	Membrane thickness (mm)	Conversion of CH_4 (%)	Selectivity of CO (%)	Oxygen permeation rate ($\text{cc}/\text{min}/\text{cm}^2$)
0.7	0.1	60.0	99.9	10.5
0.7	0.2	32.6	99.9	5.8
0.7	0.3	21.2	99.9	3.8
0.7	0.5	13.0	99.9	2.3
0.9	0.5	62.3	99.9	11.0

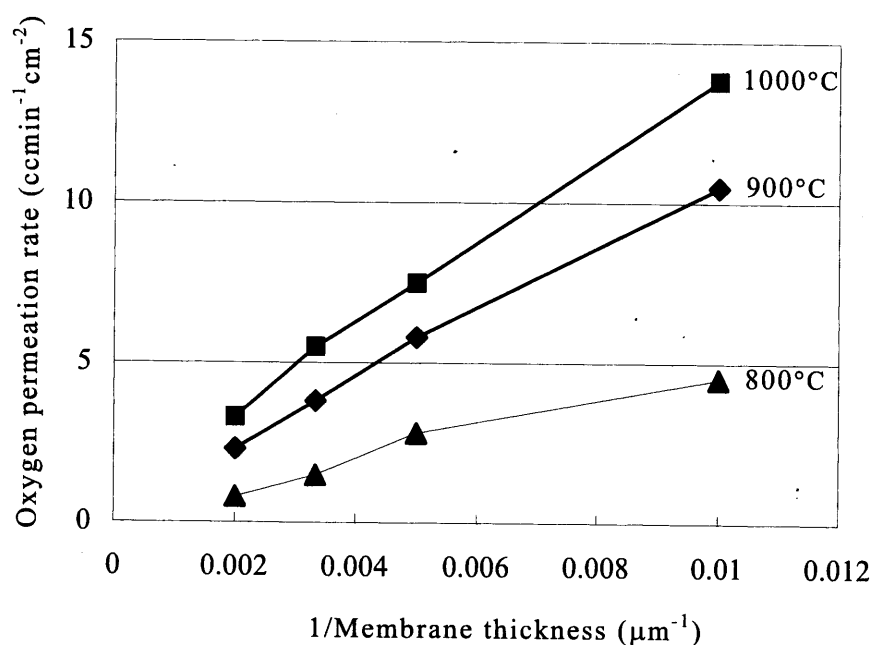


Fig.3-8. Relationship between membrane thickness and oxygen permeation rate of $\text{La}_{0.6}\text{Sr}_{0.4}\text{Ti}_{0.3}\text{Fe}_{0.7}\text{O}_{3-\delta}$ membrane.

The membranes in this study showed no gas leakage due to membrane damage throughout the 10h operation. However, failure of the membrane can occur with cyclic operation between air and reducing atmosphere. The durability of the

membrane material itself in a reducing atmosphere has direct consequences on membrane failure, regardless of the oxygen permeation rate.

To control both oxygen permeation and mechanical stability, further study on the expansion rate in reducing atmosphere, taking into consideration the stress generated by the difference in expansion rates on the oxidized side and the reducing side of the membrane, is necessary. It will be discussed at chapter 4.

3.4. Conclusion

The substitution of A-site alkali ions and B-site transition metal ions of the perovskite oxide oxygen-permeating membrane system of $\text{La}_{1-x}\text{Sr}_x\text{Ti}_{1-y}\text{Fe}_y\text{O}_{3-\delta}$, (LSTF) have been studied for their application to the partial oxidation of methane to syngas. The electrical conductivity of the LSTF was strongly dependent on the oxygen partial pressure, P_{O_2} . Both the substitution of Fe for Ti, and the substitution of Sr for La increased the p-type electronic and oxygen ionic conductivities to 155 and 0.47 Scm^{-1} respectively. From 800 to 1000°C , the temperature dependence of conductivity has been studied, and the thermal activation energy of the p-type electronic conductivity of $\text{La}_{0.6}\text{Sr}_{0.4}\text{Ti}_{0.1}\text{Fe}_{0.9}\text{O}_{3-\delta}$ was found to be 38 kJ/mol and those of the ionic conductivity of $\text{La}_{0.6}\text{Sr}_{0.4}\text{Ti}_{1-y}\text{Fe}_y\text{O}_{3-\delta}$ ($y=0.7$ and 0.9) were 11 and 20 kJ/mol. The thermal expansion coefficients of LSTF were varied from 10.8 to $17.0 (\times 10^{-6}/\text{K}^{-1})$ by increasing the Fe substitution. $\text{La}_{0.6}\text{Sr}_{0.4}\text{Ti}_{0.3}\text{Fe}_{0.7}\text{O}_{3-\delta}$ was the optimized composition with a good trade-off of the high ion conductivity, 0.07 Scm^{-1} , and good matching of the thermal expansion coefficient, $12.4 \times 10^{-6}/\text{K}^{-1}$. It has been tested for the partial oxidation of methane to syngas and shows a high oxygen permeation rate of 13.8 cc/min/cm^2 at 1000°C or 10.5 cc/min/cm^2 at 900°C . In addition, High values of CH_4 conversion and CO selectivity were confirmed at 900°C , 60.0 % and 99.9 % respectively. For membrane thicknesses of 0.5 mm to 0.1 mm, the oxygen permeation rate increases linearly in proportion to the reciprocal of membrane thickness.

4. In situ analysis of $\text{La}_{0.6}\text{Sr}_{0.4}\text{Ti}_{0.1}\text{Fe}_{0.9}\text{O}_{3-\delta}$ and $\text{La}_{0.6}\text{Sr}_{0.4}\text{Ti}_{0.3}\text{Fe}_{0.7}\text{O}_{3-\delta}$ oxygen ion conductors

4.1. Introduction

In the chapter 3, the highest ionic conductivity was obtained with the composition of $\text{La}_{0.6}\text{Sr}_{0.4}\text{Ti}_{0.1}\text{Fe}_{0.9}\text{O}_{3-\delta}$ reaching the oxygen permeation rate over $10\text{cc}/\text{min}/\text{cm}^2$ at $1000\text{ }^\circ\text{C}$ with the membrane thickness of 0.5 mm . However, low thermal stability in high-temperature operation is a problem of this composition when it is used as tube. The $\text{La}_{0.6}\text{Sr}_{0.4}\text{Ti}_{0.1}\text{Fe}_{0.9}\text{O}_{3-\delta}$ membrane tube was broken during the operation of methane partial oxidation, as shown Figure 4-1. This fracture is caused by the strain across the tubes, owing to the difference between expansions at different P_{O_2} 's, as reported by Pei et al.¹⁶⁾. On the other hand, the composition of $\text{La}_{0.6}\text{Sr}_{0.4}\text{Ti}_{0.3}\text{Fe}_{0.7}\text{O}_{3-\delta}$ showed both relatively high ion conductivity and enough high thermal stability. The membrane of this composition showed the oxygen permeation rate of $13.8\text{ cc}/\text{min}/\text{cm}^2$ at $1000\text{ }^\circ\text{C}$ (membrane thickness 0.1 mm) with no gas leakage.

The chemical or crystallographic stability at the micro-level and the structural stability at the macro-level of these LSTF compositions at high temperature, reducing, low- P_{O_2} , environment are very critical issues for the application of ion transport membranes. This material property is an important index of the durability in cyclic operation up to high temperature and also a critical information of the lattice and thermal matching to the porous support materials.

In this study, we have investigated the thermal expansions of two oxide bulk membrane samples of $\text{La}_{0.6}\text{Sr}_{0.4}\text{Ti}_{0.1}\text{Fe}_{0.9}\text{O}_{3-\delta}$ and $\text{La}_{0.6}\text{Sr}_{0.4}\text{Ti}_{0.3}\text{Fe}_{0.7}\text{O}_{3-\delta}$ using a dilatometer, and also carried out an in situ XRD analysis of these two compositions, in both a reducing atmosphere and air at a high temperature of $1000\text{ }^\circ\text{C}$. To understand how the chemical bonding in LSTF with a perovskite structure has change in various atmospheres, the crystal structures of LSTF were refined using XRD data, and the results are discussed and compared to the dilatometric results.

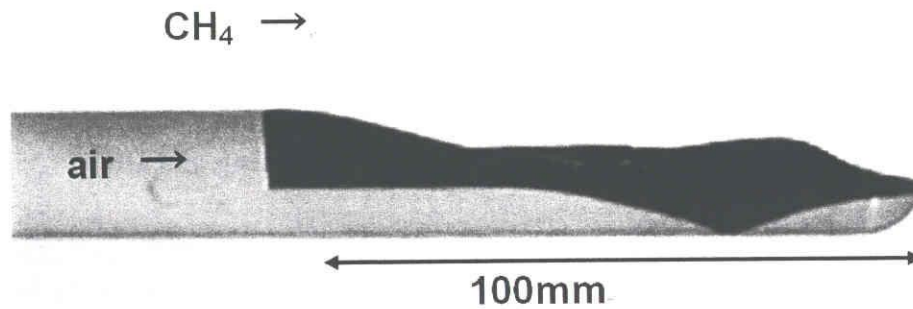


Fig.4-1. The photograph of breakage in tube type membrane of $\text{La}_{0.6}\text{Sr}_{0.4}\text{Ti}_{0.1}\text{Fe}_{0.9}\text{O}_{3-\delta}$ for CH_4 partial oxidation test.

4.2. Experimental

The thermal expansion of the sintered samples, $\text{La}_{0.6}\text{Sr}_{0.4}\text{Ti}_{1-x}\text{Fe}_x\text{O}_{3-\delta}$ ($x=0.3 \sim 0.9$), in reducing atmosphere (4% hydrogen and 96 vol.% nitrogen) ($\Delta L/L_{\text{red}}$) and the thermal expansion in air ($\Delta L/L_{\text{air}}$) in the range of temperatures between 25 and 1000°C were measured using a dilatometer, Rigaku TMA8310. The difference in expansion between the two atmospheres is expressed as a differential expansion ratio by a dilatometer, $E_{\text{r-dil}}$, by

$$E_{\text{r-dil}} (\%) = (\text{difference between expansion ratios in reducing and air atmospheres}) \\ = (\Delta L/L_{\text{red}} - \Delta L/L_{\text{air}}) / (1 + \Delta L/L_{\text{air}}) \times 100.$$

The crystal structures of LSTF membranes were analyzed by in situ XRD (Rigaku RINT2000) analysis for the two compositions of $\text{La}_{0.6}\text{Sr}_{0.4}\text{Ti}_{1-x}\text{Fe}_x\text{O}_{3-\delta}$ ($x=0.7$ and 0.9) by the following steps. i) at 25 °C in air, ii) at 1000 °C in air, iii) at 1000 °C in a reducing atmosphere of 4% hydrogen and 96 vol.% nitrogen, and iv) at 25 °C in air. Using the XRD patterns, Rietveld refinement³⁹⁾ calculation was carried out to obtain

the precise lattice parameters with the code of Rigaku PDXL. With the calculated crystal structure data, the ratio of the changes in unit cell volume, (E_{r-xc}), is also defined by,

$$E_{r-xc} (\%) = \frac{\text{(difference between unit cell volumes in reducing and air)}}{\text{(unit cell volume in air)}} \times 100.$$

4.3. Results and Discussion

The dilatometric thermal expansion curves of $\text{La}_{0.6}\text{Sr}_{0.4}\text{Ti}_{0.1}\text{Fe}_{0.9}\text{O}_{3-\delta}$, LSTF-9, and $\text{La}_{0.6}\text{Sr}_{0.4}\text{Ti}_{0.3}\text{Fe}_{0.7}\text{O}_{3-\delta}$, LSTF-7, in air and the reducing atmospheres up to 1000 °C are shown in Figure 4-2. The thermal expansion coefficients, *TECs*, of the samples of LSTF-9 and LSTF-7 are 14.4 and $12.4 \times 10^{-6} \text{ K}^{-1}$, respectively. These *TECs* of LSTF are much smaller than those reported by Park et al. ($\text{La}_{0.6}\text{Sr}_{0.4}\text{Ti}_x\text{Fe}_{1-x}\text{O}_{3-\delta}$, where $x = 0.2$ and 0.3)³⁸, $21 - 26 \times 10^{-6} \text{ K}^{-1}$ measured in air in the temperature range of 700–1000°C. In this report, the dilatometric curves of LSTF in reduced and high temperature are also plotted, showing very typical behavior of expansion in reducing atmosphere, and for both LSTF compositions, remarkable increases in expansion in the reducing atmosphere were observed at temperatures over 600 °C.

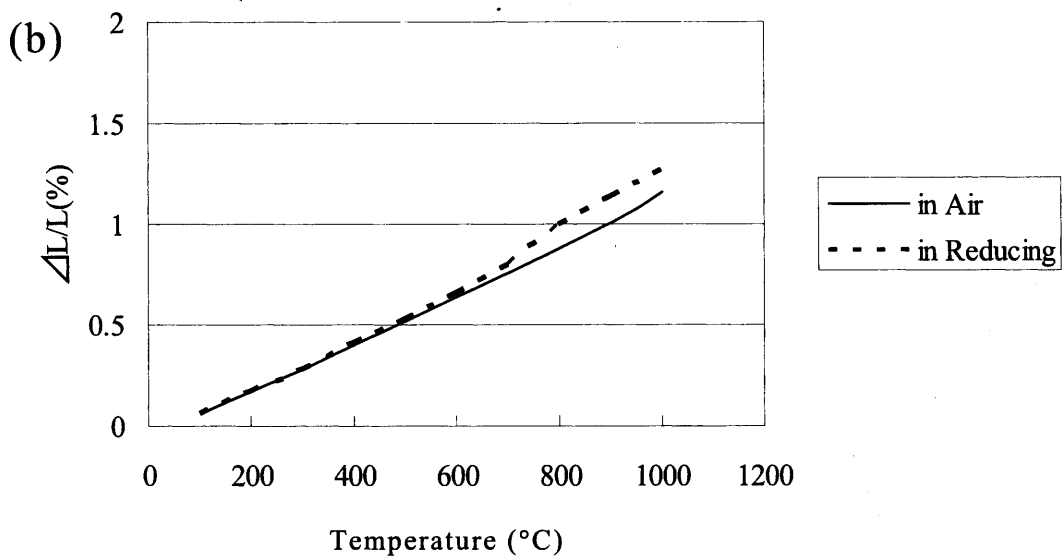
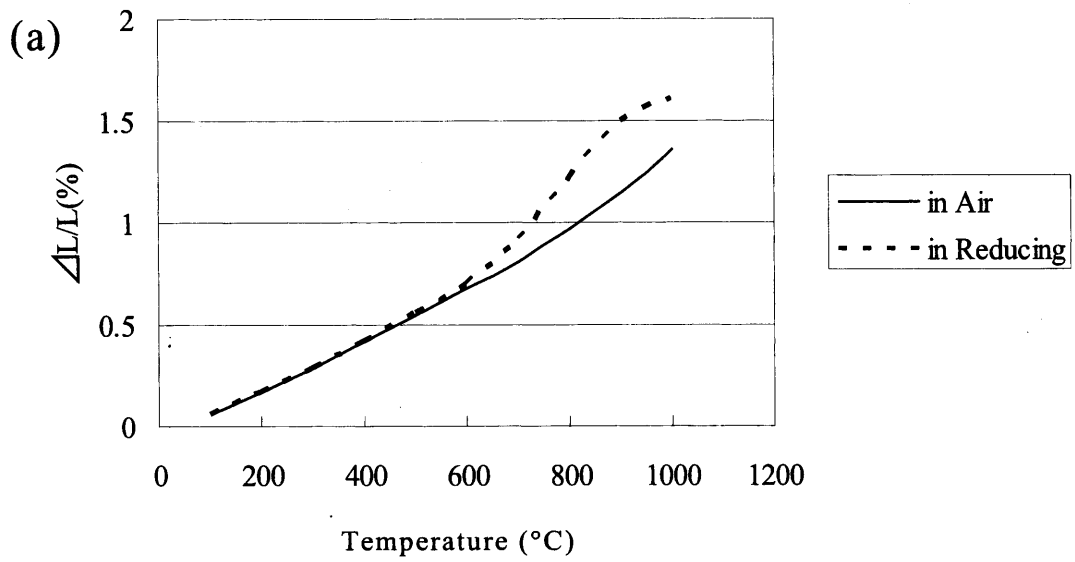


Fig.4-2. The thermal expansion curves of (a) $\text{La}_{0.6}\text{Sr}_{0.4}\text{Ti}_{0.1}\text{Fe}_{0.9}\text{O}_{3-\delta}$ and (b) $\text{La}_{0.6}\text{Sr}_{0.4}\text{Ti}_{0.3}\text{Fe}_{0.7}\text{O}_{3-\delta}$ in air and reducing atmosphere.

The differential expansion ratio, E_{r-dil} , of these LSTF can be calculated from the data curves in Figure 4-2, as listed in Table 4-1. The E_{r-dil} of the LSTF-9 and LSTF-7 are 0.4 and 0.1%. The differences result from the difference in stability for the reducing atmosphere. Previously, Park et al.³⁷⁾ reported the thermal expansions ratio of $\text{La}_{0.2}\text{Sr}_{0.8}\text{Ti}_{0.45}\text{Fe}_{0.55}\text{O}_{3-\delta}$ in air and a reducing atmosphere up to 841 °C using dilatometer. The E_{r-dil} of $\text{La}_{0.2}\text{Sr}_{0.8}\text{Ti}_{0.45}\text{Fe}_{0.55}\text{O}_{3-\delta}$ estimated from Park et al.'s dilatometric data is about 0.2 % ($10^{-5} \text{ atm} \leq P_{\text{O}_2} \leq 0.21 \text{ atm}$). Although partial oxygen pressures in reducing atmosphere are subtly different ($10^{-15} \text{ atm} \leq P_{\text{O}_2} \leq 0.21 \text{ atm}$), the E_{r-dil} is the same order of magnitude.

Table 4-1. The E_r of $\text{La}_{0.6}\text{Sr}_{0.4}\text{Ti}_{0.1}\text{Fe}_{0.9}\text{O}_{3-\delta}$ and $\text{La}_{0.6}\text{Sr}_{0.4}\text{Ti}_{0.3}\text{Fe}_{0.7}\text{O}_{3-\delta}$

	E_{r-dil} calculated from dilatometer (%)	E_{r-xc} calculating from XRD refinement crystal cell volume (%)	$\sqrt[3]{E_{r-xc}}$
$\text{La}_{0.6}\text{Sr}_{0.4}\text{Ti}_{0.1}\text{Fe}_{0.9}\text{O}_{3-\delta}$	0.40	0.80	0.27
$\text{La}_{0.6}\text{Sr}_{0.4}\text{Ti}_{0.3}\text{Fe}_{0.7}\text{O}_{3-\delta}$	0.10	0.39	0.13
$\text{La}_{0.2}\text{Sr}_{0.8}\text{Ti}_{0.45}\text{Fe}_{0.55}\text{O}_{3-\delta}$ 37)	0.20	-	-

In this study, the E_{r-dil} 's for the wide substitution change from Ti to Fe in $\text{La}_{0.6}\text{Sr}_{0.4}\text{Ti}_{1-x}\text{Fe}_x\text{O}_{3-\delta}$ have been investigated and plotted in Figure 4-3. Since an increase in Ti content was found to reduce E_{r-dil} , Ti substitution appears to improve membrane durability in a reducing atmosphere. We tested the oxygen permeation of $\text{La}_{0.6}\text{Sr}_{0.4}\text{Ti}_{1-x}\text{Fe}_x\text{O}_{3-\delta}$ membranes. No leaks were confirmed during oxygen permeation measurements (methane/air) for compositions exhibiting an E_{r-dil} of 0.1% or lower ($\text{La}_{0.6}\text{Sr}_{0.4}\text{Ti}_{0.3}\text{Fe}_{0.7}\text{O}_{3-\delta}$, $\text{La}_{0.6}\text{Sr}_{0.4}\text{Ti}_{0.4}\text{Fe}_{0.6}\text{O}_{3-\delta}$), even after 10 h. Other two

samples of high E_{r-dil} were broken during the test. We concluded that cracks in the LSTF membrane resulted from the stress generated by the difference between the expansions on the air and reducing atmosphere sides of the membrane.

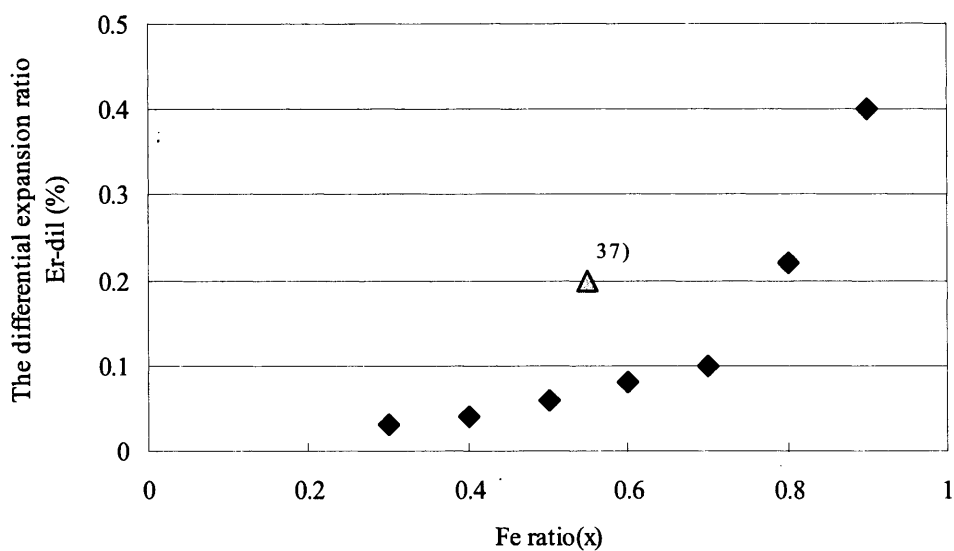


Fig.4-3. The E_{r-dil} for the compositions of $La_{0.6}Sr_{0.4}Ti_{1-x}Fe_xO_{3-\delta}$ ($x = 0.3 \sim 0.9$).

Figure 4-4 shows the XRD patterns of $La_{0.6}Sr_{0.4}Ti_{0.1}Fe_{0.9}O_{3-\delta}$ and $La_{0.6}Sr_{0.4}Ti_{0.3}Fe_{0.7}O_{3-\delta}$, in four different atmospheres. A shift of the peak towards the low angle (or larger d-spacing) occurred in a low- P_{O_2} , reducing atmosphere, showing that the oxide sample expands substantially. Previous report ¹⁶⁾ on a similar composition ($SrCo_{0.8}Fe_{0.2}O_3$) explained that this type of expansion is due to a cubic-to-orthorhombic phase transition.

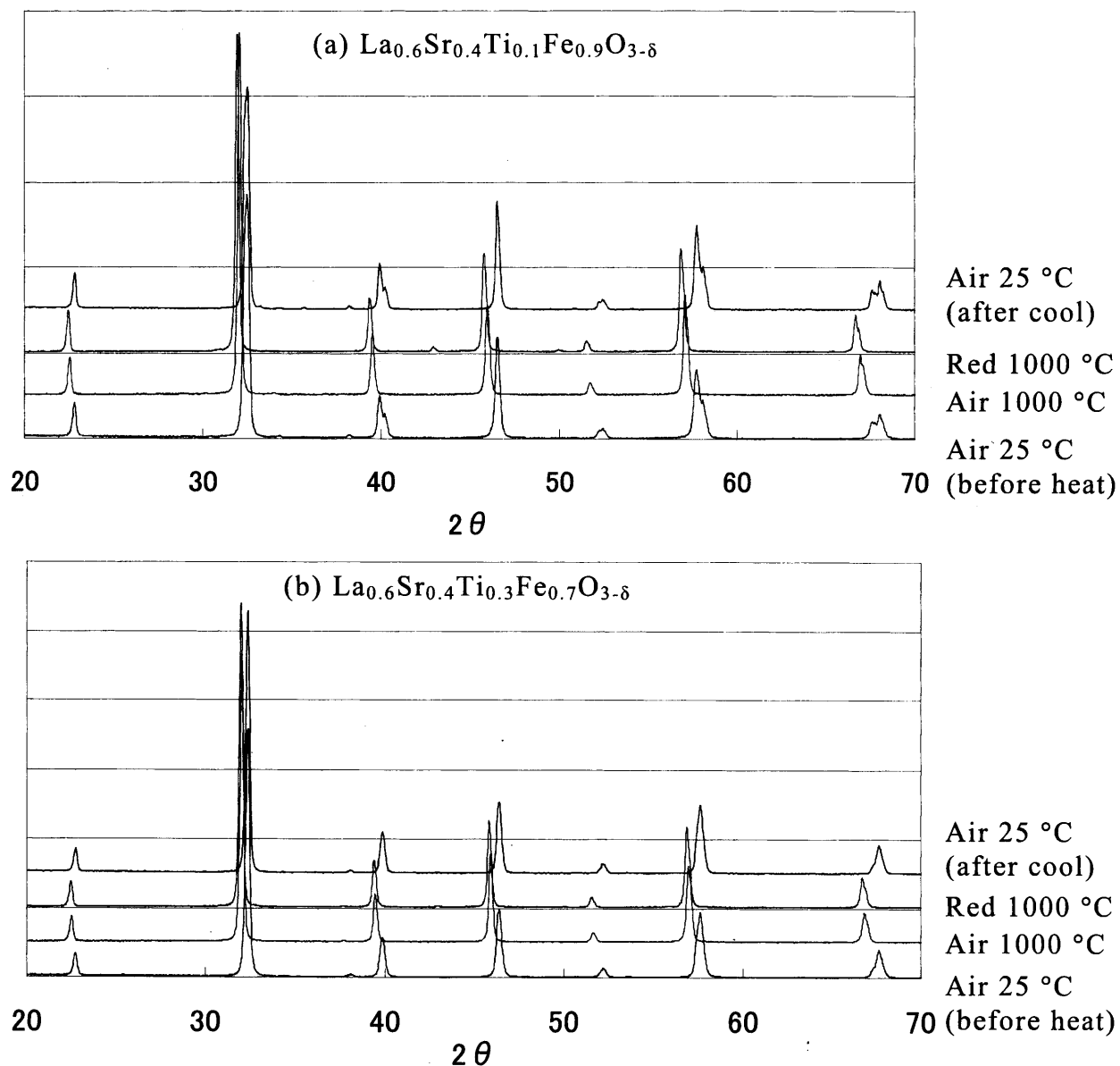


Fig.4-4. XRD pattern of (a) $\text{La}_{0.6}\text{Sr}_{0.4}\text{Ti}_{0.1}\text{Fe}_{0.9}\text{O}_{3-\delta}$ (b) $\text{La}_{0.6}\text{Sr}_{0.4}\text{Ti}_{0.3}\text{Fe}_{0.7}\text{O}_{3-\delta}$ oxygen permeable membrane.

The lattice parameters and unit cell volumes of two samples refined from the Rietveld analysis are listed in Table 4-2. For comparison, The data of $\text{La}_{0.48}\text{Sr}_{0.48}\text{Ti}_{0.6}\text{Fe}_{0.4}\text{O}_{3-\delta}$ in air at room temperature reported by Fagg et al.⁴⁰⁾ are also included in the table, and the linear thermal expansion rate estimated from volume change, $\sqrt[3]{E_{r-xc}}$, is also listed.

From results of this analysis, we found the following: first, two compositions match with the orthorhombic structure having a space group of *Pnma*, independent of P_{O_2} and temperature. Second, the larger increase in cell volume in the reducing atmosphere of $\text{La}_{0.6}\text{Sr}_{0.4}\text{Ti}_{0.1}\text{Fe}_{0.9}\text{O}_{3-\delta}$ compared with that of $\text{La}_{0.6}\text{Sr}_{0.4}\text{Ti}_{0.3}\text{Fe}_{0.7}\text{O}_{3-\delta}$ is correlated with the difference in fracture behavior between these two compositions.

Figure 4-5 shows a schematic crystal lattice of $\text{La}_{0.6}\text{Sr}_{0.4}\text{Ti}_{0.1}\text{Fe}_{0.9}\text{O}_{3-\delta}$. The crystal structure of this perovskite is particularly interesting since the c-axis lattice parameter increases with Ti-to-Fe substitution and possibly with the formation of oxygen defects.

This effect of cation substitution, Ti-to-Fe, is compared with the reported data of the same perovskite series, as plotted in Figure 4-6. The lattice parameters of $\text{La}_{0.6}\text{Sr}_{0.4}\text{TiO}_3$, which was calculated from the linear estimation using the data of LaTiO_3 (ICDD 49-0426) and SrTiO_3 (ICDD35-0734), and that of $\text{La}_{0.7}\text{Sr}_{0.3}\text{FeO}_{3-\delta}$ (ICDD89-1269) are plotted at the composition of $x=0$ and 1.0, respectively. The lattice parameter increased with the substitution of Fe, in the range of $x=0.7$ to 1.0. This trend is understood from the fact that the Ti^{4+} has a smaller ionic radius than the Fe^{3+} .

Table4-2. Lattice parameters and unit cell volume of LSTF sintered samples

samples	Atmosphere	a (Å)	b (Å)	c (Å)	Unit cell Volume, V_{xc} (Å ³)	$\sqrt[3]{V_{xc}}$	$\sqrt[3]{E_{r-xc}}$
La _{0.6} Sr _{0.4} Ti _{0.1} Fe _{0.9} O _{3-δ}	25 °C in air (before heating)	5.5318	5.5600	7.8199	240.5	6.2176	0.27
	1000 °C in air	5.6070	5.5907	7.9148	248.1	6.2825	
	1000 °C in a reducing atmosphere	5.6225	5.6074	7.9331	250.1	6.2993	
	25 °C in air (after cooling)	5.5318	5.5593	7.8213	240.5	6.2176	
La _{0.6} Sr _{0.4} Ti _{0.3} Fe _{0.7} O _{3-δ}	25 °C in air (before heating)	5.4591	5.5483	7.8016	236.3	6.1812	0.13
	1000 °C in air	5.5950	5.5940	7.8970	247.2	6.2748	
	1000 °C in a reducing atmosphere	5.6098	5.5951	7.9062	248.2	6.2833	
	25 °C in air (after cooling)	5.5006	5.5522	7.8040	238.3	6.1986	
La _{0.48} Sr _{0.48} Ti _{0.6} Fe _{0.4} O _{3-δ} 40)	in air	5.514	5.532	7.829	238.8	6.2030	-

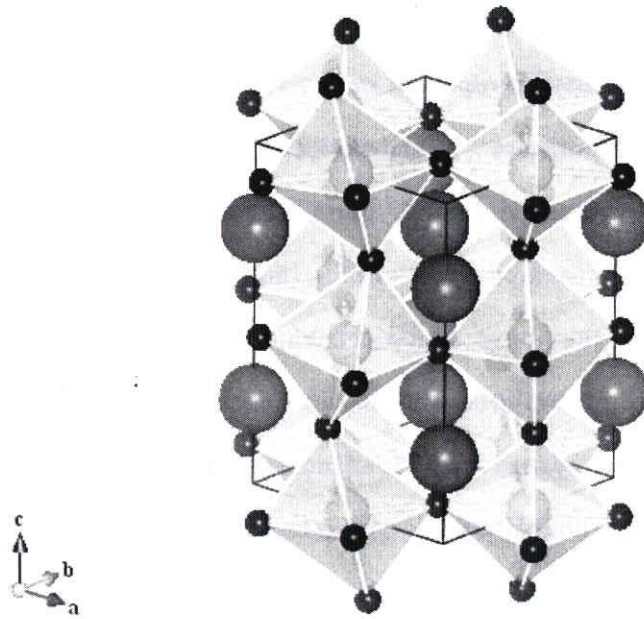


Fig.4-5. $\text{La}_{0.6}\text{Sr}_{0.4}\text{Ti}_{0.1}\text{Fe}_{0.9}\text{O}_{3-\delta}$ crystal structure, drawn by VESTA⁴¹⁾. Oxygen is small, A is big, and B is medium spheres in ABO_3 crystal structure.

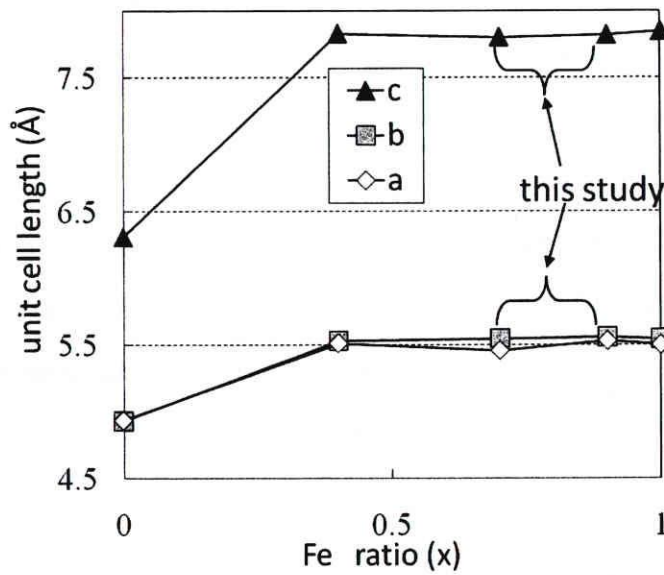


Fig.4-6. Unit cell length of $\text{La}_{0.6}\text{Sr}_{0.4}\text{Ti}_{1-x}\text{Fe}_x\text{O}_{3-\delta}$. $x=4$ is data of $\text{La}_{0.48}\text{Sr}_{0.48}\text{Ti}_{1-x}\text{Fe}_x\text{O}_{3-\delta}$ (from Ref. 40).

It is noticeable that the lattice parameter and unit cell increased further at a low P_{O_2} as shown in Table 4-2, which understood as a typical isothermal expansion followed by oxygen vacancy formation reported in other oxides such as $LaMnO_3$ ⁴²⁾.

Furthermore, the Fe substitution increased the Fe^{3+} cation coordinated by less than six anions, in other words, increased the oxygen vacancies. From the transport properties of the two components of $La_{0.6}Sr_{0.4}Ti_{0.1}Fe_{0.9}O_{3-\delta}$ and $La_{0.6}Sr_{0.4}Ti_{0.3}Fe_{0.7}O_{3-\delta}$ ⁴³⁾, both the ionic and electrical conductivity of the former were 5 times higher than those of the later at 900°C, which is due to the difference in defect concentration of mobile oxygen vacancies. Increasing anion deficiency leads to an increase in cell volume, probably owing to the enhancement of both anion and cation repulsions in the lattice.

The oxygen defect of the oxides have been investigated by TG-DTA measurements between room temperature and 1000°C in the range of error of 0.05% ($\Delta W/W$). The oxygen deficiency, δ , was 0.19 and 0.17 in the $La_{0.6}Sr_{0.4}Ti_{0.1}Fe_{0.9}O_{3-\delta}$ and $La_{0.6}Sr_{0.4}Ti_{0.3}Fe_{0.7}O_{3-\delta}$, respectively, which is roughly the same level of other oxide systems and corresponds reasonably to the transport characteristics and the XRD data in our study. As the Fe substitution increases, the amount of oxygen defect increases and the crystal cell volume expands.

In Table 4-1, the E_{r-xc} and $\sqrt[3]{E_{r-xc}}$ calculated from the Rietveld refinement data in Table 4-2 are compared with the expansion ratio in a reducing atmosphere E_{r-dil} measured by dilatometer. Although it is difficult to compare nanolevel data of the crystal lattice expansion to the microlevel bulk dilatometer data, both results show that E_{r-dil} for the $x = 0.9$ sample is 2-4 times greater than the $x = 0.7$ sample, explaining the effects of both cation substitution and oxygen defects or P_{O_2} .

From these results, it can be considered that a small change in Fe amount the nanolevel crystal structure, strongly corresponds to the stability of the membrane, through a pure chemical substitution effect and the drastic change in lattice parameter at a low P_{O_2} .

This chemical effect, from Ti to Fe ion, can be discussed in detail. The change of the distance between B site metal ion and oxygen in the LSTF samples at air and reduced atmosphere are compared in Table 4-3. The increase of the distance of the B site metal-oxygen for higher Fe substitution seems contradictory to the data of ionic radius of Ti^{+4} (0.068nm) and Fe^{+3} (0.064nm). However, the introduction of oxygen vacancy can promote the repulsion between Fe ions. In reduced atmosphere, oxygen defects increase and then the 3d orbital of metal ion which cannot makes bonding to the oxygen should repulse each other strongly. As Fe ion makes stronger ionic bonding and charge transfer than that of Ti ion, where the electronegativity of Fe and Ti are 1.87 and 1.54 respectively.

Going back to the fracture of the tubes, it is essential to discuss the microstructure of the sintered sample, relating it to the discussion above, and the difference between the nanolevel expansion ratio calculated from unit cell volume and that calculated from a dilatometer. We infer that the behavior of the crystal lattice at the microlevel affects membrane durability in a reducing atmosphere.

Table 4-3. Change of the distance between B site metal ion and oxygen in the LSTF oxide samples at air and reduced atmosphere.

B-O distance at 1000 °C	$La_{0.6}Sr_{0.4}Ti_{0.1}Fe_{0.9}O_{3-\delta}$	$La_{0.6}Sr_{0.4}Ti_{0.3}Fe_{0.7}O_{3-\delta}$
distance in air (Å)	3.9574	3.9485
distance in reduced (Å)	3.9666	3.9531
Elongated rate (%)	0.2325	0.1165

4.4. Conclusion

The thermal expansion behaviors of $\text{La}_{0.6}\text{Sr}_{0.4}\text{Ti}_{1-x}\text{Fe}_x\text{O}_{3-\delta}$, LSTF-7 and LSTF-9 (for $x=0.7$ and 0.9) were investigated by dilatometry and in situ powder X-ray diffractometry up to high temperature under controlled oxygen partial pressures and a reducing atmosphere. The sintered samples of LSTF-7 and LSTF-9 showed a positive thermal expansion, 12.4 and $14.4 \times 10^{-6} \text{ K}^{-1}$, respectively, in air over the whole temperature range, and a larger expansion at low partial oxygen pressures with a linear thermal expansion ratio factor of 0.10 and 0.40% , between $P_{\text{O}_2} = 0.21$ and 1×10^{-20} atm, respectively.

This difference in the expansion rate between two oxide compositions were confirmed again by the analysis of in-situ XRD Rietveld refinement showing that the linear thermal expansion rate estimated from the XRD data for these oxides, 0.13 and 0.27% , respectively.

It is found in this study that the lattice expansion of this LSTF system in reduced atmosphere was not accompanied with any space group but keeping Pnma structure, independent of P_{O_2} , which tell us that this system has lower thermal expansion in principle and a good candidate for robust membrane used in harsh environment.

5. Multilayer ceramic deposition process of dense oxygen permeable membranes on porous supports

5.1. Introduction

An efficient method and related material technologies for forming a dense perovskite-oxide thin film with a relatively high thermal expansion coefficient on a porous support are desired. Researchers are currently exploring the fabrication of porous supports composed of the same material as the membranes, but this approach can give rise to other problems, including porosity deterioration and warping, as the supports undergo burning shrinkage when the membranes are heated to the densification temperature.

In this chapter, we have fabricated a novel membrane system composed of a dense and thin oxygen-ion-conductive layer and a multilayer porous support of the same material, changing the microstructure of each porous layer to control the shrinkage between the layers. We have developed novel durable oxygen-permeable membranes that do not cause any mechanical failure such as peeling, cracking, or deformation in the porous material by controlling the grain size of each porous layer.

5.2. Experimental

5.2.1 Sample preparation

Figure 5-1 shows the flowchart of the preparation of the ceramic membrane in this study. The starting material is an aqueous slurry of an oxide perovskite of a fixed composition of $\text{La}_{0.6}\text{Sr}_{0.4}\text{Ti}_{0.3}\text{Fe}_{0.7}\text{O}_{3-\delta}$ (average particle diameter: 1 μm). The slurry was sprayed and dried to obtain granulated powders with various particle diameters (A: 80 μm , B: 50 μm , C: 30 μm , D: 2 μm) by calcination processes. To predict the densification caused by the firing process, these powders were compacted into pellets (ϕ 25 mm \times t 3 mm) using a compact press of 100 MPa, adding PVA aqueous solution. The pellets were fired at 1400 $^{\circ}\text{C}$ in air for 3 h. We evaluated the average pore size

and porosity of the sintered bodies by the mercury penetration method.

Next, as listed in Table 5-1, we prepared samples with various support structures compacted into 25-mm-diameter pellets by applying a pressure of 100 MPa. We then screen-printed the paste (mixture of terpineol solvent and ethyl cellulose) prepared with powder D onto the top surface of the samples. By varying the viscosity of the paste and the number of screen-printing processes, we controlled the thickness of the printed membrane. The thickness of the membranes after drying ranged from approximately 0.1 to 0.5 mm. We fired these multilayer samples at 1400 °C in air atmosphere for 3h to produce oxygen-permeable membranes. For sample No. 4, this firing temperature was varied from 1300 to 1450 °C.

The thickness of the dense membrane was controlled by adjusting the number of repetitions of the slurry coating process. Powder compacts of (ϕ 25 mm \times t 3 mm) pellets were prepared with powder A and a binder. The pellets were fired at 1400 °C in air for 3h to prepare porous supports. The sintered supports were porous and the average pore diameter and porosity were 10 μ m and 32 %, respectively.

The slurry for coating was prepared with powder D ($\text{La}_{0.6}\text{Sr}_{0.4}\text{Ti}_{0.3}\text{Fe}_{0.7}\text{O}_{3-\delta}$), xylene and a binder. A thick ceramic film was coated onto the porous support by dip coating and drying. The thickness of the film was controlled by the number of repetitions of dipping. Drying was carried out at 80 °C for 30 min, and then, the sample was fired at 1400 °C in air for 3h to prepare oxygen-permeable membranes.

To study the oxygen permeation performance of the samples, the electrode and catalyst were formed on the surface of the dense membrane. Also, an air electrode of $\text{La}_{0.6}\text{Sr}_{0.4}\text{CoO}_3$ was formed at the bottom of the porous support.

A slurry made of mixed powder of NiO and $\text{Ce}_{0.8}\text{Sm}_{0.2}\text{O}_2$ with the mixing ratio of 1:1 by weight was screen-printed on top of the sample and dried. An organometallic solution of LaSrCoO_3 was screen-printed at the bottom of the sample and dried. The sample pellets were fired at 1000 °C for 1h.

Table 5-1 Fabrication of multilayer ceramic membrane.

Sample	Porous support	Dense membrane(D)		
No.	Stacking	Thickness (mm)	*Process	Thickness (mm)
1	A	1	s.p	0.1,0.2 0.3,0.5
2	A+C	2	s.p	
3	A+B	2	s.p	
4	A+B+C	3	s.p	
5	A	3	d	0.2
6	A	3	d	0.1
7	A	3	d	0.07
8	A	3	d	0.05

* s.p=screen printing, d=dip coating

5.2.2. Characterization

The microstructures of the sintered oxygen-permeable membranes and porous supports were investigated using an SEM (JSM6490LA manufactured by JEOL) and a porosity meter (Auto Pore III manufactured by SHIMADZU) by the mercury penetration method. This method of using the high surface tension of mercury causes mercury to fill the pores in the sample. The specific surface area and porosity distribution are then determined from the applied pressure and the amount of infiltrated mercury.

The oxygen permeation test was carried out as chapter 2 at temperatures between 800 and 1000 °C.

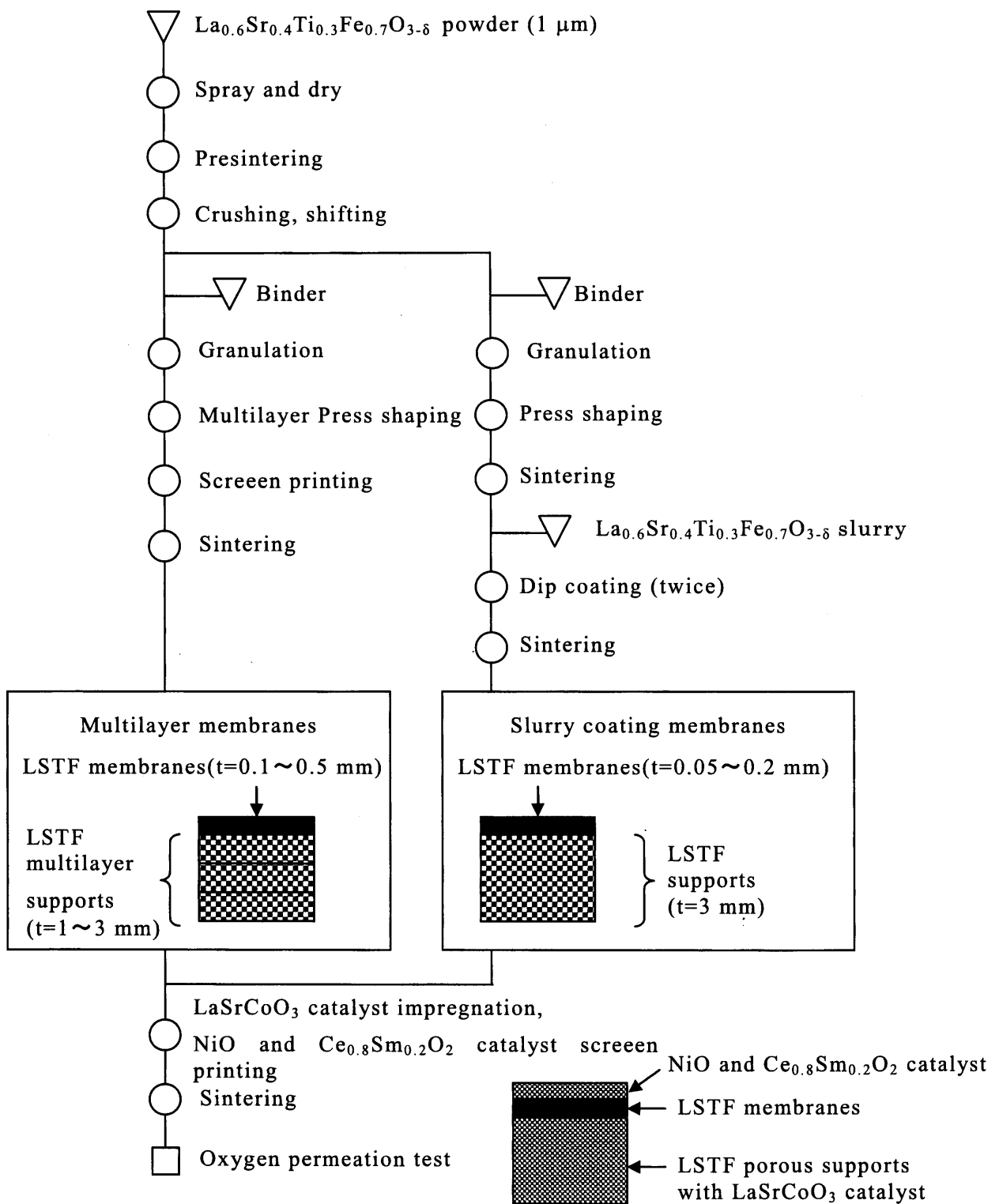


Fig.5-1. Experimental flowchart.

5.3 Results and Discussion

Figure 5-2 shows the SEM images of the raw powders A, B, C, and D and of the sintered bodies after sintering. Dense microstructures could be obtained with the starting powder of smaller particle size. The finest powder D resulted in the highest density in the sintered body. From these results, powder D was chosen for the preparation of dense oxygen-permeable membranes.

After sintering, numerous defects involving peeling at layer boundaries were found in sample No. 1. We attribute these flaws to the stress induced by the large difference in shrinkage rate between the support and the membrane during firing. No peeling occurred in samples No. 2 and 3, but a large deformation resulted, causing many cracks on the surface of the membrane, as shown in the SEM image in Figure 5-3. We suspect that the double-layer structure of the supports of samples No. 2 and 3 reduced the difference in shrinkage rate during firing.

The membranes with the particle-size-graded structure could reduce the stress induced by the different shrinkage behaviors. Sample No. 4 exhibited no peeling or cracking (Figure 5-4). Table 5-2 shows the data of the microstructure of the sintered body in each layer. Table 5-3 shows the frequency of defect formation in the 20 samples prepared. We obtained the best results in sample No. 4, which featured the particle-size-graded structure. On the basis of the results in Tables 5-2 and 5-3, the difference between the shrinkage rates of the membrane and support should be below 10 % to prohibit any unwanted defects.

Figure 5-5 shows SEM images of the surfaces of the sample No. 4 fired at different temperatures from 1300 to 1400 °C. Firing at 1300 °C generated a relatively large number of pores. Firing at 1350 °C and higher resulted in a dense structure. At 1450 °C, grain growth occurred.

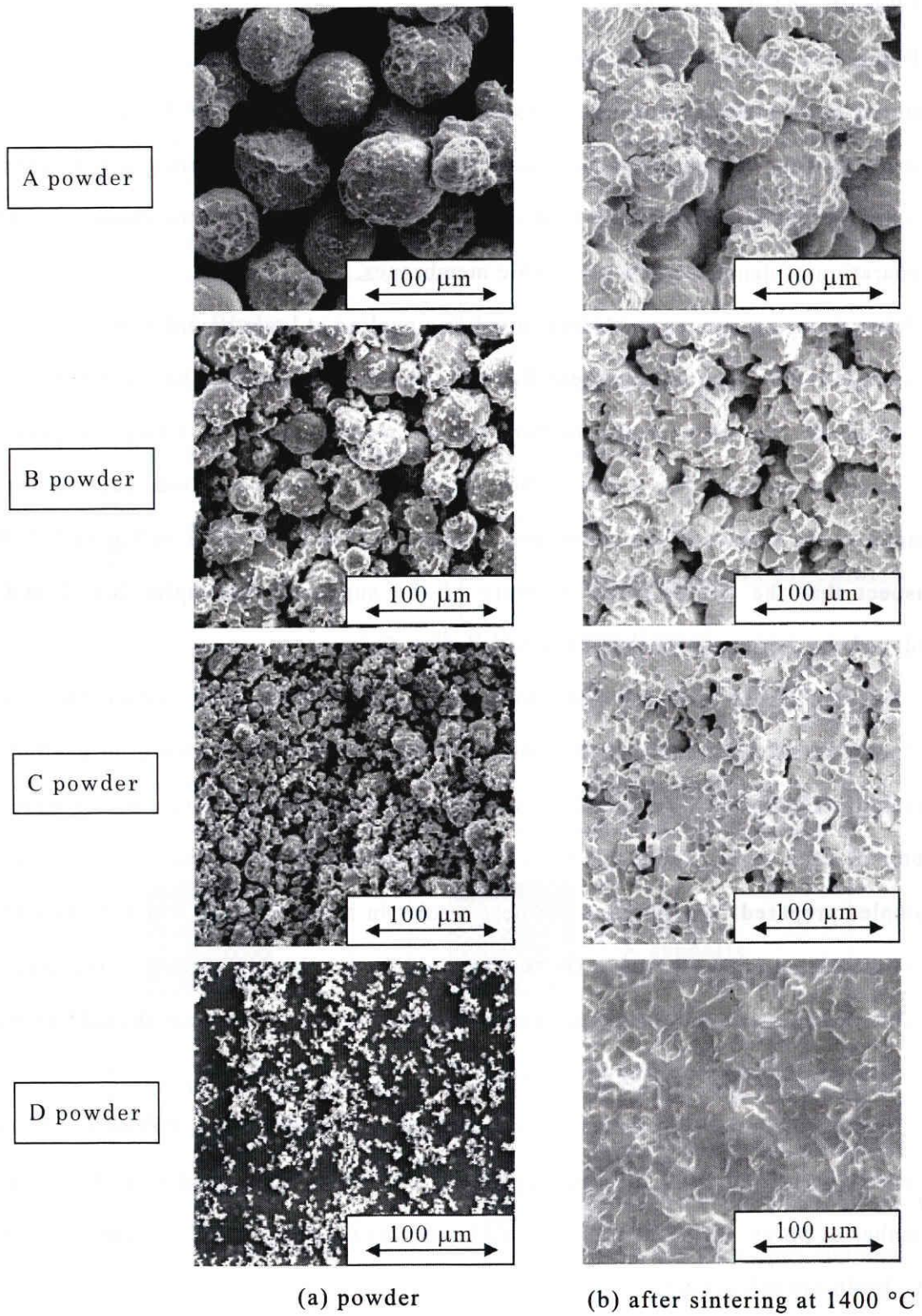


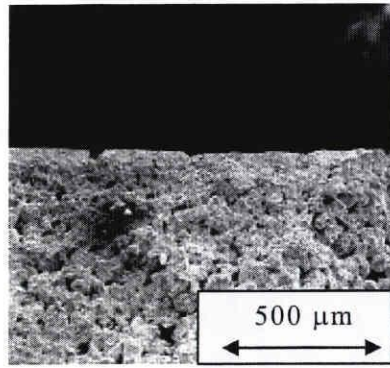
Fig.5-2. SEM image of (a) $\text{La}_{0.6}\text{Sr}_{0.4}\text{Ti}_{0.3}\text{Fe}_{0.7}\text{O}_{3-\delta}$ powder and (b)after sintering.

Table 5-2 Data of the microstructure of the sintered body in each layer.

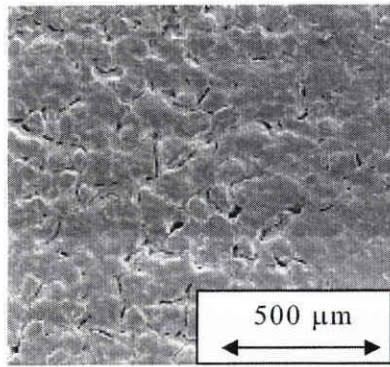
Starting powder/ Average grain diameter of starting powder (μm)	1400 °C sintered average pore diameter (μm)	1400 °C sintered porosity (%)	1400 °C sintered shrinkage (%)
A / 80	10	32	7
B / 50	5.8	17	10
C / 30	1.5	5	15
D / ≤ 10	≤ 0.5	≤ 2	20

Table 5-3 Frequency of defect in the 20 samples prepared.

Sample No.	1	2	3	4	5	6	7	8
Frequency of peeling and cracking	90 %	20 %	30 %	0 %	90 %	70 %	40 %	30 %
Frequency of bending for supports	5 %	20 %	10 %	5 %	30 %	10 %	10 %	10 %

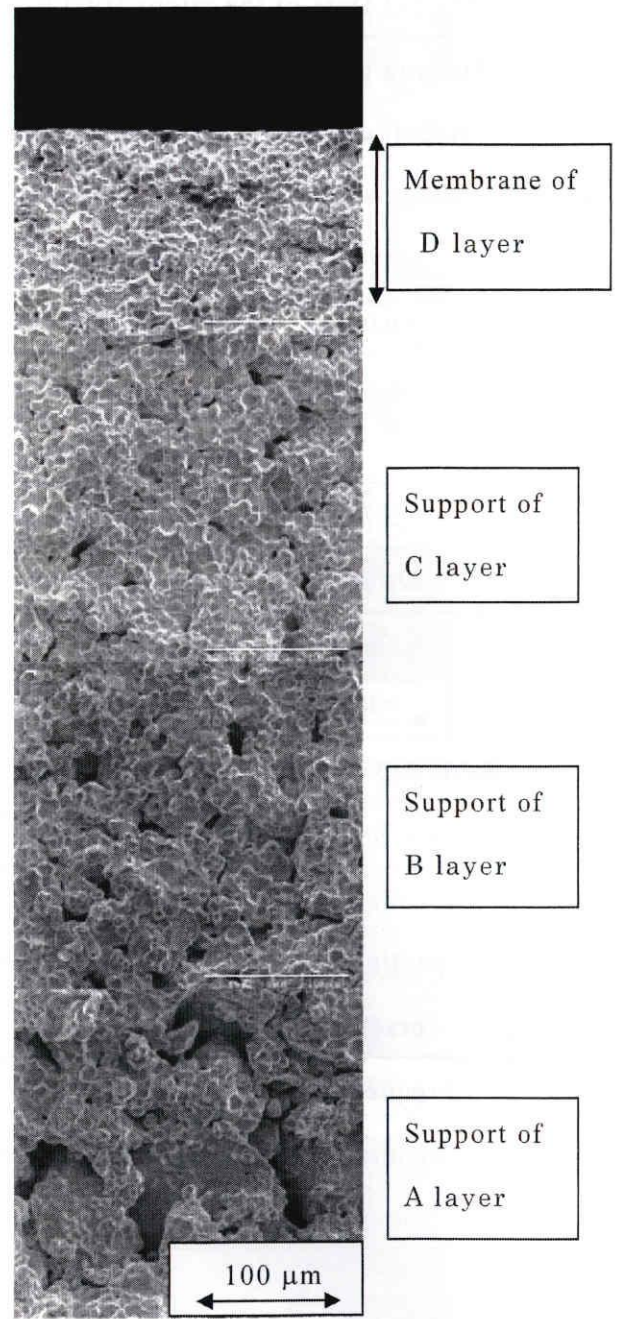


Cross section



Membrane surface

Fig.5-3. SEM image of $\text{La}_{0.6}\text{Sr}_{0.4}\text{Ti}_{0.3}\text{Fe}_{0.7}\text{O}_{3-\delta}$ membrane 2 sintering at 1400 °C.



Membrane of D layer

Support of C layer

Support of B layer

Support of A layer

Fig.5-4. Cross section SEM image of $\text{La}_{0.6}\text{Sr}_{0.4}\text{Ti}_{0.3}\text{Fe}_{0.7}\text{O}_{3-\delta}$ membrane 4 sintering at 1400 °C.

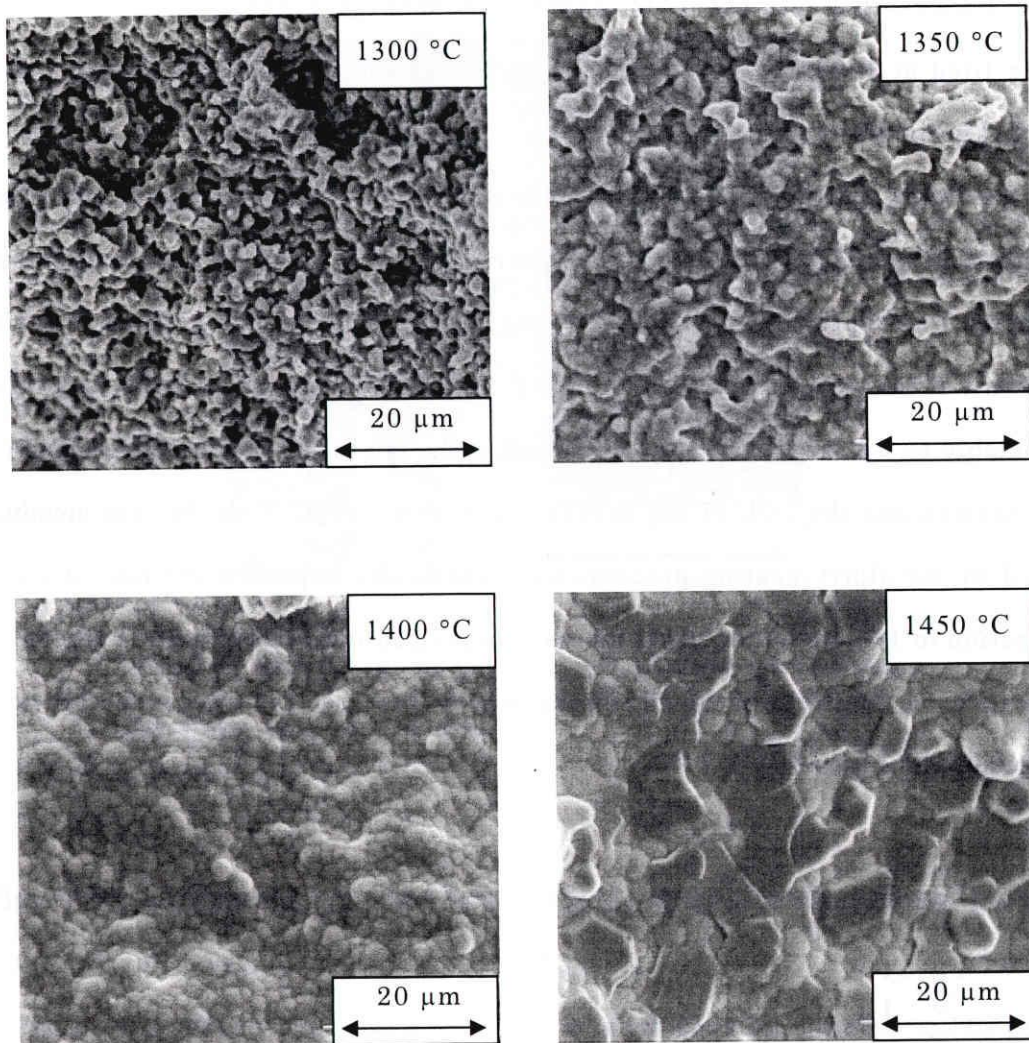


Fig.5-5. SEM image of $\text{La}_{0.6}\text{Sr}_{0.4}\text{Ti}_{0.3}\text{Fe}_{0.7}\text{O}_{3-\delta}$ membrane 4 sintering at 1300~1450 °C.

Figure 5-6 shows the oxygen permeation of the membranes of No. 4 sintered at different temperatures, investigated under methane reforming conditions. The sample fired at 1300 °C exhibited a low density and appreciable nitrogen leakage, and its rate of oxygen permeation was low. The dense sample fired at 1400 °C showed a high rate of oxygen permeation: 12 cc/min/cm². For the sample fired at 1450 °C, the rate of nitrogen leak was about the same as that of the sample fired at 1400 °C, but its

oxygen permeability was lower. We hypothesize that the oxygen permeability of the sample fired at 1400 °C is degraded by decreased ion conductivity in areas where sectional grain growth occurred.

By the slurry coating process, a very thin and dense membrane with a thickness of 50 μm was prepared (Figure 5-7). As shown in Table 5-3, a thinner oxygen-permeable membrane was confirmed to exhibit a lower frequency of defects generation such as membrane cracking, peeling, and warping of the support. We believe that this is attributable to the large shrinkage observed in the lateral direction of the membrane cross section and the lack of any mitigation of this stress. With the thin membrane formed by the slurry coating process, we successfully improved the rate of oxygen permeation to 18 $\text{cc}/\text{min}/\text{cm}^2$. This increase in permeation performance is attributable to the reduced thickness of the membrane, which increased the ion conduction across the membrane thickness.

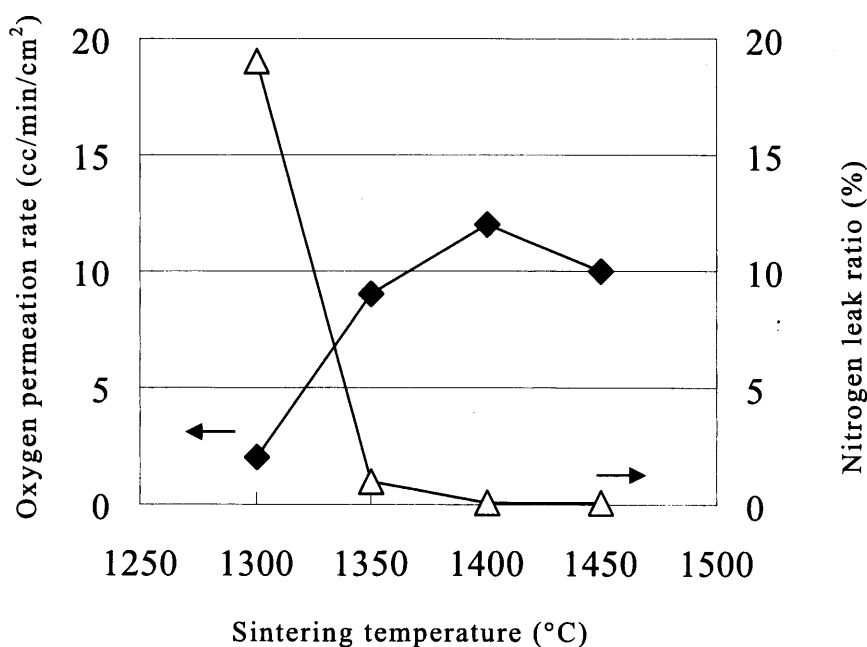


Fig.5-6. Temperature dependence of oxygen permeation rates and nitrogen leak ratio for $\text{La}_{0.6}\text{Sr}_{0.4}\text{Ti}_{0.3}\text{Fe}_{0.7}\text{O}_{3-\delta}$ membrane 4. ($\text{CH}_4/\text{Membranes}/\text{Air } 1000 \text{ }^\circ\text{C}$)

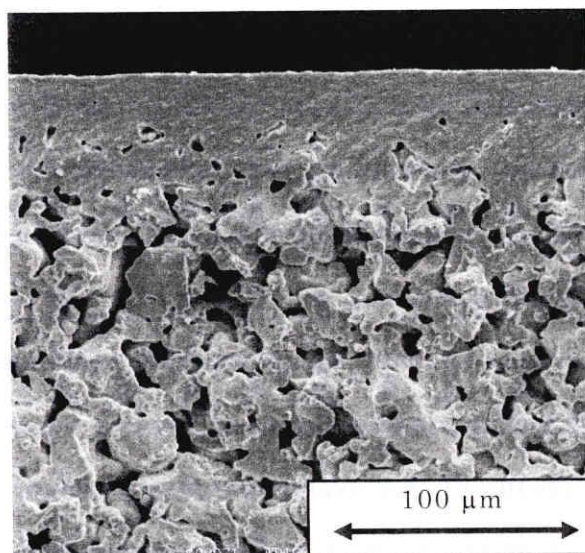


Fig.5-7. SEM image of $\text{La}_{0.6}\text{Sr}_{0.4}\text{Ti}_{0.3}\text{Fe}_{0.7}\text{O}_{3-\delta}$ membranes by slurry coating process.

Figure 5-8 indicates the relationship between the reciprocal of membrane thickness and the rate of oxygen permeation of the $\text{La}_{0.6}\text{Sr}_{0.4}\text{Ti}_{0.3}\text{Fe}_{0.7}\text{O}_{3-\delta}$ oxygen-permeable membranes prepared by the screen printing and slurry coating processes. The rate of oxygen permeation increased proportionally to the reciprocal of membrane thickness, but the gradient declined in thin-membrane regions. The deviation from the theoretical value derived from equation (1) was greater in thin-membrane regions. In other words, other factor than the conductivity of ions in the membrane seems to cause limiting effects. One reason is insufficient catalyst activity due to inadequately supported catalyst particles in the support near the membrane. In short, an increase in the amount of permeated oxygen appears to have functioned as a limiting factor in surface reactions between the membrane and the catalyst boundary surface. Another possible cause is the factor that limits gas diffusion within the support.

Comparing the multilayer and slurry coating processes, we determined that membranes formed by the slurry coating process, which enables the creation of

thinner membranes, provide a higher oxygen permeability. However, when the membrane and support are made of the same material, as in our experiments, the frequency of defects generated by shrinkage resulting from firing was significantly low. For future industrial applications, we recommend the combination two processes: the formation of a membrane by the slurry coating process on a support prepared by the multilayer process.

We performed an evaluation with water vapor and helium gas/membrane/air (membrane thickness: 0.5 mm) to assess the durability in a water-related application. Figure 5-9 shows the results of this evaluation. Oxygen permeability remained at 97 % or above after eight hours under temperatures of 800, 900, and 1000 °C, indicating an adequate basic durability in steam-related processes.

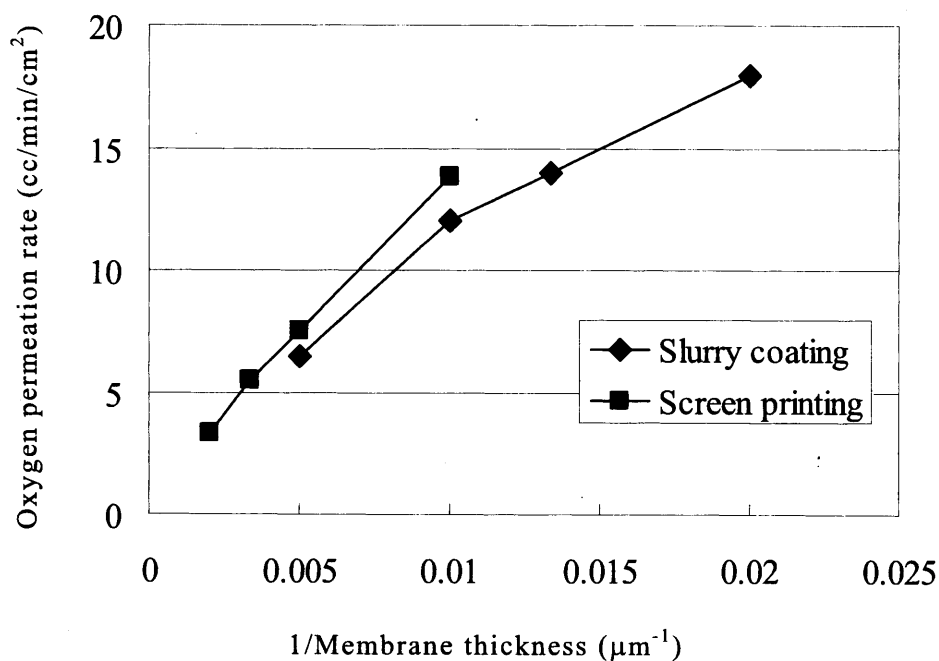


Fig.5-8. Relationship between the reciprocal of membrane thickness and oxygen permeation rates for $\text{La}_{0.6}\text{Sr}_{0.4}\text{Ti}_{0.3}\text{Fe}_{0.7}\text{O}_{3-\delta}$ oxygen membranes prepared by the screen printing process and slurry coating process. ($\text{CH}_4/\text{Membranes}/\text{Air}$ 1000°C)

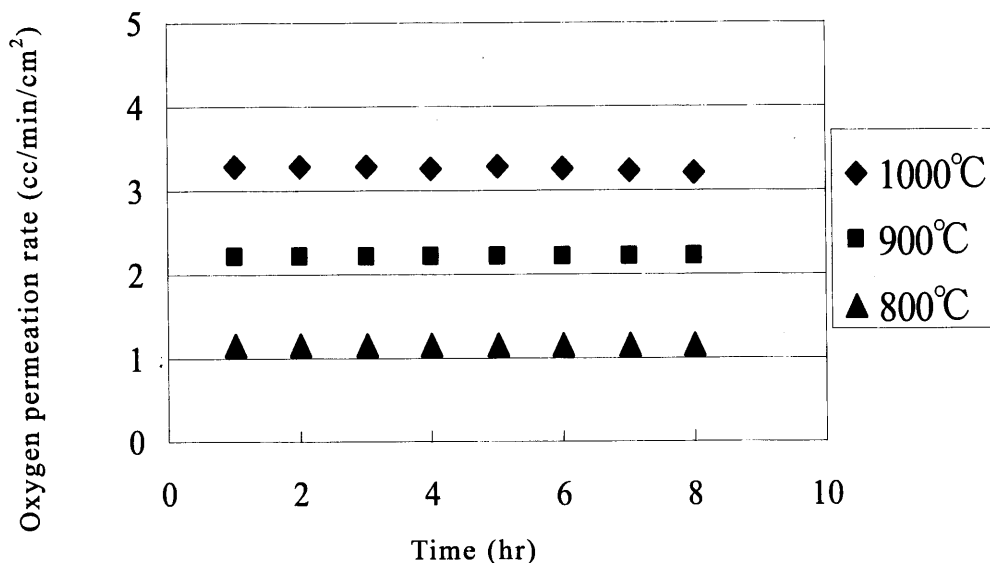


Fig.5-9. Time course of oxygen permeation rates for $\text{La}_{0.6}\text{Sr}_{0.4}\text{Ti}_{0.3}\text{Fe}_{0.7}\text{O}_{3-8}$ membranes at various temperature. (He+Steam/Membranes/Air)

5.4. Conclusion

A multilayer ceramic deposition process of $\text{La}_{0.6}\text{Sr}_{0.4}\text{Ti}_{0.3}\text{Fe}_{0.7}\text{O}_{3-8}$ (LSTF) was developed for the fabrication of durable oxygen-permeable membranes. By optimizing the diameter of the starting powder and sintering temperature, defects such as peeling and cracking in the ceramic multilayer could be eliminated. The diameter of the starting powder particles for the membrane and the sintering temperature were 2 μm and 1400 °C, respectively. The difference between the shrinkage rates of the membrane and the support should be below 10 %. With this optimized process condition, we fabricated a thin LSTF membrane formed by the slurry coating process on porous support LSTF and found its rate of oxygen permeation to be 18 cc/min/cm².

6. Oxygen ion conducting membranes sintered under different atmosphere and HIP

6.1. Introduction

We have found the effect of the substitution of Fe for Al in reducing the expansion at reducing atmosphere ⁴⁴⁾, but the sintering of perovskite with Al is generally difficult to make high density sample. As the low-density membrane easily leaks gas and also show low stability for cyclic stress. High temperature sintering over 1500 °C is required to obtain high density. However, high temperature process can reduce the porosity of support (ex. perovskite, zirconia, magnesia) materials, and other process solution is necessary.

In this chapter, we have researched the effect of sintering atmosphere by preparing the $\text{La}_{0.6}\text{Sr}_{0.4}\text{Al}_{0.1}\text{Fe}_{0.9}\text{O}_{3-\delta}$ membranes under various gas atmospheres in order to obtain membranes with high density at low sintering temperatures. The influence of high sintering pressure under hot isostatic pressing (HIP) has also been examined.

6.2. Experimental

6.2.1. Preparation of $\text{La}_{0.6}\text{Sr}_{0.4}\text{Al}_{0.1}\text{Fe}_{0.9}\text{O}_{3-\delta}$ (LSAF) membrane

Powders of La_2O_3 (Wako Pure Chemical Industries, Ltd., grain size 1 μm), SrCO_3 (Wako, grain size 1 μm), Al_2O_3 (Wako, grain size 1 μm), and Fe_2O_3 (Wako, grain size 1 μm) were mixed to prepare composition of $\text{La}_{0.6}\text{Sr}_{0.4}\text{Al}_{0.1}\text{Fe}_{0.9}\text{O}_{3-\delta}$. The powders were mixed using a ball mill with YSZ balls with a milling time of 5 h, and then calcined at 1000°C for 6h. The calcined powder was mixed with a PVA aqueous solution binder and then compacted into a tube (outside diameter $\Phi 20\text{mm}$ ×inside diameter $\Phi 10\text{mm}$ ×L100mm) using at a cold isostatic pressure of 150 MPa. One end of the tube was closed and the other end was open, as shown in Figure 2-2. These tube compacts were fired at 1500 °C for 3h in various atmospheres (Air, O_2 , Ar, mixed gas of N_2+O_2 , purity>99% each other). The oxygen partial pressure, P_{O_2} , was

monitored by oxygen sensor during the sintering. After the sintering in air at 1500 °C, the samples were HIP(KOBELCO SYSTEM20) treated at O₂ 20% + Ar 80%, 150MPa at 1500 °C for 1h with no capsule.

The thickness of the tubes was reduced into 0.5mm by grounding the surface of the tube for the test of oxygen permeation. The catalytic electrode was formed on the surface of the tube of membrane samples, as shown in Figure 2-2. The NiO-Ce_{0.8}Sm_{0.2}O₂ was selected for catalytic electrode material because of the ionic conductance of Ce_{0.8}Sm_{0.2}O₂ and high catalytic activity of NiO³¹⁾. An air electrode of La_{0.5}Sr_{0.5}CoO₃, one of the most promising cathode materials³²⁾, was dip-coated on the other surface of the tube and dried. A slurry of powder mixture, NiO and Ce_{0.8}Sm_{0.2}O₂ electrode catalyst mixed in a 1:1 weight ratio, was dip-coated on the fuel side of the sample and dried. To sinter these catalytic electrodes, the tube was fired again at 1000°C for 1h.

6.2.2. Characterization

We have evaluated the relative density, three point flexural strength, difference between expansion ratios in reducing and air atmospheres and oxygen permeation of the La_{0.6}Sr_{0.4}Al_{0.1}Fe_{0.9}O_{3-δ} samples.

The relative densities of the samples were measured by Archimedes method (METTLER AT-201). The test sample for three point flexural strength test was cut from La_{0.6}Sr_{0.4}Al_{0.1}Fe_{0.9}O_{3-δ} membrane tube and machined into a bar of 3mm×4mm×40mm dimension. The three point flexural strength of La_{0.6}Sr_{0.4}Al_{0.1}Fe_{0.9}O_{3-δ} was obtained by averaging ten trial data measured by INSTRON 5500R (JIS R1601, R1604) at 25 °C and 1000 °C.

The thermal expansion for the sintered samples (cut from tube membrane and machined into a rod of Φ2mm×L15mm), La_{0.6}Sr_{0.4}Al_{0.1}Fe_{0.9}O_{3-δ}, have been measured at reducing atmosphere (4% hydrogen and 96 vol.% nitrogen) ($\Delta L/L_{red}$) as well as in air ($\Delta L/L_{air}$), in the temperature range between 25 °C and 1000 °C using Rigaku

TMA8310 dilatometer. The difference between the values measured at the two atmospheres is expressed as a differential expansion ratio, E_{r-dil} ,

$$E_{r-dil} (\%) = (\text{difference between expansion ratios in reducing and air atmospheres}) \\ = (\Delta L/L_{red} - \Delta L/L_{air}) / (1 + \Delta L/L_{air}) \times 100.$$

The tube samples coated by catalytic electrodes were used for the oxygen permeation performance test, as shown in Figure 2-2, at temperatures from 800 to 1000°C. (Details of experiment: Chapter 2)

6.3. Results and Discussion

Figure 6-1 shows the SEM images of the microstructure of $La_{0.6}Sr_{0.4}Al_xFe_{1-x}O_3$ ($x=0.1-0.3$) samples sintered at 1500 and 1600 °C in air. All the samples show the closed pore and the pore channels. At the sintering temperature of 1500 °C, it was difficult to densify the samples especially samples with higher Al content. Higher sintering temperature was necessary to densify such samples. By increasing the sintering temperature to 1600 °C, the densifications of all the samples were achieved and most of the pores except the closed pores could be removed as shown in Fig. 6-1(b).

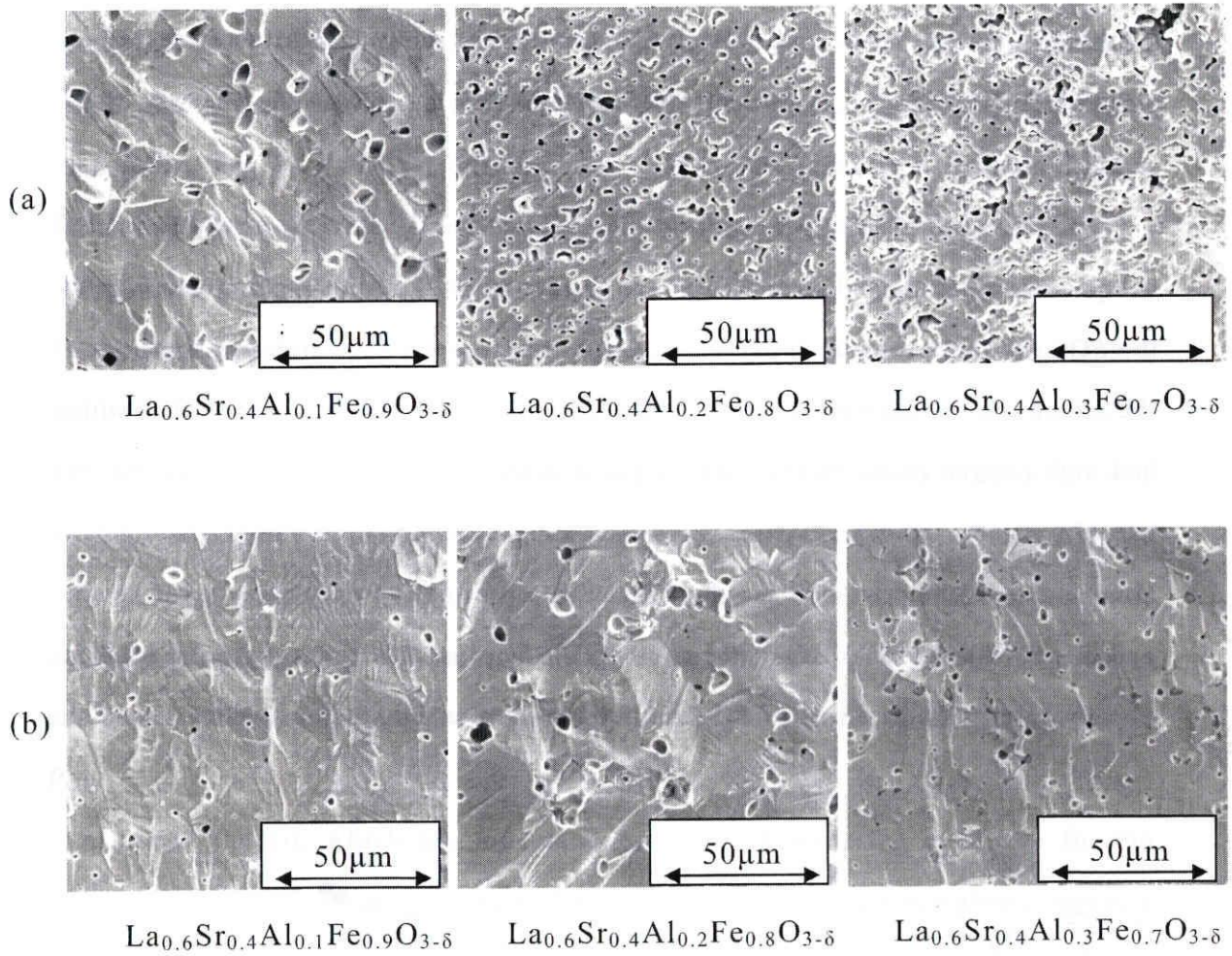


Fig.6-1.SEM images of $\text{La}_{0.6}\text{Sr}_{0.4}\text{Al}_x\text{Fe}_{1-x}\text{O}_3$ ($x=0.1-0.3$) samples sintered at (a) 1500 °C and (b) 1600 °C in air at 0.1MPa.

The composition of $\text{La}_{0.6}\text{Sr}_{0.4}\text{Al}_{0.1}\text{Fe}_{0.9}\text{O}_{3-\delta}$, which has the lowest Al content in this study, was selected for further investigation, because of its densification property at the lower sintering temperature. High temperature sintering over 1500 °C could be a problem in the microstructure control of other materials, such as the porosity of the support.

Figure 6-2 shows the relationship of the apparent densities of the samples sintered at various oxygen partial pressures, PO_2 . The density of LSAF sample increased with the PO_2 , up to the maximum of 98.2%. Chan et al. reported the sintering behavior of the mixed ion conducting oxides of $\text{SrCo}_{0.4}\text{Fe}_{0.5}\text{Zr}_{0.1}\text{O}_{3-\delta}$ sintered at high PO_2 which had high oxygen permeability without gas leakage ⁴⁵). They have suggested that the use of oxygen partial pressures higher than atmospheric oxygen mol fraction during sintering could help to increase the concentration of cation vacancies in the sample and hence the cation diffusion rate thereby helping the sintering process. It is expected that similar effect of PO_2 occurred in the present study as well.

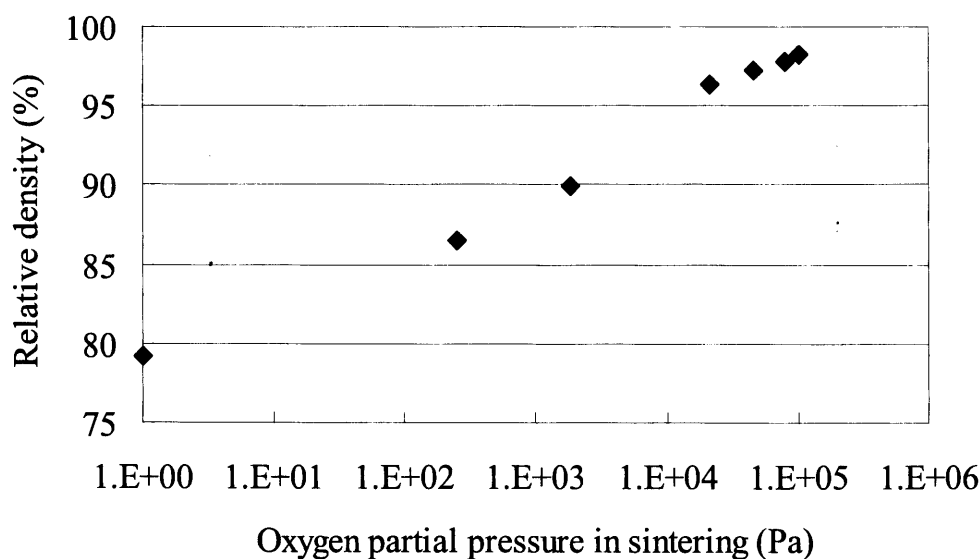


Fig.6-2. The influence of PO_2 on sintered relative density of $\text{La}_{0.6}\text{Sr}_{0.4}\text{Al}_{0.1}\text{Fe}_{0.9}\text{O}_{3-\delta}$ membranes.

Figure 6-3 shows the XRD patterns of $\text{La}_{0.6}\text{Sr}_{0.4}\text{Al}_{0.1}\text{Fe}_{0.9}\text{O}_{3-\delta}$ (LSAF) samples sintered at 1500 °C, under different sintering atmospheres. Both $\text{La}_{0.6}\text{Sr}_{0.4}\text{Al}_{0.1}\text{Fe}_{0.9}\text{O}_{3-\delta}$ samples sintered in Air and O_2 were confirmed as perovskite single phase, orthorhombic structures. However the LSAF sample sintered in Ar atmosphere, low P_{O_2} , was partially reduced to form intermetallic compounds, AlFe, AlFe_3 , and Al_3Fe . Therefore this sample could not be sintered to high density.

Figure 6-4 compares the SEM images of the microstructure of the LSAF samples sintered under various gas atmospheres. Most of the pores in the samples are closed and porosity decreased with the oxygen partial pressure during the sintering, P_{O_2} . In the very low P_{O_2} atmosphere, the oxide decomposed into the intermetallic phase and the microstructure became porous. In the atmosphere of moderate P_{O_2} , air, the sample showed large grain growth. This grain growth is due to the fast material transport, not only the oxygen ion but also the metal cation. This ambipolar diffusion process can be activated at relatively low P_{O_2} but limited by the criteria of the decomposition P_{O_2} .

Although the air, which has moderate P_{O_2} , is good sintering condition for the LSAF samples, it is not easy to eliminate the closed pores in atmospheric pressure condition. We have carried out a post sintering HIP for LSAF samples sintered in air atmosphere at 1500 °C to make a pore-free membrane sample.

The HIP treated LSAF membrane showed remarkably high density, 99.6%, and the amount of pores in the HIP treated samples was significantly reduced as shown in Figure 6-4. There was no change in the grain size of atmosphere sintered and HIP treated samples, but the pores of several μm at grain corner eliminated by the HIP treatment, as shown in the cross section images of these two membranes.

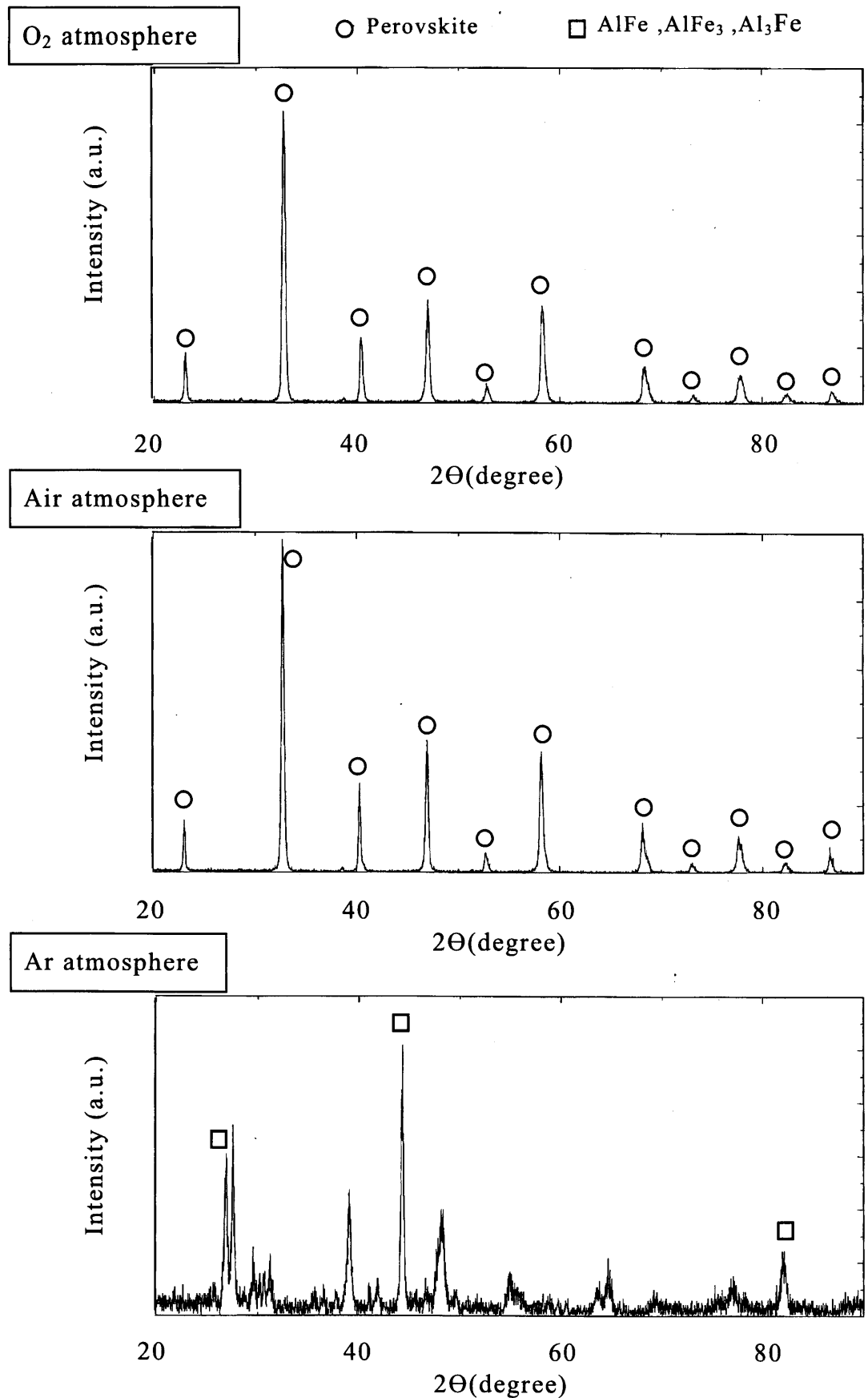


Fig.6-3. XRD patterns of $\text{La}_{0.6}\text{Sr}_{0.4}\text{Al}_{0.1}\text{Fe}_{0.9}\text{O}_{3-\delta}$ after sintering at 1500 °C.

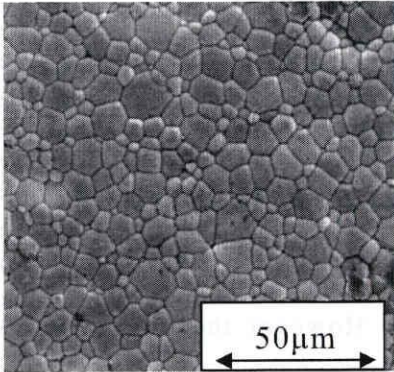
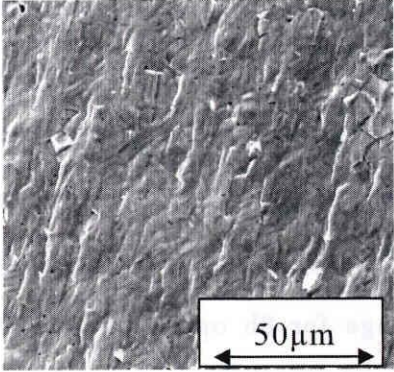
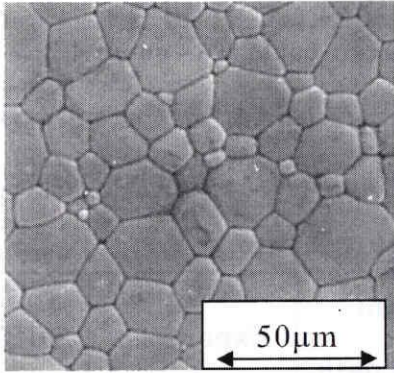
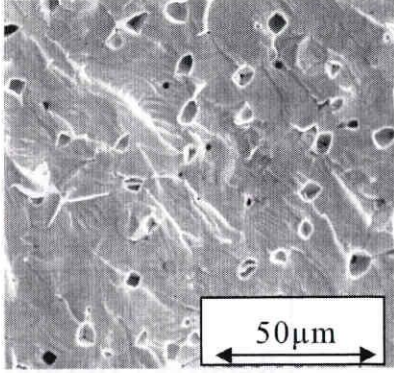
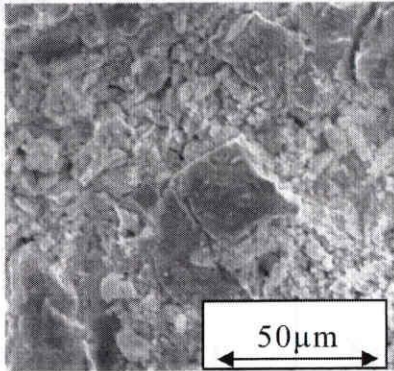
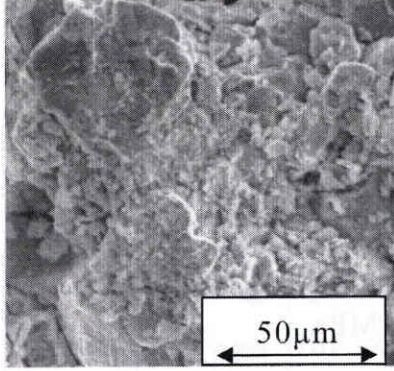
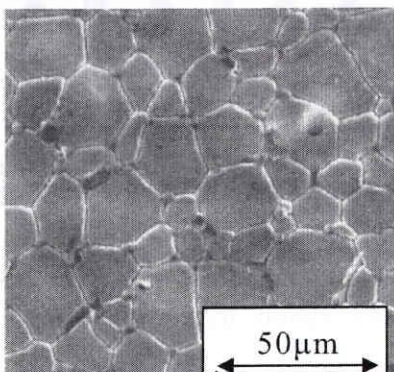
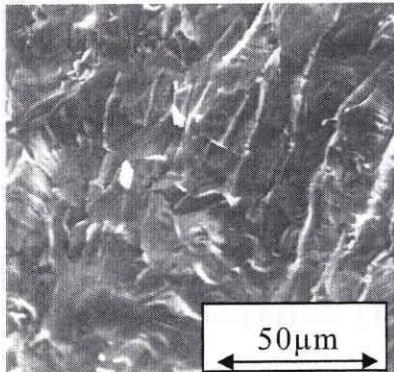
Atmosphere in sintering	Surface of membrane	Cross section of membrane
O ₂ 0.1MPa		
Air (20% O ₂) 0.1MPa		
Ar 0.1MPa		
Air (20% O ₂) 0.1MPa + O ₂ 20% Ar 80% (HIP 150MPa)		

Fig.6-4. SEM images of the $\text{La}_{0.6}\text{Sr}_{0.4}\text{Al}_{0.1}\text{Fe}_{0.9}\text{O}_{3-\delta}$ membranes sintered under different gas atmospheres.

As shown in Table 6-1 and Figure 6-5, the three point flexural strength of $\text{La}_{0.6}\text{Sr}_{0.4}\text{Al}_{0.1}\text{Fe}_{0.9}\text{O}_{3-\delta}$ was higher at high oxygen atmosphere and high pressure in sintering. Particularly the flexural strength at 1000 °C of HIP treated membrane was 1.26 times as high as the membranes sintered in air. These contribute to stability for reducing atmosphere as shown in Figure 6-6. The HIP membrane with the thickness of 0.5 mm showed the high oxygen permeation rate of 8 cc/min/cm² and no gas leakage for 8h operation at 1000°C. However the oxygen permeation rate of the sintered membrane in normal atmosphere, in O₂, decreased with the increase of gas leakage, and the membrane sintered in air could not endure 4 h.

Table 6-1. Property of the $\text{La}_{0.6}\text{Sr}_{0.4}\text{Al}_{0.1}\text{Fe}_{0.9}\text{O}_{3-\delta}$ samples sintered under various gas atmospheres.

Sintering atmosphere	Relative density (%)	Three point flexural strength (MPa)		Expansion coefficient ($\times 10^{-6}/\text{K}^{-1}$, 25-1000°C)	Differential expansion ratio Er-dil (%)	O ₂ permeation (cc/min/cm ² /N ₂ leak ratio at 4h)
		25 °C	1000 °C			
O ₂ 0.1MPa	98.2	241	187	15.6	0.37	5.7 / 5.8
Air 0.1MPa	96.5	231	165	15.6	0.37	1.2 / 18
Ar 0.1MPa	79.2	55	38	-	-	-
Air 0.1MPa + HIP	99.6	265	208	15.6	0.37	8.6 / 0.5

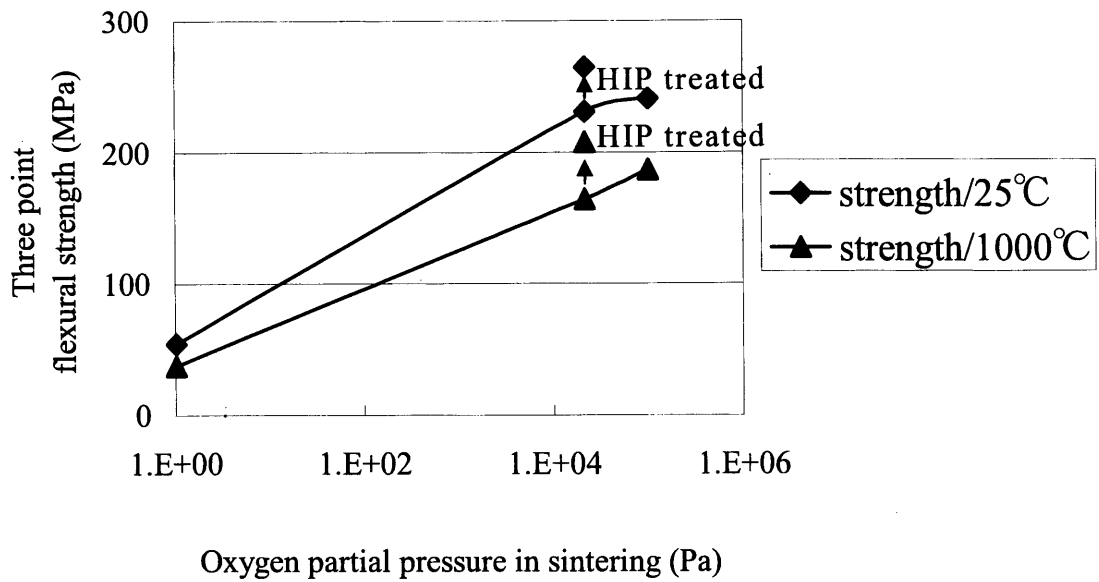


Fig.6-5. The influence of PO_2 of the sintering process on three point flexural strength of sintered $La_{0.6}Sr_{0.4}Al_{0.1}Fe_{0.9}O_{3-\delta}$ membranes.

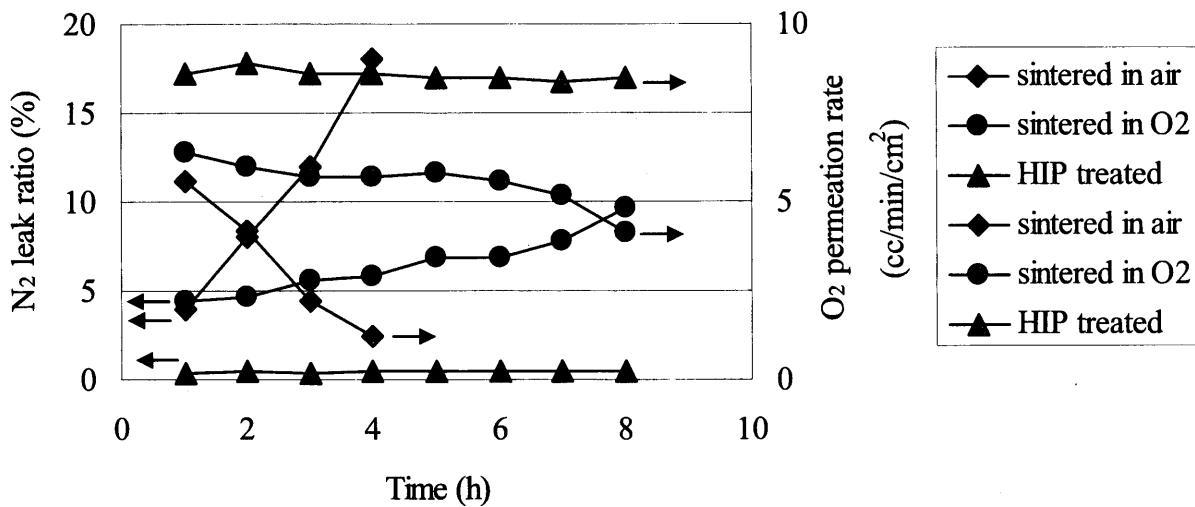


Fig.6-6. Change of the nitrogen leak ratio (percentage of nitrogen permeation rate to that of oxygen) and the oxygen permeation rates of membranes (thickness = 0.5mm) prepared under various sintering atmospheres. (The leakage and oxygen permeation rate were measured at 1000°C)

Figure 6-7 compares the results of thermal expansion of two sintered samples, one is sintered at normal pressure in air and the other is HIP treated. For both samples, the thermal expansion coefficients and the differential expansion ratios in air and reducing atmosphere, Er-dil were the same, $15.6 \times 10^{-6}/K-1$ and 0.37%, respectively (see Table 1). Their thermal expansion behaviors changed drastically in reducing atmosphere over the temperature 800°C.

From these results, it is considered that the stability problems mainly depends the microstructure and pores which is greatly enhanced by the post treatment of the HIP.

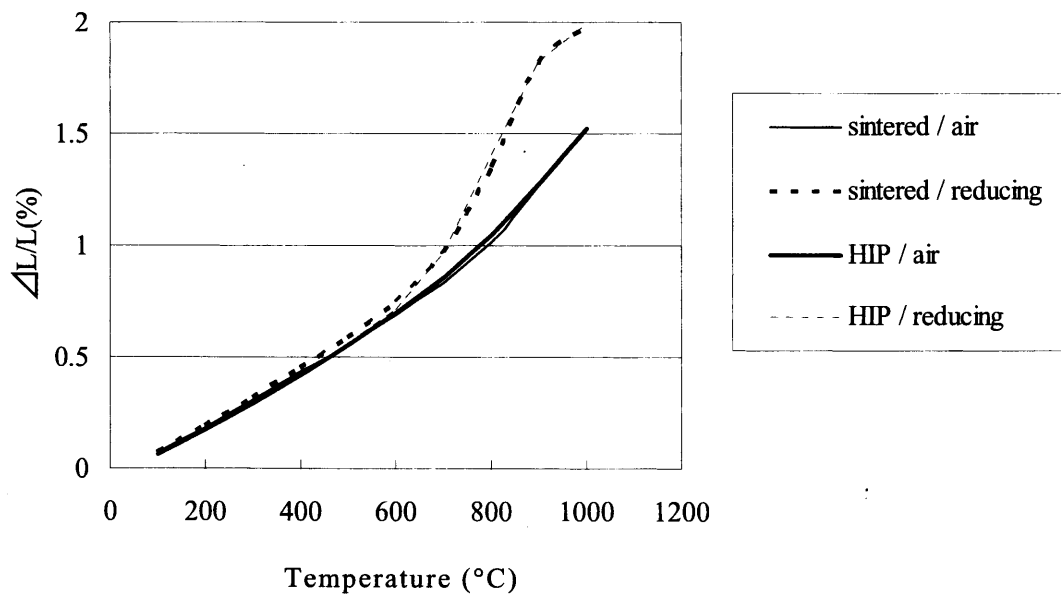


Fig.6-7. The thermal expansion curves of $La_{0.6}Sr_{0.4}Al_{0.1}Fe_{0.9}O_{3-\delta}$ materials sintered/HIP treated in air or in a reducing atmosphere.

6.4. Conclusion

$\text{La}_{0.6}\text{Sr}_{0.4}\text{Al}_x\text{Fe}_{1-x}\text{O}_{3-\delta}$ (LSAF) mixed ionic electronic conducting membranes have been sintered under various gas atmospheres. The substitution of Al for Fe reduced the density of the LSAF samples sintered at 1500 °C, creating large pore channels, but the sintering at 1600 °C achieved high density samples. The densifications of the $\text{La}_{0.6}\text{Sr}_{0.4}\text{Al}_{0.1}\text{Fe}_{0.9}\text{O}_{3-\delta}$ samples at 1500 °C have been promoted with the P_{O_2} and the oxide sample was decomposed in Ar atmosphere. The thermal expansion coefficient and differential expansion ratio in air and reducing atmosphere of the $\text{La}_{0.6}\text{Sr}_{0.4}\text{Al}_{0.1}\text{Fe}_{0.9}\text{O}_{3-\delta}$ samples were $15.6 \times 10^{-6}/\text{K}^{-1}$ and 0.37%, respectively, were not influenced by the sintering process. The HIP treated membranes exhibited high density of 99.6%, and three point flexural strength, 265MPa and 208MPa at 25°C and 1000 °C, respectively. The HIP membrane with the thickness of 0.5 mm showed the oxygen permeation rate of 8 cc/min/cm².

7. Rheological study of $\text{LaSrTiFeO}_{3-\delta}$ paste for screen printing process

7.1. Introduction

In this Chapter, $\text{La}_{0.6}\text{Sr}_{0.4}\text{Ti}_{0.3}\text{Fe}_{0.7}\text{O}_{3-\delta}$ paste consisting of a binder system of ethylcellulosous copolymer and organic solvent of terpineol and BDGAC (butyl diglycol acetate) for screen printing process were prepared, and the rheological behavior of the pastes with different powder content of $\text{La}_{0.6}\text{Sr}_{0.4}\text{Ti}_{0.3}\text{Fe}_{0.7}\text{O}_{3-\delta}$ and the different molecular weight of ethylcellulosous were analyzed by dynamic viscoelasticity method.

7.2. Experimental

7.2.1. Preparation of $\text{La}_{0.6}\text{Sr}_{0.4}\text{Ti}_{0.3}\text{Fe}_{0.7}\text{O}_{3-\delta}$ (LSTF) paste

Powders of La_2O_3 (Wako Pure Chemical Industries, Ltd., grain size 1 μm), SrCO_3 (Wako, grain size 1 μm), TiO_2 (Wako, grain size 1 μm), and Fe_2O_3 (Wako, grain size 1 μm) were mixed to prepare composition of $\text{La}_{0.6}\text{Sr}_{0.4}\text{Ti}_{0.3}\text{Fe}_{0.7}\text{O}_{3-\delta}$. The powders were mixed using a ball mill with YSZ balls for 5 h, and then calcined at 1400°C for 6h. After calcinations, sintered sample was milled by ball milling and the $\text{La}_{0.6}\text{Sr}_{0.4}\text{Ti}_{0.3}\text{Fe}_{0.7}\text{O}_{3-\delta}$ powder with the average diameter of 1 μm was obtained.

The vehicle system of EC (ethylcellulosous) and organic solvent of terpineol and BDGAC (butyl diglycol acetate) were prepared by mixing in hot stirrer at 80°C for 2h. The vehicle and the $\text{La}_{0.6}\text{Sr}_{0.4}\text{Ti}_{0.3}\text{Fe}_{0.7}\text{O}_{3-\delta}$ powder from 60 wt% to 80 vol%(from 28 vol% to 51 vol%) were mixed by a roll-mill at 25 °C for 30min. The various condition pastes of $\text{La}_{0.6}\text{Sr}_{0.4}\text{Ti}_{0.3}\text{Fe}_{0.7}\text{O}_{3-\delta}$ as listed at Table 1 were prepared.

Table 7-1. Samples of LSTF paste.

samples	solvent	EC Mw	EC (wt%)	Powder content (wt%)
TE0 - 60 - 70	Terpineol	-	0	60,70,80
TE4- 1 - 60 - 70		44000	1	
TE4- 5 - 60 - 70			5	
TE4- 10 - 60 - 70			10	
TE4- 15 - 60 - 70			15	
TE100- 1 - 60 - 70		180000	1	
TE100- 5 - 60 - 70			5	
TE100- 10 - 60 - 70			10	
TE100- 15 - 60 - 70			15	
BE0 - 60 - 70		BDGAC	-	
BE4- 1 - 60 - 70	44000		1	
BE4- 5 - 60 - 70			5	
BE4- 10 - 60 - 70			10	
BE4- 15 - 60 - 70			15	
BE100- 1 - 60 - 70	180000		1	
BE100- 5 - 60 - 70			5	
BE100- 10 - 60 - 70			10	
BE100- 15 - 60 - 70			15	

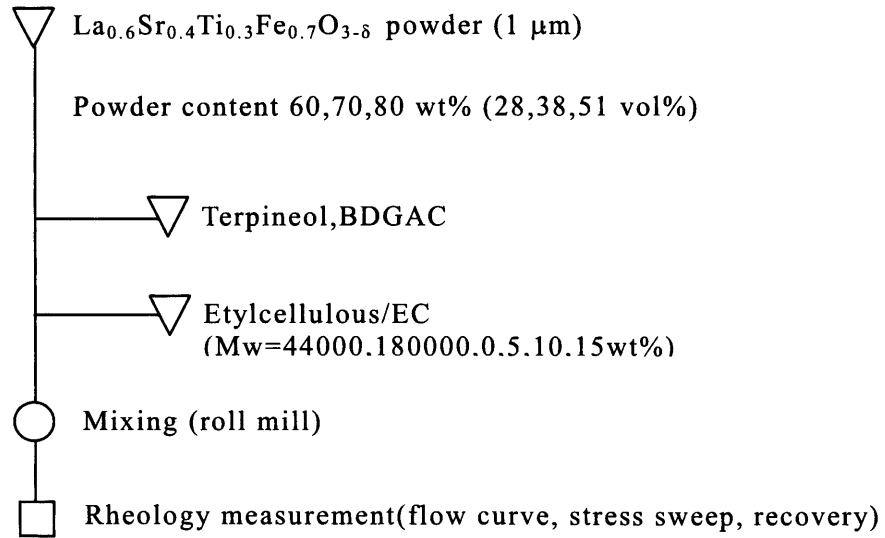


Fig.7-1. Experimental flowchart.

7.2.2. Characterization

The rheological behavior were measured by a rheometer (MARS-2, HAAKE, Germany) using parallel-plate ($\phi = 35\text{mm}$). Through all the tests, the gap between parallel-plate and bottom was 0.1 mm, after the parallel-plate approached 0.1 mm, the excess of the paste was trimmed off. The flow of the paste curve was measured at the shear rate from 0.1 s^{-1} to 100 s^{-1} at $23 \text{ }^\circ\text{C}$. The storage modulus (G') and the loss modulus (G'') were measured at shear stress values from 1 Pa to 5000 Pa at the frequency of 1.0 Hz at $23 \text{ }^\circ\text{C}$. The yield stress of the paste was obtained by the strain curve.

Dynamic viscoelasticity method allows the correlation of the elastic response to the paste's structure. G' , G'' are usually represented as:

$$G^* = G' + iG''$$

where

$$G' = G \times \cos \delta$$

and

$$G'' = G \times \sin \delta$$

where a viscoelastic fluid is characterized by a phase angle $0 < \delta < 90^\circ$. G' is referred as the elastic or storage modulus, which is a measure of the energy stored during the test, while G'' is the viscous or loss modulus, which is used to determine the energy for flow. In an ideal solid $G^* = G'$, whereas for an ideal liquid $G^* = G''$.

For simulate the paste behavior during screen printing process, the recovery characteristics were measured at three intervals. In the first interval, oscillatory measurement was carried out at low share stress of 10 MPa at 1Hz frequency for 60s. In the next interval, rotational measured at high share rate of $100s^{-1}$ for 30s to simulate the paste being moved by the squeegee and pushed through the openings of the screen. In the third interval, the test condition of first interval was applied to the paste again. During the test of first and third interval, the storage modulus (G') and the loss modulus (G'') were measured, then the recovery ratio was calculated from the difference of G' between first and third interval by following formula,

The recovery ratio(%) = G' at third interval / G' at first interval $\times 100$

7.3. Results and Discussion

Figure 7-2 shows the representative result of flow curve at LSTF paste, terpineol and BDGAC solvent system, respectively. All the test samples had a typical rheological behavior of pseudoplastic fluid. The viscosity decreased as the share rate increase. This can be considered to the polymer chain pulled to be straight chain in the area of high share rate. These rheological behaviors were desired for screen printing process.

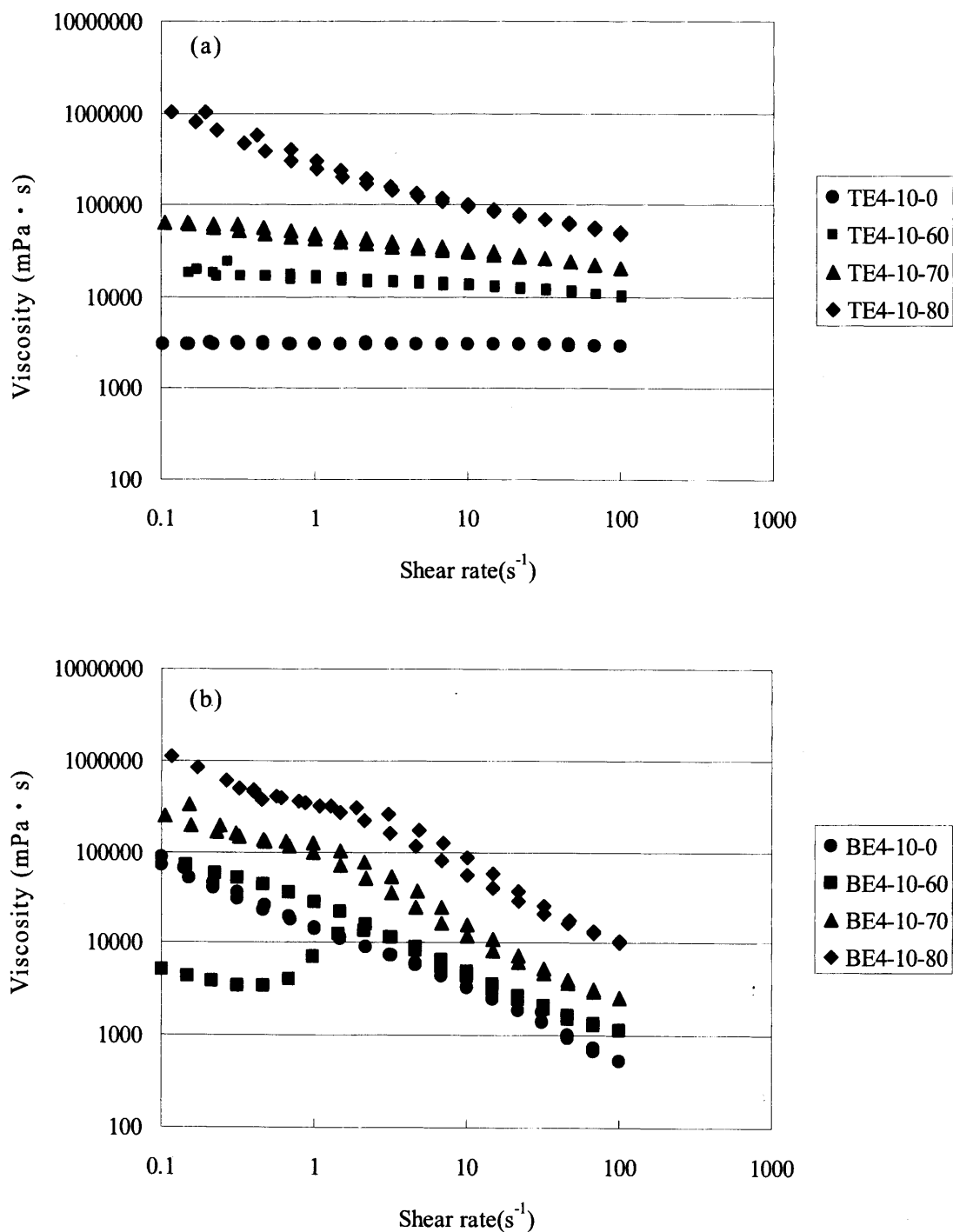


Fig.7-2. Relationship between the viscosity and share rate at LSTF paste.

(a)LSTF+terpineol+EC10wt% (b) LSTF+BDGAC+EC10wt%

Figure 7-3 shows the viscosity of LSTF paste at share rate of 100 s^{-1} using terpeneol at various LSTF particle and EC content. The viscosities were increased with the increase of LSTF particle and EC content in the vehicle system. These similar behaviors were reported at most another paste systems.^{46,47)} The paste of low content with LSTF and EC could flow at low shear stress compared with high content paste. The fundamental data of viscosity for LSTF paste was obtained.

Figure 7-4 shows the viscosity of LSTF paste of 70wt% particle at various EC content in terpeneol and BDGAC. The minimum viscosity was observed near 1 wt% EC content. It suggested that a small addition of EC dispersed the particles of LSTF and the further EC increase the viscosity of the paste, the excess EC may agglomerate LSTF particles in vehicle system. Compared with terpeneol and BDGAC, the viscosity of LSTF paste using terpeneol was larger than that of BDGAC. It was considered the viscosity of BDGAC was lower than terpeneol as shown Figure 7-5, BDGAC could not increase the viscosity of the paste compared with terpeneol.

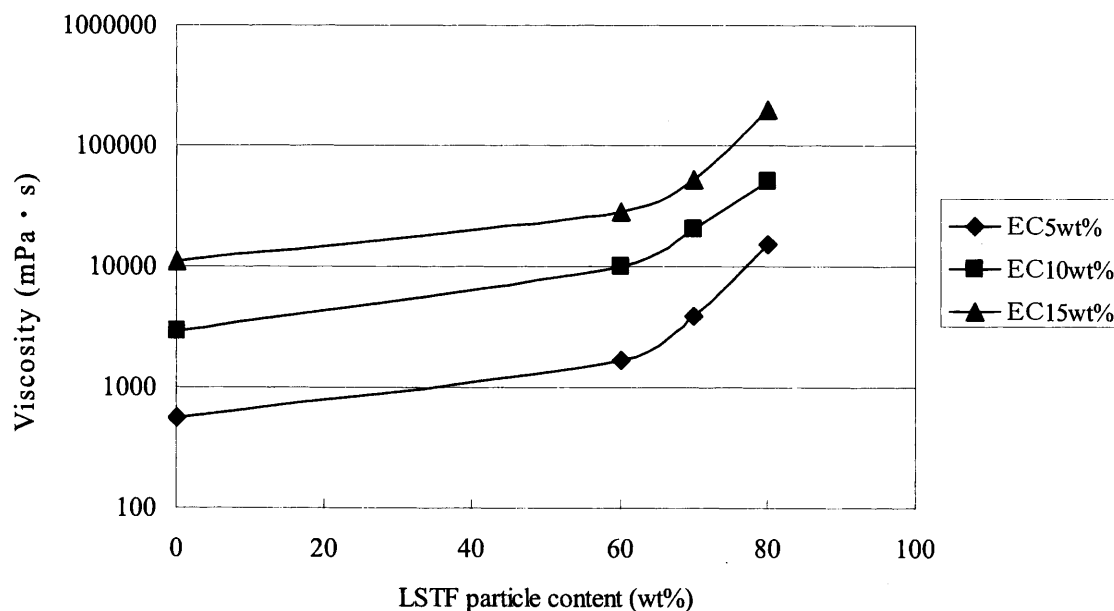


Fig.7-3. The viscosity of LSTF paste at various LSTF particle contents.
(Terpeneol system, share rate = 100 s^{-1})

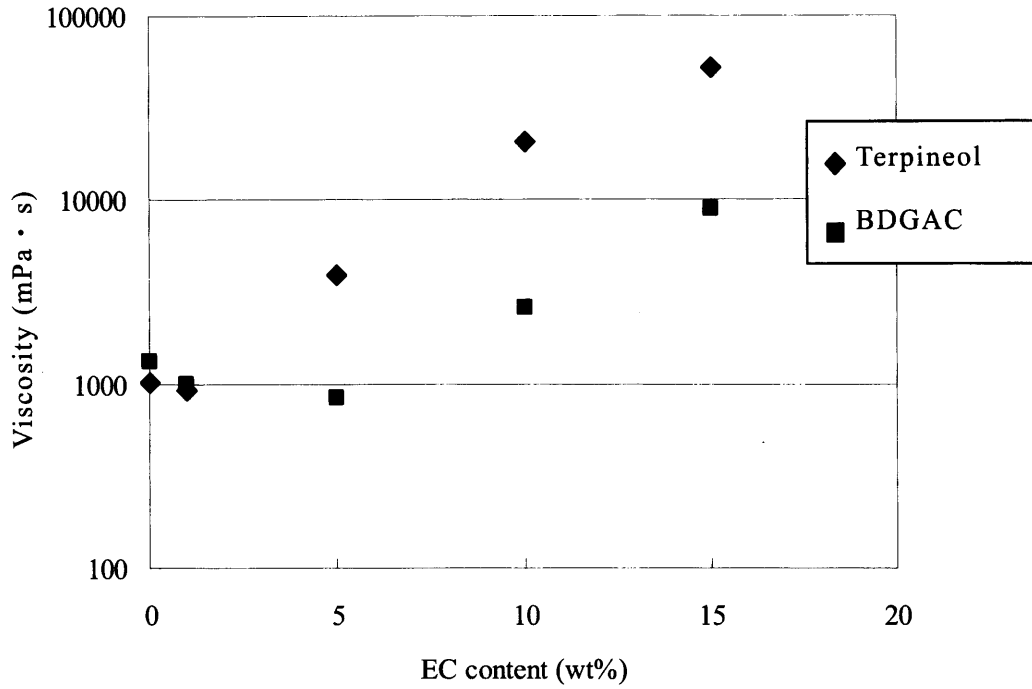


Fig.7-4. The viscosity of LSTF paste at various EC contents.
(LSTF particle content of 70wt%, share rate = 100 s^{-1})

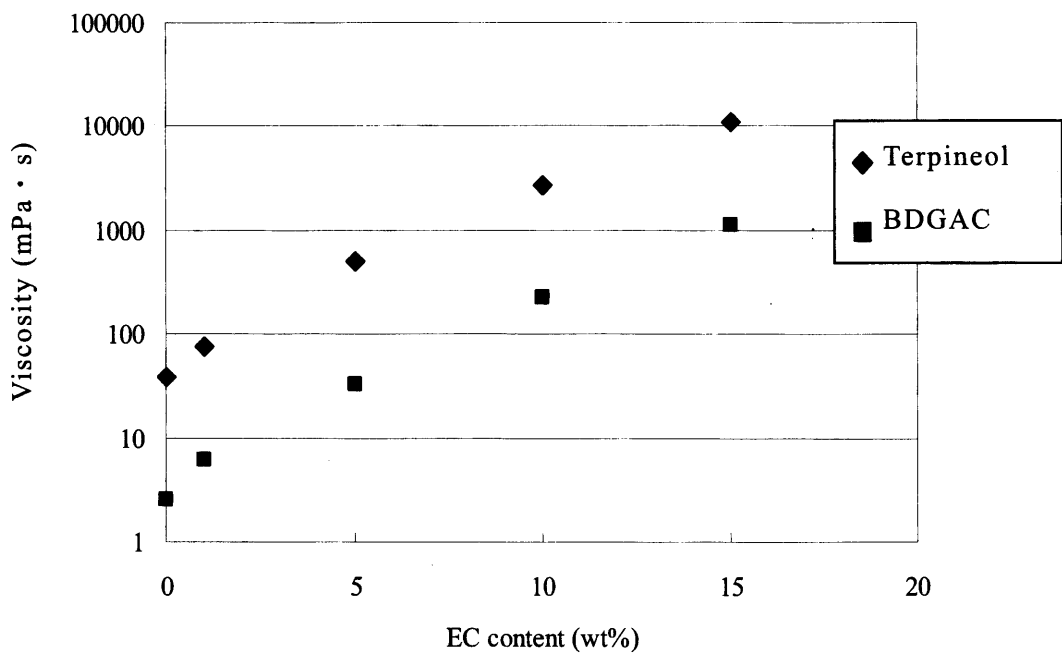


Fig.7-5. The viscosity of vehicle at various EC contents.
(share rate = 100 s^{-1})

Figure 7-6 shows the share stress dependence of G' and G'' (stress sweep curve) for the LSTF paste using the vehicle system of terpineol and EC at various LSTF particle contents. At the paste of LSTF 80wt% particle content, the point of cross over ($G' = G''$) was revealed. In the paste of 60wt% and 70wt% contents, G'' is greater than G' at all stress ranges. As a result, the almost samples were suggested as the liquid behaviors.

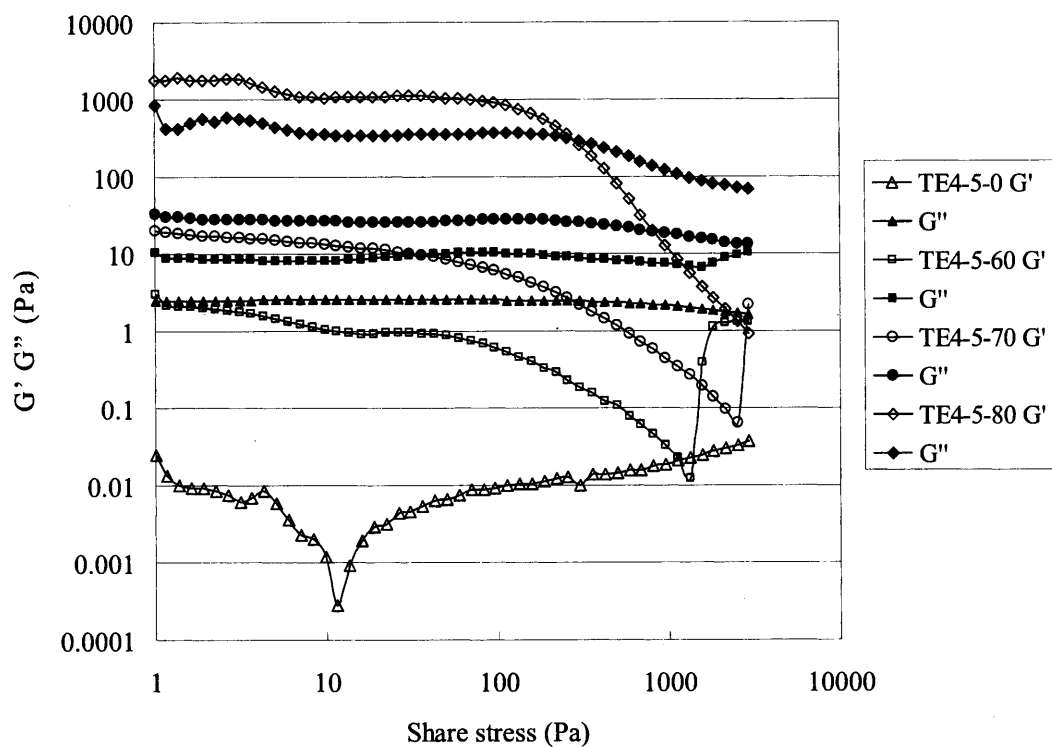


Fig.7-6. Share stress dependence of G' and G'' for the LSTF paste using the vehicle system of 5 wt% EC ($M_w=44000$) in terpineol.

Figure 7-7 shows the stress sweep curve for the LSTF paste using only terpineol not involved EC. The rheological behavior were different from the paste using EC, the 70wt% paste indicated the G' was greater than G'' at low share stress. The LSTF paste using EC could flow at low shear stress compared with the paste not used EC. Therefore the EC supported the dispersion of LSTF particles in solvent.

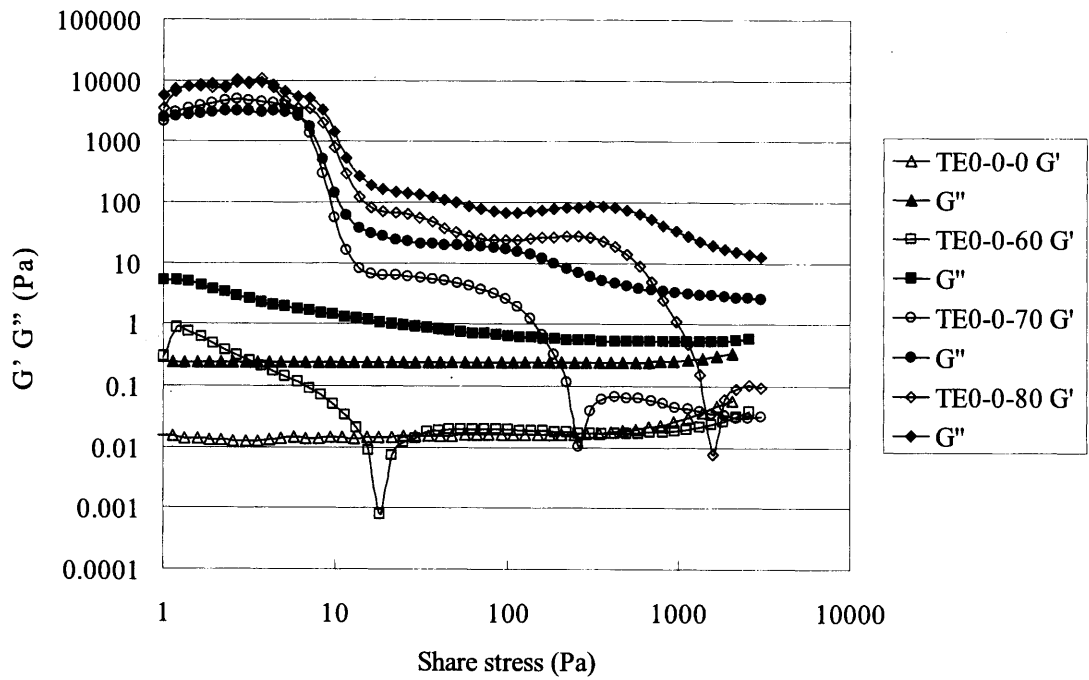


Fig.7-7. Share stress dependence of G' and G'' for the LSTF 70wt% paste using only terpineol not involved EC.

Figure 7-8 shows the share stress dependence of G' and G'' for the LSTF 70wt% paste using the vehicle system of 5-15wt% EC ($M_w=44000$) in terpineol. Optimizing the result, even 5wt% of EC has enough to fluid for the paste of screen printing because of liquid behavior.

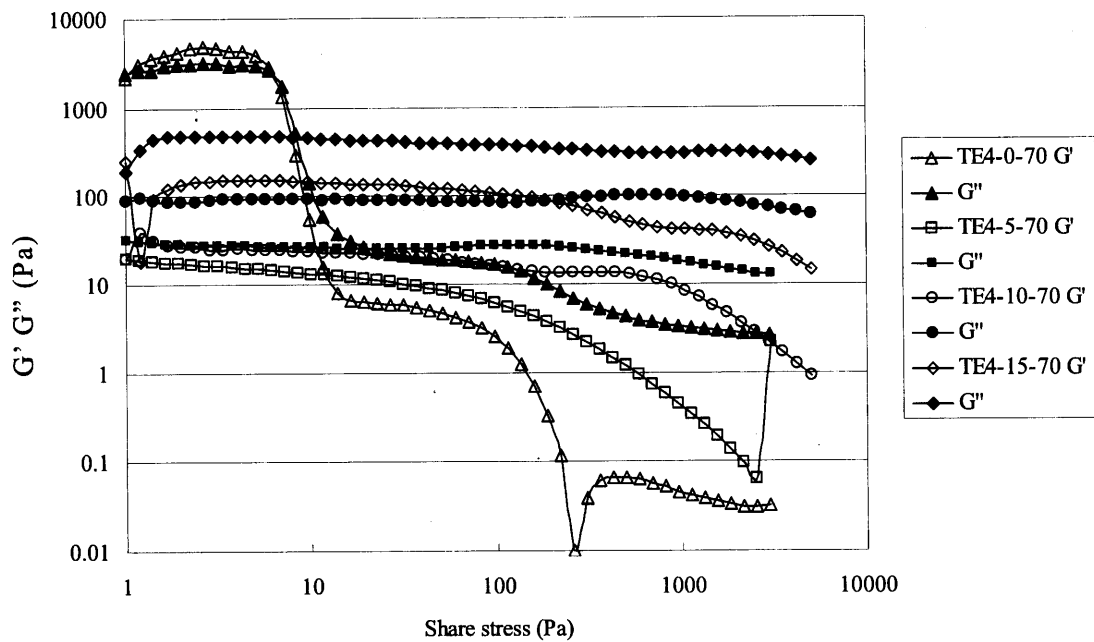


Fig.7-8. Share stress dependence of G' and G'' for the LSTF 70wt% paste using the vehicle system of 5-15 wt% EC ($M_w=44000$) in terpineol.

Figure 7-9 shows the share stress dependence of G' and G'' for the LSTF 70wt% paste using the vehicle system of EC 10wt% ($M_w=44000, 180000$) in terpineol. Using EC of high molecular weight, the rheological behavior changed from liquid to solid. For the purpose of our applications, oxygen permeable membrane, SOFCs, the rheological behavior as liquid are almost desired for screen printing process. Therefore, the EC with low molecular weight was optimized in this study.

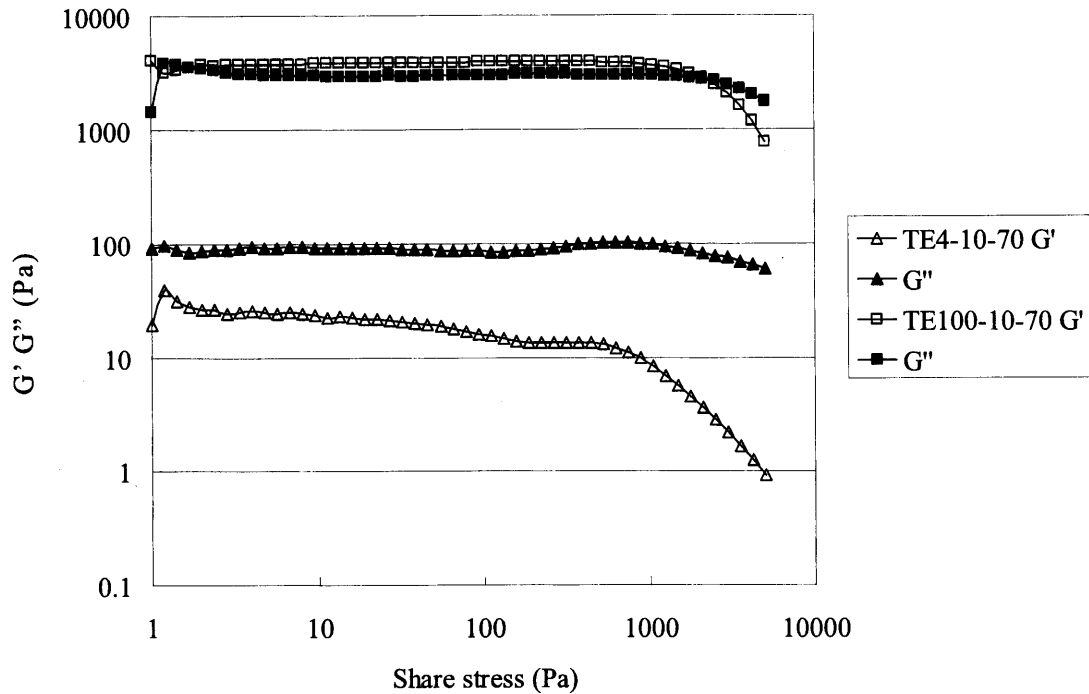


Fig.7-9. Share stress dependence of G' and G'' for the LSTF 70wt% paste using the vehicle system of EC 10 wt% ($M_w=44000, 180000$) in terpineol.

Figure 7-10 shows the yield stress of LSTF paste using terpineol and EC. The values of yield stress were obtained by stress sweep measurement. The yield stress was suddenly increased as the bending point over 70 wt% of LSTF particle content. On increasing the powder content in the paste, the yield stress increased and the interparticle distance between the particles decreased. When the binder flow, the paste can flow and the particles rotate in the paste. In the high powder content pastes, the binder could not occupy a space between the particle-particle. Therefore, on increasing the powder content in the paste, the paste could not flow easily and the high yield stress was needed for flow.

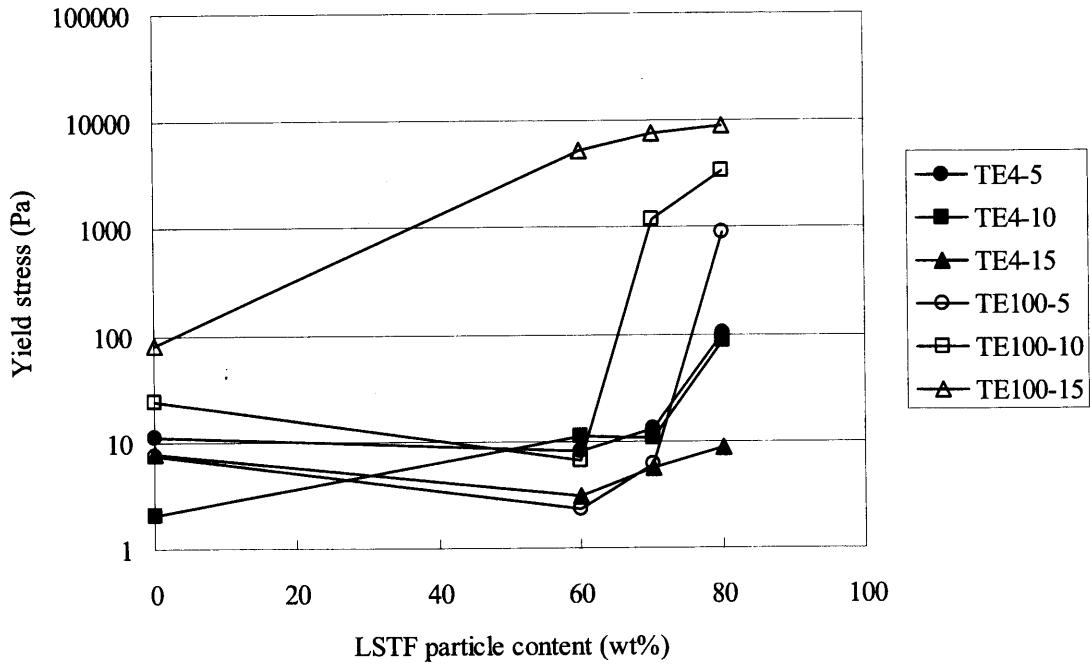


Fig.7-10. The yield stress of LSTF paste using terpineol and EC measured by stress sweep curve.

Figure 7-11 shows the representative results of recovery test. Figure 7-12 shows the recovery ratio using terpineol and BDGAC. It was tendency the recovery ratio was decreased with increase of LSTF particle content except for TE4-10. At TE4-10 paste, the recovery ratio at 70wt% was peculiar high. It was considered the condition of TE4-10-70 paste was well balanced the correlation between LSTF particle and EC. Generally the conducting ceramic paste is desired for high particle content and high recovery characteristics. Therefore, as a result, the LSTF paste was optimized 70wt% LSTF and 10wt%EC in terpineol system.

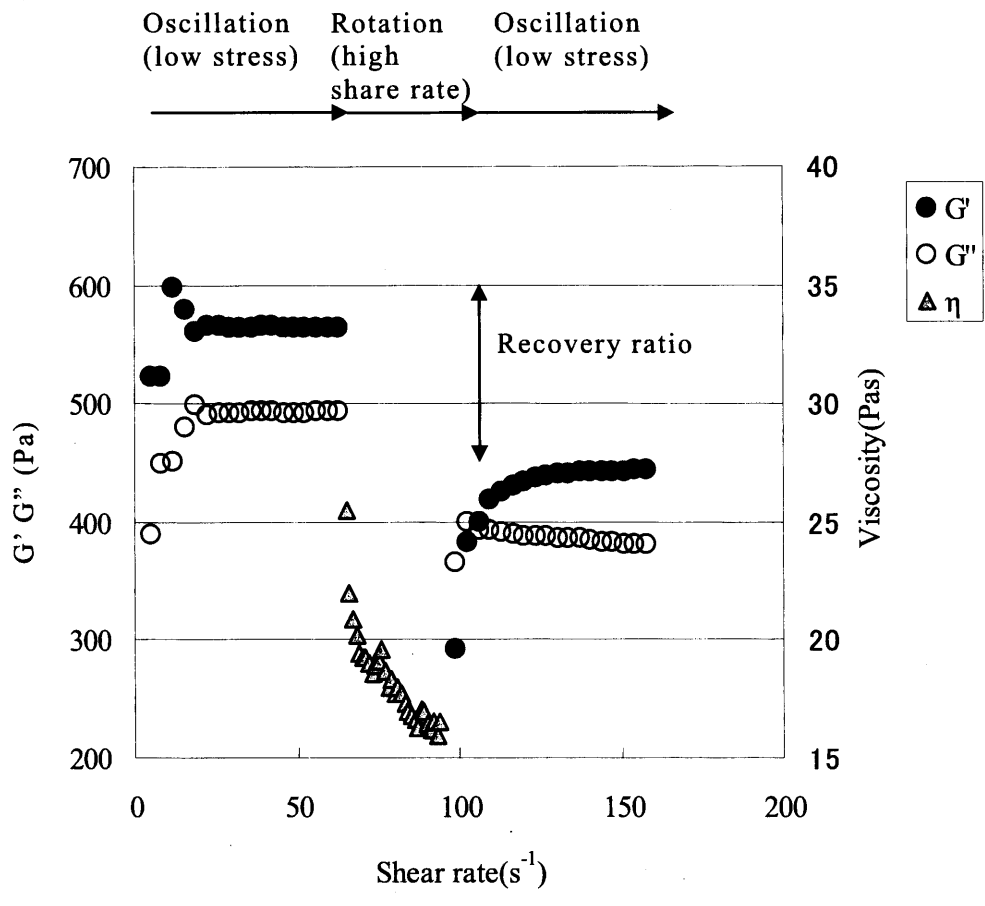


Fig.7-11.Example of the behavior in recovery measurement.
 (paste : TE4-5-80)

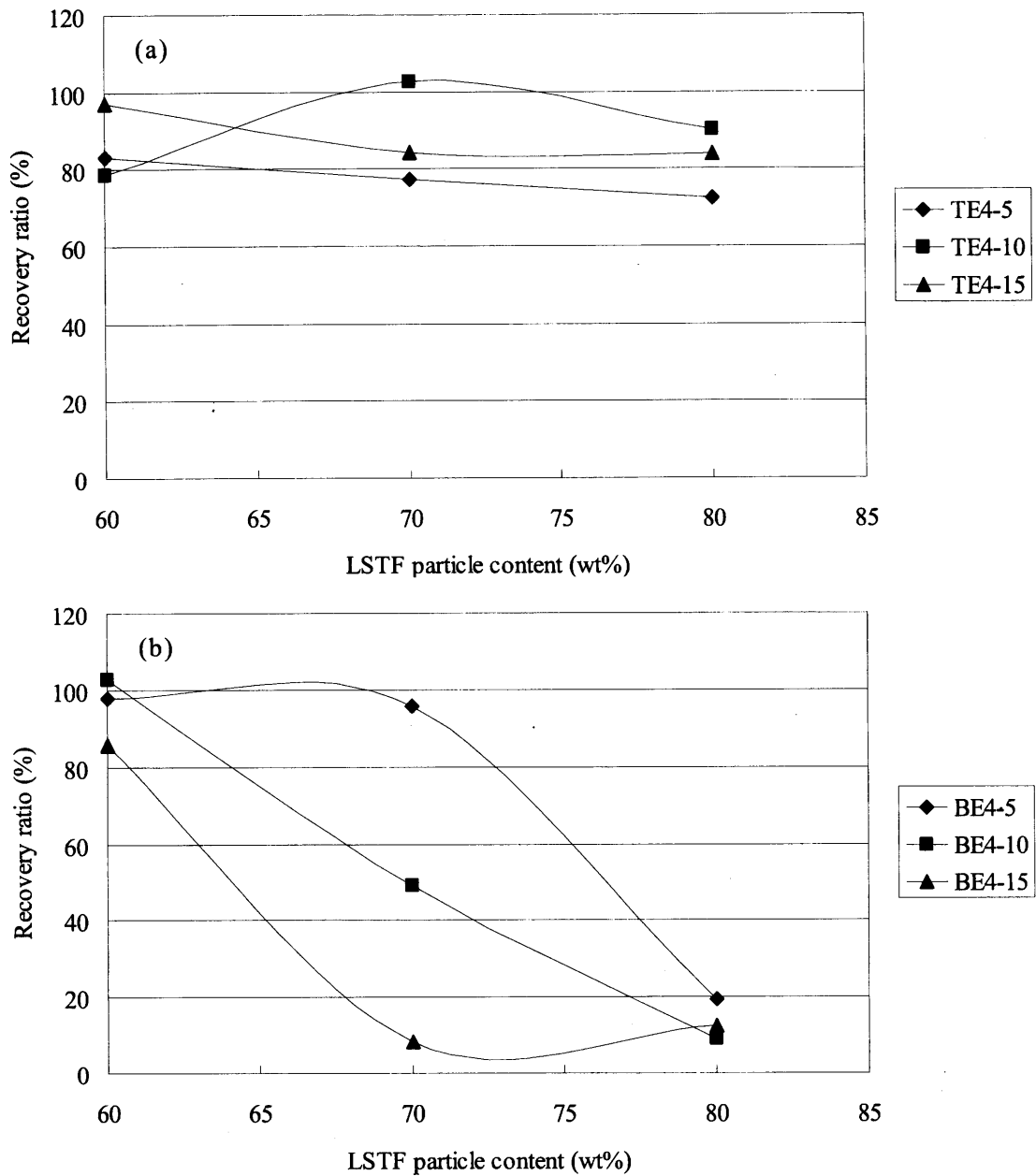


Fig.7-12. The recovery ratio of LSTF paste using (a) terpineol (b) BDGAC.

7.4. Conclusion

Conducting ceramic pastes of $\text{La}_{0.6}\text{Sr}_{0.4}\text{Ti}_{0.3}\text{Fe}_{0.7}\text{O}_{3-\delta}$ (LSTF) were prepared by the vehicle system of EC (ethylcellulos) and organic solvent of terpineol and BDGAC (butyl diglycol acetate). By optimizing the EC content, the powder content in the paste can be increased keeping the paste proper rheological property. The LSTF paste was optimized 70wt% LSTF and 10wt%EC in terpineol system.

8. Summary

In this study, the transport characteristics of $\text{LaSrTiFeO}_{3-\delta}$ oxygen ion conducting materials and the mechanism of thermal expansion in a reducing high-temperature atmosphere were investigated. In addition, the ceramic processes of this material as oxygen ion conducting membranes were optimized for the industrial fabrication and the development in the application. The results in each chapter are summarized as follow:

In chapter 3, the substitution of A-site alkali ions and B-site transition metal ions of the perovskite oxide oxygen-permeating membrane system of $\text{La}_{1-x}\text{Sr}_x\text{Ti}_{1-y}\text{Fe}_y\text{O}_{3-\delta}$, (LSTF) have been studied for their application to the partial oxidation of methane to syngas. Both the substitution of Fe for Ti, and the substitution of Sr for La increased the p-type electronic and oxygen ionic conductivities to 155 and 0.47 Scm^{-1} respectively. From 800 to 1000°C , the temperature dependence of conductivity has been studied, and the thermal activation energy of the p-type electronic conductivity of $\text{La}_{0.6}\text{Sr}_{0.4}\text{Ti}_{0.1}\text{Fe}_{0.9}\text{O}_{3-\delta}$ was found to be 38 kJ/mol and those of the ionic conductivity of $\text{La}_{0.6}\text{Sr}_{0.4}\text{Ti}_{1-y}\text{Fe}_y\text{O}_{3-\delta}$ ($y=0.7$ and 0.9) were 11 and 20 kJ/mol. The thermal expansion coefficients of LSTF were varied from 10.8 to $17.0 (\times 10^{-6}/\text{K}^{-1})$ by increasing the Fe substitution. $\text{La}_{0.6}\text{Sr}_{0.4}\text{Ti}_{0.3}\text{Fe}_{0.7}\text{O}_{3-\delta}$ was the optimized composition with a good trade-off of the high ion conductivity, 0.07 Scm^{-1} , and good matching of the thermal expansion coefficient, $12.4 \times 10^{-6}/\text{K}^{-1}$. It has been tested for the partial oxidation of methane to syngas and shows a high oxygen permeation rate of 13.8 cc/min/cm^2 at 1000°C or 10.5 cc/min/cm^2 at 900°C . In addition, High values of CH_4 conversion and CO selectivity were confirmed at 900°C , 60.0 % and 99.9 % respectively.

In chapter 4, the thermal expansion behavior of $\text{La}_{0.6}\text{Sr}_{0.4}\text{Ti}_{1-x}\text{Fe}_x\text{O}_{3-\delta}$ ($x=0.7$ and 0.9) was investigated by dilatometry and in-situ powder X-ray diffractometry at 25

and 1000°C under controlled oxygen partial pressures in air and at reducing atmosphere, $P_{O_2} = 0.21$ and 1×10^{-20} atm, respectively. The sintered samples of $x=0.7$ and 0.9 showed positive thermal expansions, i.e., 12.4 and $14.4 \times 10^{-6} \text{ K}^{-1}$, respectively, in air up to 1000°C, and also larger expansions at lower partial oxygen pressures, with a linear thermal expansion ratio factor of 0.10 and 0.40% . The change in the crystal lattice parameters analyzed by XRD Rietveld refinement showed that the crystal lattice volume increased with an increase in temperature and a decrease P_{O_2} . The linear thermal expansion rate estimated from volume change of the XRD data for the oxides of $x=0.7$ and 0.9 , were 0.13 and 0.27% , which corresponds to those of estimated from the dilatometry.

In chapter 5, a novel multilayer ceramic deposition process of $\text{La}_{0.6}\text{Sr}_{0.4}\text{Ti}_{0.3}\text{Fe}_{0.7}\text{O}_{3-\delta}$ (LSTF) has been developed for the fabrication of durable oxygen-permeable membranes. By optimizing the diameter of the starting powder and sintering temperature, defects such as peeling and cracking in the ceramic multilayer could be eliminated. With this optimized process, we have fabricated a thin membrane LSTF formed by the slurry coating process on porous support LSTF and found its rate of oxygen permeation to be 18 cc/min/cm^2 .

In chapter 6, $\text{La}_{0.6}\text{Sr}_{0.4}\text{Al}_x\text{Fe}_{1-x}\text{O}_{3-\delta}$ (LSAF) mixed ionic electronic conducting membranes have been sintered, and the substitution of Al for Fe reduced the density of the sintered body including large defect of pore channels. The sintering behavior of the $\text{La}_{0.6}\text{Sr}_{0.4}\text{Al}_{0.1}\text{Fe}_{0.9}\text{O}_{3-\delta}$ samples have been studied under different oxygen partial pressure, P_{O_2} , and a post process of hot isostatic pressing (HIP) has been carried out. The thermal expansion coefficients and the differential expansion ratios measured in air and under reducing atmosphere for these samples were $15.6 \times 10^{-6}/\text{K}^{-1}$ and 0.37% , respectively, and were not affected by the sintering process. The density of the sample sintered in air was 96.5% and the HIP increase the density of the sample up to 99.6% , eliminating the pores. The three point flexural strength of the HIP sample at 25°C and 1000°C were 265MPa and 208MPa , respectively, and the

oxygen permeation rate of the HIP treated membranes with the thickness of 0.5mm was 8cc/min/cm².

In chapter 7, conducting ceramic pastes of La_{0.6}Sr_{0.4}Ti_{0.3}Fe_{0.7}O_{3-δ} (LSTF) were prepared by a vehicle system of EC (ethylcellulose) and organic solvents of terpineol and BDGAC (butyl diglycol acetate). By optimizing the EC content in the LSTF pastes, we have succeeded to increase the LSTF powder content in the paste, keeping the paste high flowability. The LSTF paste was optimized at the composition of 70wt% LSTF and 10wt%EC in the terpineol solvent system.

9. References

- 1) C.A.Udovich, *Stud.Surf.Sci.Catal.*, 119, (1998) 417
- 2) H.Nagahama, *Fuel Cell*, 7 (2007) 112-117
- 3) Chung-Yi Tsai, Anthony G. Dixon, William R. Moser, Yi Huama, *AIChE J.*, 43, 11A, (1997) 2741-2750
- 4) Z.Shao, H.Dong, G.Xiong, Y.Cong, W.Yang, *J.Membrane Science*,183, (2001) 181-192
- 5) T.Ishihara, Y. Tsuruta, T.Todaka, H.Nishiguchi, Y.Takita, *Solid State Ionics*, 152-153, (2002) 709-714
- 6)Y.Suzuki, T.Yamazaki, S.Kaganoi, H.Kurimura, *Separation Process Eng.*,34(1),(2004) 1-8
- 7) Y.Teraoka, H.Zhang, S.Furukawa, N.Yamazoe, *Chemistry Letters*, (1985) 1743-1746
- 8) Y.Teraoka, Y.Honbe, J.Ishii,H.Furukawa,I.Moriguchi, *Solid State Ionics*, 152-153 (2002) 681-687
- 9) J.E.ten Elshof, H.J.M.Bouwmeester, H.Verweij, *Solid State Ionics*, 81, (1995) 97-109
- 10) N.Itoh, T.Kato, K.Uchida, K.Haraya,*J.Mem.Sci.*,92 (1994) 239-246
- 11) S.Hamakawa, F.Mizukami, *Catalysis Society of Japan*, 48 (2006) 308-313
- 12) T.Ishihara, T.Yamada, H.Arikawa, H.Nishiguchi, Y.Takita, *Solid State Ionics*,135 (2000) 631-636
- 13) Y.Tsuruta, T.Todaka, H.Nishiguchi, T.Ishihara, Y.Takita, *Electrochemical and Solid-State Letters* , 4(3) (2001) E13-15
- 14) U.Balachandran, J.T.Dusek, R.L.Mieville, R.B.Poeppel, M.S.Kleefisch, S.Pei, T.P.Kobylinski, C.A.Udovich, A.C.Bose, *Appl.Catal.A*,133 (1995) 19
- 15) H.Takamura, K.Okumura, Y.koshino, A.Kamegawa, M.Okada, *J. Electroceramics*, 13, (2004) 613-618

- 16) S.Pei, M.S.Kllefis, T.P.Kobylinski, J.Faber, C.A.Udovich, V.Z.McCoy, B.Dabrowski, U.Balachandran, R.L.Mieville, R.B.Poeppel., *Catal.Let.*, 30 (1995) 201
- 17) Y.Teraoka, H.M.Zhang, K.Okamoto, N.Yamazoe, *Mat.Res.Bull.*,23(1988)51-58
- 18) T.Ishihara, H.Matsuda, Y.Takita, *J.Am.Chem.Soc.*,116(1994)3801-3803
- 19) Z.Shao, G.Xiong, H.Dong, W.Yang, L.Lin, *Separation and Purification Technology*,25(2001)97
- 20) Y. Teraoka, T. Fukuda, N. Miura and N. Yamazoe, *Journal of the Ceramic Society of Japan*, 97(4) (1989) 476-472
- 21) Y. Teraoka, T. Fukuda, N. Miura and N. Yamazoe, *Journal of the Ceramic Society of Japan*, 97(5) (1989) 533-538
- 22) S. Hamakawa and F. Mizukami, *Catalysis Society of Japan*, 48(5) (2006) 308-313
- 23) L.W.Tai, M.M.Nasrallah, H.U.Anderson, D.M.sparlin and S.R.sehlin, *Solid State Ionics*, 76 (1995) 273-283
- 24) E. A. F. Span, F. J. G. Roesthuis, D. H. A. Blank and H. Rogalla, *Applied Physics A*, 69 (1999) 783-785
- 25) H. Kurimura, M. Harada, *MEMBRANE*, 29(5) (2004) 265-271
- 26) Eric D.Wachsman, Subhash C.Singhal, *American Ceramic Society of Bulletin*, 89(3)(2009)22-32
- 27)H.Yokokawa, N.Sakai, T.Horita, K.Yamaji, M.E.Brito,*MRS Bull*,30(2005)591
- 28) T.Suzuki, Z.Hasan, Y.Funahashi, T.Yamaguchi, Y.Fujishiro, M.Awano, *Science*, 325(2009)852-855
- 29) H.Uchida, T.Osuga, M.Watanabe, *J.Electrochem.Soc.*,146(5)(1999)1677
- 30) N.Oishi, A.Atkinson, N.P.Brandon, J.A.Kilner, B.C.H.Steele, *J.Am.Ceram.Soc.*, 88(2005)1394
- 31) Z. Shao, S. M. Haile, *Nature* 431, (2004) 170-173
- 32) B. C. H. Steele, A. Heinzl, *Nature* 414, (2001) 345-352
- 33) B. Ma, U. Balachandran, J.H. Park, C.U. Segre, *J. Electrochem.Soc.*, 143, 5

- (1996) 1736-1744
- 34) D.P. Fagg, V.V. Kharton, J.R. Frade, A.A.L.Ferreira, *Solid State Ionics* 156 (2003) 45-57
- 35) S. Steinsvik, R. Bugge, J. Gjonnes, J. Tafto, T. Norby, *J. Phys. Chem. Solids* 6 (1997) 969
- 36) V.V. Kharton, A.V. Kovalevsky, A.P. Viskup, J.R. Jurado, F.M. Figueiredo, E.N. Naumovich, J.R. Frade, *J. Solid State Chem.* 156 (2001) 437
- 37) C. Y. Park, A. J. Jacobson, *Solid State Ionics* 176 (2005) 2671
- 38) J. H. Park K. Y. Kim, S. D. Park, *Desalination* 245 (2009) 559
- 39) H. M. Rietveld, *J.Appl. Crystallogr.* 2 (1969) 65
- 40) D.P.Fagg, J.C.Waerenborgh, V.V.Kharton, J.R.Frade, *Solid State Ionics* 146 (2002) 87
- 41) K. Momma and F. Izumi, *J. Appl. Crystallogr.* 41 (2008) 653
- 42) J. Mizusaki, N. Mori, H. Takai, Y. Yonemura, H. Minamiue, H. Tagawa, M. Dokiya, H. Inaba, K. Naraya, T. Sasamoto, T. Hashimoto, *Solid State Ionics* 129 (2000) 163
- 43) Y. Takahashi, A. Kawahara, T. Suzuki, M. Hirano, W. Shin, *Solid State Ionics* 181 (2010) 300-305
- 44) JP-Patent Publication NO.2007-51035
- 45) X.Chan,C.Zhang,X.Dong,W.Zhou,W.Jin,Z.Shao,N.Xu,*J.Mem.Sci*, 316, (2008) 128-136
- 46) W.Tseng, C. Chen, *Materials Science and Engineering*, A347(2003)145-153
- 47) X.Lu, Y.Lee, S.Yang,Y.Hao,J. R.G Evans, C.G.Parini, *J.Eur.Ceram.Soc.*, 30(2010)1-10

10. List of Publications

1) “Perovskite membrane of $\text{La}_{1-x}\text{Sr}_x\text{Ti}_{1-y}\text{Fe}_y\text{O}_{3-\delta}$ for partial oxidation of methane to syngas” *Solid State Ionics*, 181 (2010) 300–305.

Y.Takahashi, A.Kawahara, T.Suzuki, M.Hirano, W.Shin . . . Chapter 3

2) “Dilatometry and high-temperature X-ray diffractometry study of $\text{La}_{0.6}\text{Sr}_{0.4}\text{Ti}_{0.1}\text{Fe}_{0.9}\text{O}_{3-\delta}$ and $\text{La}_{0.6}\text{Sr}_{0.4}\text{Ti}_{0.3}\text{Fe}_{0.7}\text{O}_{3-\delta}$ oxygen-permeable membranes” *Solid State Ionics*, 181 (2010) 1516–1520.

Y.Takahashi, T.Suzuki, A.Kawahara, Y. Ando, M.Hirano, W.Shin . . . Chapter 4

3) “Multilayer ceramic deposition process of dense oxygen permeation membranes on porous supports” *Desalination and Water Treatment*, 17 (2010) 57–65.

Y.Takahashi, Y.Ando, A.Kawahara, M. Hirano, W.Shin . . . Chapter 5

4) “ $\text{LaSrAlFeO}_{3-\delta}$ oxygen ion conducting membranes sintered under different atmosphere and HIP” *Journal of the Ceramic Society of Japan*, 118(12) (2010) 1144-1149.

Y.Takahashi, W.Shin . . . Chapter 6

11. Acknowledgment

This study is gratefully supported by Professor W. Shin (AIST and Nagoya Institute of Technology), who is the supervisor of this study. I also thank Professor T. Kasuga (Nagoya Institute of Technology), Professor Y. Iwamoto (Nagoya Institute of Technology) and Professor K. Kakimoto (Nagoya Institute of Technology) for their insightful comments and constructive suggestions on this study.

The support of Noritake Co., Limited's coworkers (Mr. Y.Ando, Dr. Balagopal.N.Nair, Mr. Y.Hirano, Mr. S.Suzuki, Dr. A.Kawahara et.al) and CHUBU Electric Power Co.'s researchers (Dr. M.Hirano, Dr. T.Kasuga et.al) and AIST's researchers (Dr. I. Matsubara, Dr T. Ito, Dr. S. Murakami, Ms. K. Ri et.al) are highly acknowledged.

I also thank my family and my wife for their warm encouragement.